The lifecycle of molecular clouds in nearby star-forming disc galaxies

Mélanie Chevance,[1][*] J. M. Diederik Kruijssen,[1] Alexander P. S. Hygate,[2,1]
Andreas Schruba,[3] Steven N. Longmore,[4] Brent Groves,[5] Jonathan D. Henshaw,[2]
Cinthya N. Herrera,[6] Annie Hughes,[7,8] Sarah M. R. Jeffreson,[1] Philipp Lang,[2]
Adam K. Leroy,[9] Sharon E. Meidt,[10] Jérôme Pety,[6,11] Alessandro Razza,[12]
Erik Rosolowsky,[13] Eva Schinnerer,[2] Frank Bigiel,[14] Guillermo A. Blanc,[12,15]
Eric Emsellem,[16,17] Christopher M. Faesi,[2] Simon C. O. Glover,[18] Daniel T. Haydon,[1]
I-Ting Ho,[2] Kathryn Kreckel,[2,1] Janice C. Lee,[19] Daizhong Liu,[2] Miguel Querejeta,[16,20]
Toshiki Saito,[2] Jiayi Sun,[9] Antonio Usero[20] and Dyas Utomo[9]

Affiliations are listed at the end of the paper

ABSTRACT

It remains a major challenge to derive a theory of cloud-scale ($\lesssim 100$ pc) star formation and feedback, describing how galaxies convert gas into stars as a function of the galactic environment. Progress has been hampered by a lack of robust empirical constraints on the giant molecular cloud (GMC) lifecycle. We address this problem by systematically applying a new statistical method for measuring the evolutionary timeline of the GMC lifecycle, star formation, and feedback to a sample of nine nearby disc galaxies, observed as part of the PHANGS-ALMA survey. We measure the spatially-resolved (~ 100 pc) CO-to-Hα flux ratio and find a universal de-correlation between molecular gas and young stars on GMC scales, allowing us to quantify the underlying evolutionary timeline. GMC lifetimes are short, typically $10-30$ Myr, and exhibit environmental variation, between and within galaxies. At kpc-scale molecular gas surface densities $\Sigma_{H_2} \geqslant 8$ M$_\odot$ pc^{-2}, the GMC lifetime correlates with time-scales for galactic dynamical processes, whereas at $\Sigma_{H_2} \leqslant 8$ M$_\odot$ pc^{-2} GMCs decouple from galactic dynamics and live for an internal dynamical time-scale. After a long inert phase without massive star formation traced by Hα ($75-90$ per cent of the cloud lifetime), GMCs disperse within just $1-5$ Myr once massive stars emerge. The dispersal is most likely due to early stellar feedback, causing GMCs to achieve integrated star formation efficiencies of $4-10$ per cent. These results show that galactic star formation is governed by cloud-scale, environmentally-dependent, dynamical processes driving rapid evolutionary cycling. GMCs and H II regions are the fundamental units undergoing these lifecycles, with mean separations of $100-300$ pc in star-forming discs. Future work should characterise the multi-scale physics and mass flows driving these lifecycles.

Key words: stars: formation – ISM: clouds – ISM: structure – galaxies: evolution – galaxies: ISM – galaxies: star formation

1 INTRODUCTION

The lifecycle of giant molecular clouds (GMCs) resides at the heart of the physics driving star formation and stellar feedback in galaxies. Star formation takes place in GMCs (e.g. Kennicutt & Evans 2012) and the stellar feedback from the newly-formed stars de-

posits mass, metals, energy and momentum into the GMCs, eventually leading to their disruption (e.g. Dobbs et al. 2014; Krumholz 2014) and regulating the galaxy-wide star formation rate (SFR; e.g. Ostriker & Shetty 2011; Hayward & Hopkins 2017; Krumholz et al. 2018). These cloud-scale ($\lesssim 100$ pc) processes determine how galaxies evolve and form stars (e.g. Scannapieco et al. 2012; Hopkins et al. 2013; Semenov et al. 2018; Kruijssen et al. 2019), imply-

---

[*] E-mail: chevance@uni-heidelberg.de

ing that an understanding of galaxy evolution requires describing a rich variety of physics over a wide range of spatial scales.

Recent simulations of galaxy formation and evolution are now able to resolve the scales of GMCs (e.g. Grand et al. 2017; Hopkins et al. 2018), but observations have long been unable to match this step outside a small number of very nearby galaxies, mostly confined to the Local Group (e.g. Bolatto et al. 2008; Kawamura et al. 2009; Miura et al. 2012; Hughes et al. 2013; Corbelli et al. 2017; Faesi et al. 2018; Kruijssen et al. 2019; Schruba et al. 2019). It is critical to obtain an empirical census of the GMC lifecycle across a wider range of galactic environments, spanning the main sequence of galaxies at $z = 0$ (e.g. Brinchmann et al. 2004). Covering a wide range of environments is important, because the cosmic star formation history peaked at redshift $z \sim 2-3$ (Madau & Dickinson 2014) and it is currently unclear if the GMC lifecycle proceeded differently under the high-pressure and high-gas fraction conditions prevalent in high-redshift galaxies (e.g. Genzel et al. 2011; Swinbank et al. 2011, 2012; Tacconi et al. 2013, 2018), with claimed lifetimes of up to several 100 Myr (Zanella et al. 2019). Analytical and numerical studies predict that the GMC lifecycle likely varies with the galactic environment (e.g. Dobbs & Pringle 2013; Dobbs et al. 2015; Fujimoto et al. 2014; Jeffreson & Kruijssen 2018; Meidt et al. 2018, 2019). Due to a crucial lack of observational constraints on GMC scales across a variety of environments, it is therefore not known how most stars in the Universe formed and how they affect galaxy evolution through feedback. Thanks to the construction of large sub-mm interferometers such as the Atacama Large Millimeter/submillimeter Array (ALMA) and the Northern Extended Millimeter Array (NOEMA), it is now possible to overcome this problem.

Observationally, galaxies globally follow a 'star formation relation', linking the gas surface density and the SFR surface density (e.g. Silk 1997; Kennicutt 1998). This has been observed in a large range of galaxies, from nearby spiral galaxies (e.g. Bigiel et al. 2008; Blanc et al. 2009; Schruba et al. 2011; Kennicutt & Evans 2012; Leroy et al. 2013) to high redshift galaxies (e.g. Daddi et al. 2010; Genzel et al. 2010; Tacconi et al. 2013). These empirical, large-scale relations are often used in galaxy formation simulations to describe the relation between gas mass and SFR. However, these relations do not apply universally; they are observed to break down at scales $\lesssim 1$ kpc (e.g. Onodera et al. 2010; Schruba et al. 2010; Leroy et al. 2013; Kreckel et al. 2018; Kruijssen et al. 2019) as well as in low-density environments, such as in low surface brightness galaxies or in galaxy outskirts (e.g. Kennicutt 1989; Martin & Kennicutt 2001; Boissier et al. 2003; Bigiel et al. 2010; Goddard et al. 2010).

As demonstrated by Kruijssen & Longmore (2014), the small-scale breakdown of the star formation relation is driven by evolutionary processes taking place at the scale of molecular clouds. The details of how the star formation relation breaks down differ between different galaxies (Leroy et al. 2013), which suggests that the evolution of individual clouds depends on the galactic environment. Such an environmental dependence has been predicted by theory. Galaxy dynamics, interstellar medium (ISM) pressure, and disc structure modify the balance of cloud formation and destruction (e.g. Dobbs & Pringle 2013; Dobbs et al. 2014; Fujimoto et al. 2014; Jeffreson & Kruijssen 2018; Krumholz et al. 2018; Meidt et al. 2018, 2019) and therefore influence the population and lifecycle of GMCs. One of the major challenges in understanding the parsec-scale physics of star formation and feedback within GMCs and their impact on galaxy evolution is to resolve the scales of individual clouds within galaxies and empirically constrain their life-

cycles as a function of the galactic environment (e.g. Lada et al. 2010; Hopkins et al. 2013). This requires a large (> 100) sample of GMCs and star-forming regions for a wide variety ($\gtrsim 10$) of galaxies covering different ISM conditions (e.g. densities, pressures) and kinematics (e.g. dynamical time-scales) to obtain sufficiently representative statistics. In this paper, we address this problem by characterising the GMC lifecycle across nine star-forming disc galaxies spanning a range of properties.

There are two main competing theories describing the cloud lifecycle, which predict strong differences in the time evolution of individual clouds. In one theory, clouds are described as long-lived, stable objects, supported by magnetic fields, such that star formation proceeds over long time-scales (~ 100 Myr; e.g. McKee 1989; Vázquez-Semadeni et al. 2011). In a second theory, clouds are transient objects, undergoing gravitational free-fall or dynamical dispersal, in which star formation proceeds on a dynamical time-scale (~ 10 Myr; e.g. Elmegreen 2000; Hartmann et al. 2001; Dobbs et al. 2011). Measuring the molecular cloud lifetime is a key step to distinguish between these two theories, but so far observations have only been made for small samples and have yielded a variety of different outcomes, largely due to differences in experiment design and the use of differing, subjective ways of defining objects (i.e. GMCs and HII regions).

GMC lifetimes are well in excess of a human lifetime, requiring the use of indirect methods to constrain their lifecycles. Long cloud lifetimes (~ 100 Myr) have been suggested by the presence of molecular clouds in between spiral arms (i.e. 'inter-arm' GMCs, see e.g. Scoville & Hersh 1979; Scoville & Wilson 2004; Koda et al. 2009). Short cloud lifetimes ($10-50$ Myr) have been measured by classifying the clouds based on their star formation activity (Engargiola et al. 2003; Blitz et al. 2007; Kawamura et al. 2009; Murray 2011; Miura et al. 2012; Corbelli et al. 2017), or by quantifying the fraction of CO-bright versus Hα-bright lines of sight across each galaxy (Schinnerer et al. 2019). Finally, evolution along orbital streamlines has been used to infer cloud lifetimes, leading to values ranging from ~ 1 Myr in the Central Molecular Zone of the Milky Way (Kruijssen et al. 2015; Henshaw et al. 2016; Barnes et al. 2017; Jeffreson et al. 2018) to $20-50$ Myr in the central ~ 4 kpc of M51 (Meidt et al. 2015). While the classification of clouds based on their star formation activity is the most promising method due to its general applicability, the subjective definition of cloud categories and the fact that the cloud structure needs to be resolved to classify them limits the application of this method to very nearby galaxies, mostly confined to the Local Group. This can potentially be overcome by describing star formation in galaxies as a multi-scale process, such that the cloud lifecycle is inferred without needing to resolve individual GMCs (Kruijssen et al. 2018, see below).

In addition to the overall cloud lifetime, the co-existence (or overlap) time-scale of GMCs and HII regions provides an essential diagnostic for probing the cloud-scale physics of star formation and feedback. By measuring how long GMCs survive after the appearance of ionising photons generating Hα emission, it is possible to identify the feedback mechanism driving GMC dispersal. In principle, GMC dispersal could be driven by a number of processes, including supernovae, stellar winds, photoionisation, and radiation pressure (e.g. Krumholz 2014; Dale 2015; Krumholz et al. 2019). Crucially, many of these processes act on different time-scales and all of these have different environmental dependences, so that it is possible to determine their relative importance by measuring the characteristic time-scale for gas dispersal as a function of the galactic environment. Other feedback mechanisms, such as protostellar

outflows are local mechanisms which are incapable of disrupting entire GMCs (Bally 2016; Krumholz et al. 2019).

Capitalising on the unprecedented resolution and sensitivity achieved by ALMA, the method introduced by Kruijssen et al. (2018) develops a statistical approach for empirically characterising the evolutionary timeline of cloud evolution, star formation, and feedback by describing the multi-scale nature of the star formation relation in galaxies. This method is based on the fact that the breakdown of the star formation relation between the gas mass and the SFR on sub-kpc scales is highly sensitive to the time-scales governing the GMC lifecycle. In brief, it uses cloud-scale variations of the flux ratio between tracers of molecular gas and star formation to determine the relative occurrence of both phases, thus constraining their relative durations. This approach is agnostic about observational criteria often used to define GMCs or HII regions, and instead defines these empirically as emission peaks that are positioned on the timeline describing their evolutionary lifecycles in a way that is independent from their neighbours. We refer to these as 'independent regions' and find that the identified objects resemble classical GMCs and HII regions in terms of their spatial dimensions. Rather than needing to resolve individual GMCs, as was the case in previous methods, this new technique only requires resolving the mean separation length of the combined population of GMCs and HII regions (a few 100 pc). This enables the systematic application of this method across a significant part of the local galaxy population (out to ~ 50 Mpc with ALMA's currrent capabilities).

As a result, we can now determine the molecular cloud lifetime, the time-scale for cloud dispersal by feedback, as well as the characteristic distance between individual sites of star formation. In turn, these constrain a variety of additional physical quantities, such as the integrated cloud-scale star formation efficiency, the mass loading factor (i.e. the feedback-driven mass outflow rate in units of the SFR), and the feedback outflow velocity. The accuracy of the method has been demonstrated using simulated galaxies (Kruijssen et al. 2018) and it has been applied to the individual galaxies NGC300 (Kruijssen et al. 2019), the Large Magellanic Cloud (Ward et al. 2019) and M33 (Hygate et al. 2019a). Kruijssen et al. (2019) find a de-correlation between gas and star formation in NGC300, which they attribute to the rapid evolutionary cycling between molecular gas, star formation, and cloud destruction by stellar feedback. Fujimoto et al. (2019) build on this empirical result to propose that this de-correlation is a fundamental test of feedback physics in galaxy simulations, as it probes the dispersive effect of stellar feedback on GMCs.

Here, we greatly expand the sample of galaxies analysed, to cover a relevant range of galaxy types and environments in which star formation takes place and obtain representative constraints on the molecular cloud lifecycle. The systematic application of these novel analysis techniques requires a high-resolution, multi-wavelength census of the nearby galaxy population. To date, the main challenge has been to obtain homogeneous sensitivity mapping of the molecular gas across a large number of galaxies at ~ 100 pc resolution. With the PHANGS[1] collaboration, we have now made this step by carrying out the PHANGS-ALMA survey (A. K. Leroy et al. in prep.), which is mapping the CO emission across the star-forming discs of ~ 80 nearby galaxies at a point-source sensitivity high enough to detect molecular clouds down to $\sim 10^5$ M$_\odot$. In combination with matched-resolution, ground-based

---

[1] Physics at High Angular Resolution in Nearby GalaxieS; http://phangs.org.

Hα maps, these observations probe the multi-phase structure of galaxies at 1″ resolution (35−162 pc for our sample), which allows us to characterise the lifecycle of cloud evolution, star formation, and feedback as a function of galactic environment.

In this paper, we present the first systematic characterisation of the molecular cloud lifecycle in a first sample of nine nearby star-forming galaxies. The structure of the paper is as follows. In Section 2, we first present the observational data, describing the distribution of gas and SFR tracers in nine nearby galaxies. In Section 3, we summarise the statistical method used to derive the characteristic quantities of star formation and feedback. In Section 4, we then present the derived quantities characterising star formation and feedback processes for the nine galaxies, and carry out a detailed comparison of the measured molecular cloud lifetimes with analytical predictions in Section 5. Finally, we discuss the physical interpretation and implications of the results in Section 6, and conclude in Section 7.

2 OBSERVATIONS

We now summarise our galaxy sample, describe the observational data used to trace molecular gas and recent star formation, and discuss the procedure used to obtain total SFRs.

2.1 Sample selection

We use a sample of nine galaxies with currently available, high-resolution, multi-wavelength coverage, targeted by the PHANGS-ALMA survey (P.I. E. Schinnerer; A. K. Leroy et al. in prep.). One of the main science goals of the PHANGS collaboration is to link the cloud-scale physics governing ISM structure, star formation, and feedback with galaxy evolution. One of the key steps for achieving this is to map the molecular gas distribution in nearby star-forming galaxies at high physical resolution and high sensitivity. An initial sample of 17 galaxies has been observed during ALMA Cycle 3, targeting the $J = 2 - 1$ transition of carbon monoxide (CO) at a resolution of $\sim 1''$, which is expanded to a total of 74 galaxies in ALMA Cycle 5. The observations are described in more detail in (A. K. Leroy et al. in prep.; also see Sun et al. 2018 and Utomo et al. 2018), but we summarise them below. The galaxies have been selected to be nearby ($\lesssim 17$ Mpc), relatively face-on (inclination $\lesssim 75°$) and to lie on or near the main sequence of star formation [$\log_{10}(\text{SFR}/M_\star)$ [yr^{-1}] $\gtrsim -11$ and $\log_{10}(M_\star)$ [$M_\odot$] $\gtrsim 9.3$]. At these distances, the spatial resolution achieved across our sample of nine galaxies ranges from 35−162 pc. This spatial scale is close to the typical sizes of GMCs measured in the Milky Way (Solomon et al. 1987; Heyer et al. 2009; Miville-Deschênes et al. 2017), implying that the galaxy sample is suitable for constraining the GMC lifecycle using our methodology (see Sections 3 and 6).

From this initial sample of the PHANGS-ALMA CO survey, we select the objects which also have newly obtained narrow-band Hα observations with the MPG/ESO 2.2-m Wide-Field Imager (WFI; A. Razza et al. in prep.) or archival high-quality Hα observations available at a similar resolution. This restricts our final sample to eight nearby star-forming galaxies: NGC628, NGC3351, NGC3627, NGC4254, NGC4303, NGC4321, NGC4535 and NGC5068. In addition to these targets, we also include the galaxy NGC5194 for which archival observational data of Hα and CO(1-0) are also available at a similar spatial resolution (Pety et al. 2013; Schinnerer et al. 2013). The main characteristics

Table 1. Physical and observational properties of the targets.

Galaxy	Stellar mass[a] [$\log_{10}$ M$_\odot$]	Metallicity[b] [12+log(O/H)]	CO[c] resolution [″]	CO[c,d] sensitivity [K km s^{-1}]	Hα observations	Hα resolution [″]	Spatial resolution[e] [pc]
NGC628 (*M74*)	10.24	8.65	1.12	1.3	WFI	0.87	53
NGC3351 (*M95*)	10.28	8.80	1.46	1.2	KPNO[f]	1.16	84
NGC3627 (*M66*)	10.67	8.33	1.57	1.6	WFI	1.44	109
NGC4254 (*M99*)	10.52	8.62	1.71	0.7	WFI	1.21	154
NGC4303 (*M61*)	10.67	8.69	1.84	1.1	WFI	0.81	162
NGC4321 (*M100*)	10.71	8.69	1.64	1.0	KPNO[f]	1.28	137
NGC4535	10.49	8.68	1.56	0.8	WFI	1.20	139
NGC5068	9.36	8.39	1.00	1.8	WFI	1.15	35
NGC5194 (*M51*)	10.73	8.84	1.06	4.9	KPNO[f]	1.83	79

[a] Stellar masses are presented in Leroy et al. (2019) and references therein, with typical uncertainties of 0.1 dex.

[b] Mean molecular gas mass-weighted metallicity based on Pilyugin et al. (2014), with typical uncertainties of 0.03 dex.

[c] CO(1-0) for NGC5194 from Schinnerer et al. (2013); CO(2-1) for all other galaxies.

[d] Characteristic 1σ sensitivity corresponding to the root-mean-squared noise across the integrated intensity CO map at the resolution given in the preceding column.

[e] Deprojected spatial resolution accounting for inclination, calculated as the maximum of the CO and Hα maps. The adopted distances and inclinations are listed in Table 3.

[f] *Spitzer* Infrared Nearby Galaxy Survey (SINGS) (Kennicutt et al. 2003).

of these galaxies and of the observations are summarised in Table 1. We now summarise the properties of the CO and Hα data used.

2.2 Molecular gas tracer

As discussed previously, we measure molecular cloud lifetimes in a sample of nine star-forming disc galaxies. To ensure the homogeneity of the results, we select the same tracers of molecular gas and recent star formation across the entire galaxy sample (with the exception of NGC5194; see below). The CO (*J*=1-0) transition [denoted as CO(1-0) in the following] and the CO (*J*=2-1) transition [denoted as CO(2-1) in the following] are commonly used to trace molecular gas (e.g. Schuster et al. 2007; Leroy et al. 2009; Bolatto et al. 2013; Sandstrom et al. 2013). The effective critical density for exciting CO(2-1) is higher than for CO(1-0) ($\sim 10^3$ cm^{-3} and $\sim 10^2$ cm^{-3}, respectively; Leroy et al. 2017a), implying that this tracer is less affected by optical depth. In addition, the mapping of CO(2-1) at a given resolution with ALMA is more efficient than for CO(1-0), which makes it a commonly observed transition for extragalactic studies of molecular gas and the tracer of choice in the PHANGS-ALMA survey (A. K. Leroy et al. in prep.). While CO(2-1) does not trace specifically the high density molecular gas (traced for example by HCN, HCO$^+$), it is brighter and easier to observe than these high density gas tracers, allowing entire galaxies to be mapped efficiently at arcsecond resolution. We therefore use the CO(2-1) transition as a tracer of the molecular gas for all galaxies except NGC5194, for which only a CO(1-0) map is available at high resolution, observed by the Plateau de Bure Interferometer (PdBI; Pety et al. 2013; Schinnerer et al. 2013).

The typical angular resolution is $1-2''$, allowing us to achieve a median physical spatial resolution of ~ 110 pc at the distances of our target galaxies. This is sufficient to resolve the characteristic spatial separation between independent (i.e. temporally uncorrelated) regions (see Section 4). The angular resolution for each galaxy is listed in Table 1. For the PHANGS-ALMA galaxies, observations have been taken using the 12-m, 7-m, and total power arrays, covering all spatial scales, including short- and zero-spacing

data. For NGC5194, the combination of the PdBI with the IRAM 30-m telescope also enables the recovery of all spatial scales.

We now summarise the main steps of the data reduction of the PHANGS data, which are described in detail in A. K. Leroy et al. (in prep.). After calibration of the $u-v$ data using the ALMA calibration pipeline, line-specific datasets are extracted, for each $u-v$ measurement set and each line of interest, for both the 12-m and 7-m array. These are then regridded to a chosen velocity grid and all measurements for a given spectral line are combined. The cubes are set to have a common channel width of 2.5 km s^{-1} and a typical bandwidth of typically 500 km s^{-1}. The final cubes of the combined 12-m and 7-m data are reconstructed using several iterations of multiscale clean using the algorithm `tclean` in CASA[2] (McMullin et al. 2007, v5.4.0) and are convolved to a round synthesised beam (where the size of the synthesised beam is approximately equal to the original major axis beam size). For the galaxies NGC3627, NGC4254, NGC4321, and NGC5068, which were observed with two separate 150-pointing mosaics, we combine the two mosaics linearly after convolution to match the beams of the two halves. The total power data are reduced using the CASA v5.3.0 software package (see Herrera et al. 2019, for details). For each antenna, the spectra are calibrated, the "OFF" position is subtracted from the spectrum, and a first-order polynomial is fitted and subtracted to correct the baseline. The spectra are then convolved to regularly-gridded data cubes. Finally, the 12m+7m cubes are combined with the total power cubes using CASA's `feather` task, and corrected for the 12m+7m primary beam response. The reduction, imaging and combination of the PAWS data for NGC5194 are presented in Pety et al. (2013). We use the "broad" integrated intensity maps of the PHANGS v1.0 data release (A. K. Leroy et al. in prep.). These maps recover most of the CO emission present in the data cube, including low signal-to-noise flux, resulting in high completeness (Sun et al. 2018), but also higher noise compared to maps using more restrictive masking of the faint CO emission.

---

[2] See https://casa.nrao.edu/

2.3 Star formation tracer

We trace massive star formation using the Hα line, which mostly originates from ionised gas in the vicinity of newly formed massive stars and is therefore commonly used as a tracer of the SFR (see in particular the review by Kennicutt & Evans 2012). We select Hα as a star formation tracer, because it is the most readily observable tracer of young stars ($\lesssim 10$ Myr; e.g. Leroy et al. 2012; Haydon et al. 2018) with the best coverage across our sample, while minimising contamination from other objects. By contrast, the far-UV or near-UV wavelength ranges probe longer time-scales and have larger associated uncertainties (Haydon et al. 2018). The duration of the phase traced by Hα also has the advantage of being only weakly dependent on metallicity, in contrast to UV filters. Infrared (IR) emission (e.g. at 24 μm) is also a common tracer of young star formation and can be used in particular to correct for extinction, which often heavily affects embedded young stars (e.g Kennicutt et al. 2009; Hao et al. 2011). However, IR observations generally do not have sufficient spatial resolution for our science goal (except for the most nearby galaxies), and the duration of the IR emission phase is hard to calibrate due to contamination by evolved stars.

The Hα maps were obtained using ground-based telescopes and include a variety of archival and new data. For NGC628, NGC3627, NGC4254, NGC4303, NGC4535 and NGC5068, we use newly-obtained Hα data using the WFI instrument on the MPG/ESO 2.2-m telescope at La Silla Observatory. We also observe the galaxies in the R-band to enable the continuum subtraction of the Hα data. The details of these observations will be presented in A. Razza et al. (in prep.).

For NGC3351, NGC4321 and NGC5194, we use wide-field high-resolution narrow-band Hα data from the *Spitzer* Infrared Nearby Galaxies Survey (SINGS; Kennicutt et al. 2003). The SINGS galaxies we consider here have been observed using the Kitt Peak National Observatory (KPNO) 2.1-m telescope with the CFIM imager. The data are part of IRSA data release 5.[3] SINGS also includes R-band observations taken with the same telescope under similar observing conditions, which are used to perform the continuum subtraction of the Hα maps. The origin of the Hα data and their spatial resolution are detailed in Table 1.

We now summarise the main steps of the data reduction (for details, see A. Razza et al. in prep. and Schinnerer et al. 2019). For consistency, the same steps have been applied both to the WFI and SINGS data.

Background subtraction. For all galaxies, the sky background is calculated by masking bad pixels and bright sources, and then masking all emission more than 3σ above the median flux of the masked image. This masked image is then smoothed by convolution with a Gaussian that has a dispersion of ~ 3 times the full width half maximum (FWHM) of the angular resolution, in order to mask out all diffuse emission from any bright sources or from the galaxy. We then fit the residual sky background with a plane. In the cases where a good plane fit cannot be obtained (this can happen when the galaxies fill a large fraction of the image), the sky background is taken as the median of the masked image.

Seeing. We fit point sources in both the Hα and R-band background-subtracted images with a Gaussian to determine the seeing of the observations. In cases where the results differ by more than 0.5 pixels, the higher-resolution map is convolved with a Gaussian of the appropriate width to match the lower-resolution data.

Astrometry. The analysis presented in Section 3 carries out a spatial correlation of the CO and Hα maps to determine the relative durations of the evolutionary phases governing the cloud lifecycle. This requires that both maps share a common astrometric system at high accuracy. Extensive tests of the method using simulated data show that for meaningful constraints on the coexistence time-scale of CO and Hα emission (i.e. the 'feedback time-scale' $t_{\rm fb}$, see Section 3), we require that any astrometric offset is less than 1/3 of either the FWHM of the size of the emission peaks (GMCs and H II regions), or of the (synthesised) beam if they are not resolved (Hygate et al. 2019b). The angular resolution of our observations is $\sim 1''$. Therefore, considering the conservative case where emission peaks are not resolved, we adopt a target value of $0.3''$ for the absolute astrometric precision.

The astrometric precision of Hα maps has been assessed by matching stellar sources to the Gaia DR2 catalogue (Gaia Collaboration et al. 2016, 2018) and fitting ~ 50 stars per R-band image, for both the SINGS data and the WFI data. The resulting astrometric precision is $0.1''-0.2''$, which comfortably satisfies our conservative target precision of $0.3''$.

Flux calibration. The flux scale is determined using the median of the flux ratios for a selection of non-saturated stars that are matched between the Hα and the R-band images. Since the R-band continuum has to be subtracted from the Hα line, but the Hα line also contributes to the R-band data, we proceed iteratively to produce the flux-calibrated Hα images. First, the ratio of the relative flux calibration is used to determine the scale of the R-band continuum in the Hα narrow-band image. With this flux basis, we perform a first estimate of the Hα flux, which is then used to determine the contribution of the Hα line to the R-band. We repeat this procedure until the successive continuum estimates differ by less than 1 per cent. To obtain the continuum-subtracted Hα image, this estimate of the continuum is then subtracted from the narrow-band image.

Filter transmission and [N II] *contamination.* We correct the measured Hα flux for the loss due to the filter transmission, using the spectral shape of the narrow-band filter and the position of the Hα line within the filter. It is also corrected for the contribution of the [N II] lines at 654.8 and 658.3 nm to the narrow-band filter flux. For all galaxies in our sample, we first assume a uniform contamination of 30 per cent due to the [N II] lines. This value has been calibrated with high-spectral resolution observations of H II regions in NGC628 with the VLT/MUSE instrument (Kreckel et al. 2016) and comparable results are found from similar observations in NGC3627, NGC4254 and NGC4535, where we measure median ratios [N II]/Hα of 0.30 to 0.32, with standard deviations of 0.05 to 0.06 (K. Kreckel et al. in prep.). In addition, our galaxies span a relatively narrow range in metallicity and our radial coverage is limited to the inner part of the disk (Kreckel et al. 2019) and no trend of the [N II]/Hα ratio with galactocentric radius (or metallicity) is observed (K. Kreckel et al. in prep.), which supports our assumption of a uniform contamination throughout the sample. We then estimate the contribution of the Hα and [N II] lines to the narrow-band image based on the redshift of the galaxy and on the filter transmission curves (see Table 2 in Schinnerer et al. 2019), before finally subtracting the effective contribution from the [N II] lines to the Hα flux.

Extinction. We correct for foreground Galactic extinction using the calibration from Schlafly & Finkbeiner (2011) and assuming a Fitzpatrick (1999) reddening law with $R_V = 3.1$. Note that we

---

[3] More details about these observations can be found at http://irsa.ipac.caltech.edu/data/SPITZER/SINGS/doc/sings_fifth_delivery_v2.pdf

do not carry out a spatially-resolved correction for internal extinction of the Hα line, but instead perform a single, global extinction correction. This is achieved by calculating the global SFR across the field of view using far-UV and 22 μm emission and re-scaling the Hα map accordingly (see Section 2.4 for details). None the less, our lack of a spatially-resolved extinction correction may cause us to underestimate emission from young, embedded HII regions, or fail to detect them at all. In practice, this means that we trace the unembedded phase of star formation, when Hα is visible. Previous studies of nearby galaxies have shown a high spatial correlation between 24μm emission and Hα emission (e.g. Pérez-González et al. 2006; Prescott et al. 2007; Kruijssen et al. 2019). Most importantly, we aim to derive visibility time-scales rather than absolute flux levels. As long as an HII region is visible above the noise level, it is included in our analysis. The absolute brightness of a region is only used as a weight when calculating the population-averaged gas-to-SFR flux ratio (see Section 3).[4]

Even if we might expect some impact of extinction on the local Hα flux, we stress that we calibrate the measured timeline for cloud evolution and star formation based on the duration of the unembedded phase of star formation (see Section 3.2). As a result, neglecting the embedded star-formation phase during which Hα is not yet visible would only result in underestimating the duration of the overlap between the gas and the young stellar phases. However, it would not affect the cloud lifetime, because the sum of the durations of the inert CO-bright phase and the overlap phase is unaffected by extinction, even if the division between both phases may change. For the same reason, the total duration of the evolutionary cycle would not change either. If an embedded Hα phase is present, Haydon et al. (2019) demonstrate that this could potentially affect the measured duration of the overlap phase, but only for global gas surface densities larger than $20\,\mathrm{M}_\odot\,\mathrm{pc}^{-2}$ at solar metallicity. This conclusion is based on a numerical simulation that over-predicts the effects of extinction and thus represents a lower limit. Extinction thus affects less than half of our sample (see Figure B3 – galaxies that reside above this (highly conservative) threshold of $20\,\mathrm{M}_\odot\,\mathrm{pc}^{-2}$ across more than 4 kpc in galactocentric radius are NGC3627, NGC4254, NGC4303, and NGC5194). We will quantify the impact of extinction further in future works (M. Chevance et al. in prep.; J. Kim et al. in prep.).

Finally, sources other than HII regions generating Hα emission (such as supernova remnants) might contribute to the Hα flux and thus contaminate our measurements. However, these generally have considerably smaller sizes and lower luminosities than HII regions (e.g. Kreckel et al. 2018). As a result, their contribution to the flux-weighted average Hα flux in each aperture is negligible – Peters et al. (2017) quantify this using three-dimensional radiation-hydrodynamical simulations and estimate that shocks contribute less than 10 per cent of the total Hα flux. A large-scale reservoir of Hα emission tracing diffuse ionised gas is also commonly observed in galaxies (e.g. Monnet 1971; Dettmar 1990; Hoopes et al. 1996; Oey et al. 2007; Kreckel et al. 2016; Lacerda et al. 2018). We describe how we separate this diffuse emission reservoir from the compact emission tracing HII regions in Section 3.4.

The final CO and Hα images of all nine galaxies are shown in Figure 1. The figures also indicate the field of view used in the

analysis (this is mostly limited by the field of view of the CO observations, but it also excludes some map edges where the noise is high, e.g. in NGC628 and NGC5194), the galactic centres and bar regions (which are excluded by eye because of blending effects, see below), and the foreground stars and background galaxies that have been masked. These maps are used throughout this paper.

2.4 Global SFR

As noted above, Hα line emission can suffer from extinction, implying that the total SFR derived from Hα alone is underestimated. To correct for extinction, we calculate the SFR from multi-wavelength mapping, combining the Galaxy Evolution Explorer (GALEX) far-ultraviolet band (far-UV; 155 nm) and the Wide-field Infrared Survey Explorer (WISE) W4 band at 22 μm maps (Leroy et al. 2019), convolved to 15″ angular resolution. To convert the observed flux levels to a SFR, we use the SFR prescription provided by Kennicutt & Evans (2012) and Jarrett et al. (2013). The SFR measured this way accross the fields of view used for our analysis are listed in Table 3. Finally, we determine the appropriate conversion factor between the flux in the Hα map and the total extinction-corrected SFR from GALEX and WISE across the same field of view. We note that this conversion factor has no impact on the evolutionary timeline derived in Section 4 and only plays a role in calculating the integrated star formation efficiency per star formation event (see Section 3.2).

3 UNCERTAINTY PRINCIPLE FOR STAR FORMATION

We now turn to a discussion of our analysis method. We first introduce the general concept and framework, before discussing how it is applied specifically to our sample of nine nearby disc galaxies. This section also includes a summary of the adopted input parameters of the analysis, a discussion of how we filter diffuse emission from the galaxy maps, and a description of how the evolutionary timelines are calibrated.

3.1 General concept

Inspired by the interpretation first proposed by Schruba et al. (2010), recent work has now demonstrated that the observed small-scale scatter around the global star formation relation (e.g. Bigiel et al. 2008; Blanc et al. 2009; Onodera et al. 2010; Schruba et al. 2010; Leroy et al. 2013; Kreckel et al. 2018; Kruijssen et al. 2019) can be understood by assuming that individual regions in a galaxy independently undergo an evolutionary lifecycle during which a molecular cloud assembles, collapses, forms stars, and is disrupted by feedback, with molecular gas and SFR tracers probing different evolutionary phases (e.g. Feldmann et al. 2011; Kruijssen & Longmore 2014). On small scales, such an independent region is observed at a specific time during this cycle, and therefore does not necessarily satisfy the galactic star formation relation: it is not possible to simultaneously observe a young stellar cluster and the progenitor cloud from which it formed. When focusing on a young, unembedded star-forming region, most of the molecular gas has been consumed or disrupted, leaving an excess of SFR flux compared to the average gas-to-SFR flux ratio. By contrast, when focusing on a non-star-forming GMC, an excess of molecular gas is measured relative to the galactic-scale balance between gas and SFR emission. This means that the gas-to-SFR flux ratio (or gas depletion

---

[4] The fluxes of all CO and Hα regions are summed before calculating the gas-to-SFR ratio. As a result, bright regions contribute more to these total fluxes. In the following, we therefore refer to our measurements as 'flux-weighted averages'.
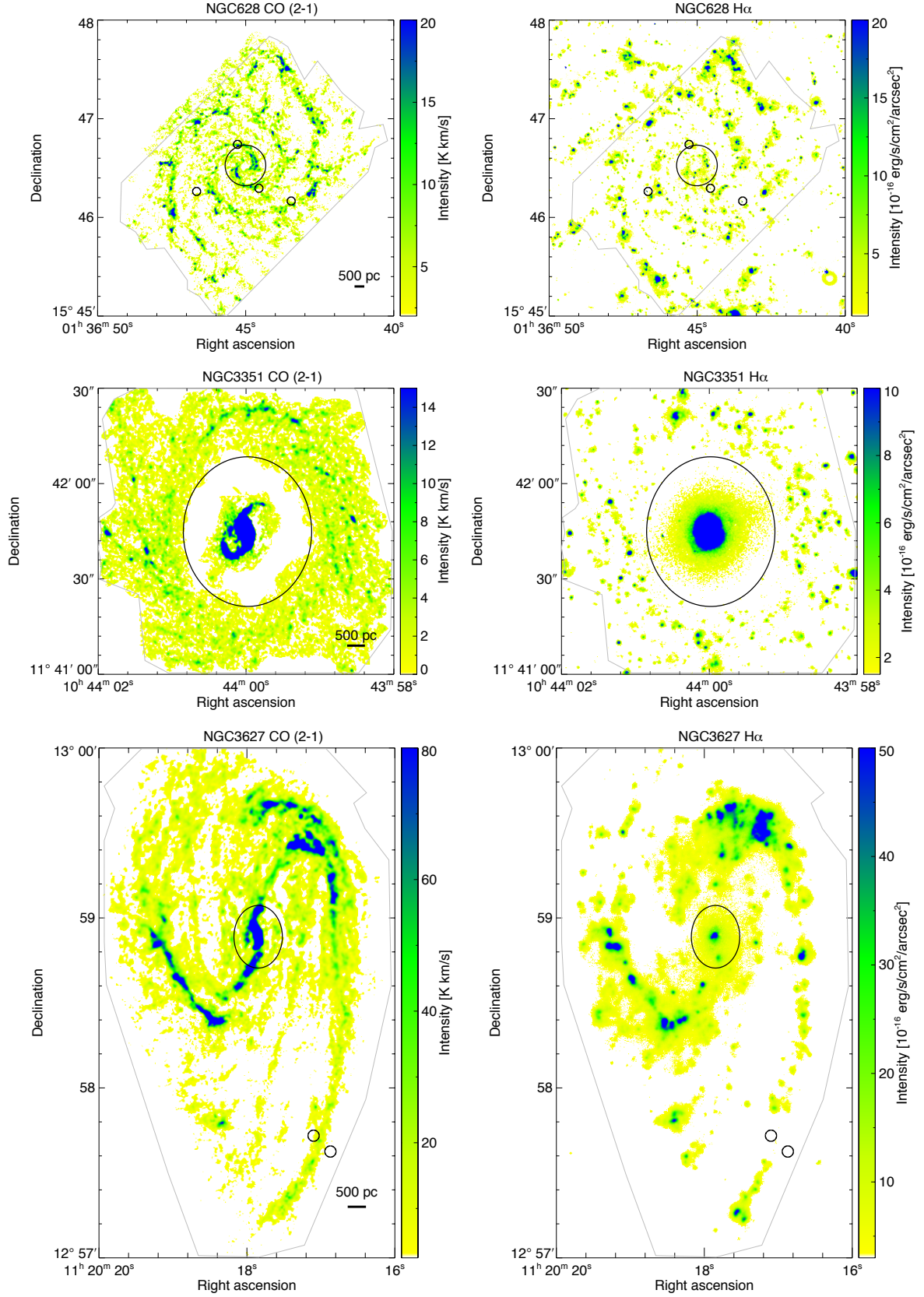
Figure 1. Maps of the nine observed galaxies. The left column shows the ^{12}CO integrated intensity maps ($J = 1-0$ transition for NGC5194, $J = 2-1$ transition for the other galaxies of the sample; in units of K km s^{-1}) and the right column shows the Hα intensity maps (in units of 10^{-16} erg s^{-1} cm^{-2} arcsec^{-2}). To minimise the effects of blending between independent regions, the centre of each galaxy (black central ellipse) is identified by eye and excluded from the analysis. We also mask foreground stars and background galaxies (black circles). The analysis of this work has been performed in the area delineated by the grey line, where both CO and Hα have been observed (the field of view is primarily limited by the size of the CO map, excluding map edges with high noise when necessary). A linear scale of 500 pc is indicated in each of the CO images.
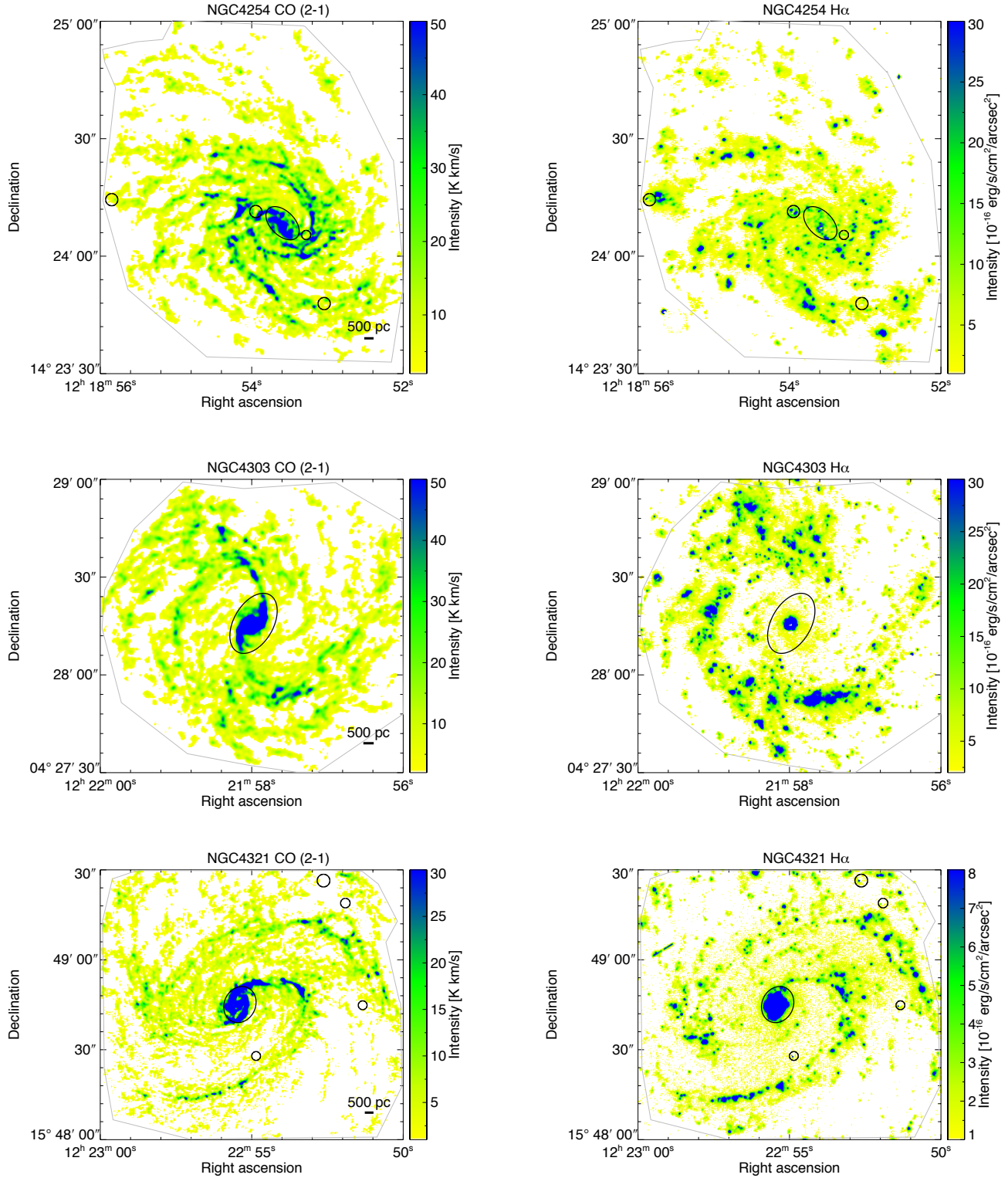
Figure 1 – *continued*

time) depends strongly on the local evolutionary state of the ISM (Schruba et al. 2010; Kruijssen & Longmore 2014).

In the context of the above interpretation, the observed scatter around the star formation relation on small scales results from the statistically-insufficient sampling of the different star forma-

tion phases. Conversely, the strong correlation between gas mass and SFR observed on galactic scales results from averaging over many regions that collectively sample the full evolutionary lifecycle spanning the successive phases of star formation. In this work, we use the statistical method first presented in Kruijssen & Longmore
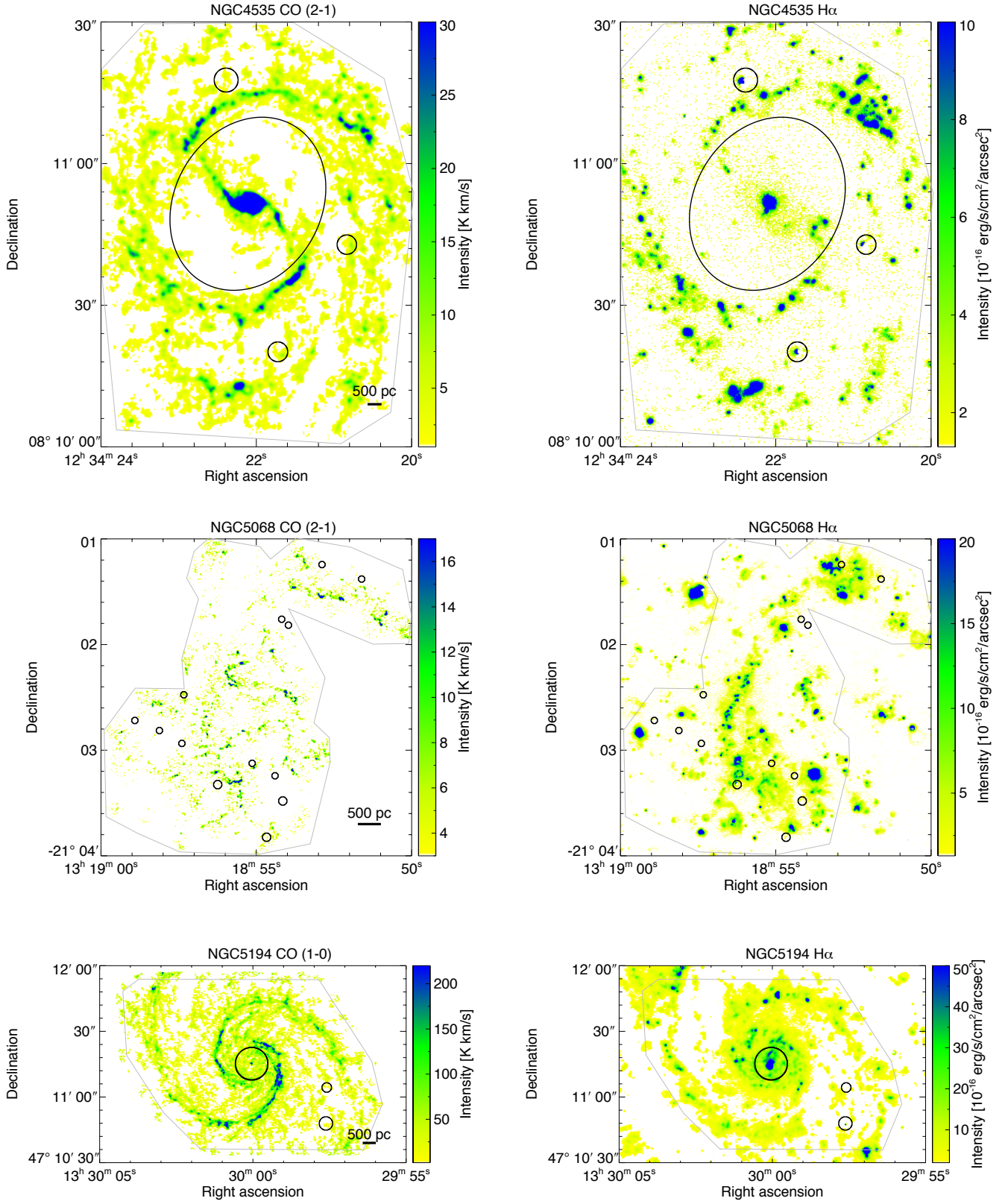
Figure 1 – *continued*

(2014) and developed further in Kruijssen et al. (2018), which exploits the multi-scale nature of the star formation relation by translating the small-scale variations of the gas-to-SFR flux ratio into the underlying evolutionary timeline of cloud formation, star formation and feedback, as well as deriving the physical quantities describing star formation on the cloud scale.

The evolutionary timeline for star formation is constituted by the lifetime of molecular clouds, t_{gas}, and the duration of the young stellar phase, t_{star}. Here and in the following, we use 'gas' and 'star' to refer to molecular gas clouds and young H II regions respectively. These two phases can overlap in time, which defines the duration of the feedback phase, t_{fb}, during which stars and gas coexist within a region. The total duration of this evolutionary timeline, τ, is therefore given by:

$$\tau = t_{star} + t_{gas} - t_{fb}. \tag{1}$$

According to this definition, t_{star} is the complete duration over which the SFR tracer is visible, such that it exceeds the lifetime of massive stars if star formation proceeds over a non-zero timescale. Likewise, t_{gas} represents the complete duration over which the cloud is visible in the gas tracer. Finally, t_{fb} is the time between the moment at which the SFR tracer first becomes visible and the moment at which the gas tracer has completely dispersed. Each of these phases can be probed by a particular observational tracer. Schematically, across a galaxy, the relative abundance (or rarity) of the tracers associated with each of the above phases reflects their relative duration. Therefore, by measuring how common or how rare flux peaks of a given tracer are, we are able to define a relative lifetime between successive phases of the star formation cycle.

In practice, we perform our measurement by centring circular apertures of a certain size on molecular clouds or young H II regions, and measuring the relative change of the gas-to-SFR flux ratio within these apertures with respect to the galactic average as the aperture size is varied (see e.g. Supplementary Video 1 of Kruijssen et al. 2019). At large aperture sizes (centred on either emission peak), the galactic average gas-to-SFR flux ratio is recovered. The relative deviation (or 'bias') of the gas-to-SFR flux ratio measured at smaller aperture sizes relative to the galactic average directly probes the relative durations of the phases captured by the two tracers. For instance, when placed on the numerous emission peaks of a long-lived tracer, even the smallest apertures will cover most of the galaxy, and will therefore also encompass a large fraction of emission peaks of the other tracer. The resulting flux ratio will be close to the galactic average, resulting in a small bias. By contrast, when placed around the rare emission peaks of a short-lived tracer, small apertures will cover only a small part of the galaxy, and therefore only a small fraction of the emission peaks of the other tracer, leading to a large bias of the flux ratio compared to the galactic average.

To measure the above time-scales for our nine target galaxies, we systematically fit the model from Kruijssen et al. (2018) to the observed gas-to-SFR flux ratios measured as a function of the aperture size, when focusing apertures either on molecular gas emission peaks or on SFR emission peaks. The general steps of the procedure used for this analysis are described in Section 3.2 and are summarised as follows. We first select two tracers of causally-related phases in a Lagrangian timeline, i.e. any individual region visible in one of the tracers will eventually emit in the other tracer.[5]

---

[5] This does not preclude multiple visibility cycles of the first of both tracers before becoming visible in the second, which happens if clouds dis-

Flags	Value	Notes
mask_images	1	Mask images on
mstar_int	1	Mask the centre of the galaxy
mgas_ext	1	Mask outer parts of the galaxy, where CO is not detected

Table 2. Flags set to a different value than the default (as listed in table 1 of Kruijssen et al. 2018).

Emission peaks are identified in this pair of maps and the gas-to-SFR flux ratio is measured around these peaks, for a range of different aperture sizes. We then fit a statistical model to these measurements to constrain its three free parameters (these are t_{gas}, t_{fb}, and the region separation length λ, see below), propagate the errors on the derived parameters characterising the evolutionary timeline, and derive secondary quantities including their uncertainties. The results of applying this analysis to our galaxy sample are presented in Section 4.

3.2 Application of analysis method to our galaxy sample

Our analysis method is formalised in the HEISENBERG code, which is presented and described in detail by Kruijssen et al. (2018). Here we summarise the main steps of the method to measure the duration of the gas phase (t_{gas}), the duration of the feedback phase (t_{fb}), and the typical separation length between independent regions (λ).

We provide two galaxy maps of the tracers characterising the evolutionary timeline of interest (CO and Hα, see Section 3.3). Both maps are convolved to the same resolution and matched to the same pixel grid before running the analysis. We specify as needed if the maps should be partially masked or a galactocentric radius cut should be applied. We define a central region by eye to exclude the galactic centre (where independent regions are the most prone to blending). For NGC3351 and NGC4535, this mask is extended to cover the bar region, because their strong bars have cleared most of the corresponding area of molecular gas and star formation. We also exclude the galaxy outskirts beyond the galactocentric radius of the outermost emission peak identified across both maps (see below). The masking also takes into account the edges of the field of view. If any, masks or radial cuts are applied to both maps. The masked regions (galaxy outskirts, central region, foreground stars and background galaxies) are visible as ellipses in Figure 1. To enable a straightforward measurement of the gas-to-SFR flux ratio (here CO-to-Hα flux ratio) at various aperture sizes, we next use a top-hat kernel to convolve both maps to N_{ap} different spatial scales, spaced logarithmically between a minimum ($l_{ap,min}$) and maximum ($l_{ap,max}$) aperture size (see Table 3).

The emission peaks on which the apertures are placed are

perse dynamically without forming massive stars. However, we find in Section 4 that this is unlikely to occur, because the integrated cloud lifetimes are similar to a (cloud-scale or galactic) dynamical time-scale, leaving insufficient time for multiple cycles. The generality of the method also allows for multiple generations of (or temporally extended) star formation within a single cloud, by allowing $t_{fb} > 0$. Because the method identifies 'independent regions', which reside on an evolutionary timeline independently of their neighbours, these regions may contain multiple smaller H II regions or molecular substructure if these have correlated evolutionary ages. For instance, this would apply to a group of H II regions born from the same molecular cloud.

Table 3. Main input parameters of the analysis for each galaxy. The other parameters use the default values as listed in table 2 of Kruijssen et al. (2018).

Quantity	NGC628	NGC3351	NGC3627	NGC4254	NGC4303	NGC4321	NGC4535	NGC5068	NGC5194
D [Mpc][a]	9.77	10.00	10.57	16.80	17.60	15.20	15.80	5.16	8.60
i [°][b]	8.70	45.14	56.49	35.27	19.99	39.10	42.12	26.95	21.00
ϕ [°][b]	20.82	193.24	174.04	68.51	310.60	157.65	179.35	348.96	173.0
$l_{\mathrm{ap,min}}$ [pc]	50	80	100	140	150	130	130	30	70
$l_{\mathrm{ap,max}}$ [pc]	4800	4900	5400	10700	7400	6100	7200	4000	3000
N_{ap}	15	15	15	15	15	15	15	15	12
$N_{\mathrm{pix,min}}$	10	10	10	10	15	10	10	15	15
$\Delta \log_{10} \mathcal{F}_{\mathrm{star}}$[c]	1.00	1.60	2.10	2.30	2.50	1.60	2.30	1.70	2.30
$\delta \log_{10} \mathcal{F}_{\mathrm{star}}$[c]	0.06	0.25	0.20	0.20	0.15	0.25	0.25	0.50	0.20
$\Delta \log_{10} \mathcal{F}_{\mathrm{gas}}$[c]	0.70	1.10	2.20	1.90	2.00	1.60	2.00	1.20	1.40
$\delta \log_{10} \mathcal{F}_{\mathrm{gas}}$[c]	0.03	0.15	0.10	0.10	0.15	0.15	0.20	0.60	0.15
$t_{\mathrm{star,ref}}$ [Myr]	4.35	4.27	4.37	4.34	4.37	4.29	4.38	4.53	4.19
$\sigma(t_{\mathrm{star,ref}})$ [Myr][d]	0.16	0.17	0.16	0.16	0.16	0.16	0.16	0.14	0.17
SFR [$M_\odot$ yr^{-1}][e]	0.87	0.22	2.81	4.50	4.37	2.50	0.92	0.22	1.91
σ(SFR) [$M_\odot$ yr^{-1}][d]	0.17	0.04	0.56	0.90	0.87	0.50	0.18	0.04	0.38
$\log_{10} X_{\mathrm{gas}}$[f]	0.81	0.67	0.33	0.78	0.82	0.45	0.82	0.92	0.59
$\sigma_{\mathrm{rel}}(X_{\mathrm{gas}})$[d]	0.40	0.63	0.50	0.31	0.50	0.50	0.50	0.50	0.50
$n_{\lambda,\mathrm{iter}}$	10	10	12	12	12	12	12	10	12

[a] Distances adopted from A. K. Leroy et al. (in prep.) and references therein.

[b] Inclinations and position angles are preliminary and will be presented by Lang et al. (2019).

[c] The parameters for the peak identification listed here are valid for the diffuse-emission filtered maps (see Section 3.4). Different values are used for the first iteration during which emission peaks are identified in unfiltered maps, but we have verified that the choice of these initial parameter values does not significantly affect our results.

[d] Standard error. The subscript 'rel' indicates a relative error.

[e] This is the SFR measured from GALEX and WISE (see Section 2.4) across the field of view considered in this paper, rather than of the entire galaxy.

[f] The gas conversion factor corresponds to $\alpha_{\mathrm{CO}(1-0)}$ for NGC5194 and to $\alpha_{\mathrm{CO}(2-1)}$ for all of the other galaxies, in $M_\odot$ (K km s^{-1} pc^2)$^{-1}$.

identified in both maps at the best common resolution, using the algorithm CLUMPFIND (Williams et al. 1994). In brief, the CLUMPFIND algorithm identifies closed contours for a given set of flux level intervals, defined by a flux range below the maximum flux level, $\Delta \log_{10} \mathcal{F}$, and an interval between flux levels, $\delta \log_{10} \mathcal{F}$. In Table 3, these carry subscripts 'star' and 'gas', referring to the Hα and CO maps, respectively. We set the minimum number of pixels within a closed contour necessary for a peak to be identified to $N_{\mathrm{pix,min}}$, to avoid selecting point sources, and the position of the peak is then defined as the pixel with the maximum flux value within this closed contour. For each of the N_{ap} spatial scales, we place apertures on each peak and measure the gas and SFR fluxes within these apertures, as well as the effective average aperture area, which may be smaller than the intended aperture area due to the potential presence of masked pixels.[6] This results in four fluxes per aperture size: the total summed CO flux and total summed Hα flux across the entire sample of CO peaks, and the total summed CO flux and total summed Hα flux across the entire sample of Hα peaks. From these summed fluxes, we then calculate the CO-to-Hα flux ratio around CO peaks or around Hα peaks, at each given aperture size. We then calculate the bias relative to the galactic averaged CO-to-Hα flux ratio for each set of peaks. As a function of the aperture size, this bias for CO and Hα emission peaks takes the characteristic shape of a 'tuning fork' diagram (see Section 4).

In practice, placing an aperture on each peak would result in counting at least some of the pixels multiple times, because some apertures overlap. This occurs for large aperture sizes and in regions with a high number density of peaks, and leads to inaccurate

measurements of the flux ratio bias due to over-representing regions at high number densities. To avoid this effect, the flux ratio bias is calculated 1000 times on different Monte-Carlo realisations of sub-samples of independent, non-overlapping apertures, for each peak type and aperture size. These Monte-Carlo realisations contain the maximum number of non-overlapping apertures obtained by going through the full list of apertures in a different order each time and rejecting those that overlap with any apertures that have already been drawn. The final CO-to-Hα flux ratio is an average over all of the Monte-Carlo realisations. The uncertainties on the flux ratio bias measurements account for both the finite sensitivity and resolution of the maps, as well as for the intrinsic stochasticity of the gas mass and SFR of the different regions. These are then translated into effective uncertainties, which take into account the covariance between the flux measurements at different aperture sizes, and are used when fitting the statistical model to the tuning fork diagram. In the tuning fork diagrams presented in Section 4, we show both the individual and effective uncertainties.

The next step is to fit these measurements with a statistical model linking the flux ratio biases to the duration of the different phases of the evolutionary timeline. The mathematical expressions for the flux biases have been derived in Kruijssen & Longmore (2014, Appendix C) by considering a random spatial distribution of point-like regions at random positions on the evolutionary timeline, and taking into account the possible flux evolution between regions in isolation and regions within which both phases coexist. The model was since updated to account for a spatially-extended profile of the regions. As stated above, the model depends on three independent quantities: t_{gas}, t_{fb} and λ. As a function of these quantities, it predicts how the CO-to-Hα flux ratio changes as a function of the aperture size when focusing apertures on regions bright in

[6] For instance, apertures that partially fall outside of the field of view have their area reduced accordingly.

CO or in Hα. We refer to Kruijssen et al. (2018, sect. 3.2.11) for the complete details of the model and note that a concise summary is provided in the Methods section of Kruijssen et al. (2019). The model is fitted to the data points by minimising the reduced-χ^2 over the above three free parameters. These three quantities are non-degenerate, as they affect the predictions of the model in different ways (see Section 4.1). The resulting three-dimensional probability distribution function (PDF) is marginalised to obtain the one-dimensional PDF for each free parameter. The uncertainty on each free parameter is defined as the 32nd percentile of the part of the PDF below the best-fitting value, and the 68th percentile of the part of the PDF above the best-fitting value. For a Gaussian PDF, this reduces to the 1σ uncertainties. We provide the full PDFs of our measured cloud lifetimes in Section 4, finding that they are often close to log-normal.

Fundamentally, the above analysis only measures relative time-scales, such that the duration of one of the two phases needs to be provided as a reference time-scale in order to convert the relative time-scales into absolute ones. We use the calibration of the Hα-emitting phase by Haydon et al. (2018) to convert the relative duration of each phase to an absolute timeline, using a reference timescale ($t_{\rm star,ref}$). This calibration has been carried out in a self-consistent way, by applying the HEISENBERG code to pairs of simulated galaxy maps. The input maps used there are a mass surface density map of star particles within a specified age range (of which the duration is then known)[7] and a synthetic emission map of a star formation tracer (Hα or UV emission for various filters), the duration of which is then an output of the method. Haydon et al. (2018) generate these maps by post-processing their hydrodynamical disc galaxy simulations with the stellar population synthesis (SPS) code SLUG2 (da Silva et al. 2012, 2014; Krumholz et al. 2015). They sample stars stochastically from a Chabrier (2005) initial mass function (IMF) and use Geneva stellar evolutionary tracks (Schaller et al. 1992) with STARBURST99 spectral synthesis (Leitherer et al. 2014).[8]

Haydon et al. (2018) calibrate $t_{\rm star,ref}$ using an SPS model describing an instantaneous burst of star formation, to avoid any dependence on the duration of star formation, which likely varies in nature. This implies that the reference time-scale ($t_{\rm star,ref}$) differs from the total duration of the Hα-bright phase ($t_{\rm star}$) by excluding the feedback phase. This choice of defining $t_{\rm star,ref} = t_{\rm star} - t_{\rm fb}$ thus allows for a continuous star formation history, in which new massive stars can form as long as the region contains molecular gas, and the 'clock' defining $t_{\rm star,ref}$ only starts when the last massive star forms. The exact value of $t_{\rm star,ref}$ varies somewhat with metallicity (see Section 3.5) and the sampling of the IMF. In this work, we account for the dependence of this time-scale on metallicity. Its dependence on IMF sampling is weak in general, and is negligi-

ble for the range of region masses probed by our observations (see section 6 of Haydon et al. 2018). For reference, the total Hα visibility time-scales (i.e. $t_{\rm H\alpha} \equiv t_{\rm star} = t_{\rm star,ref} + t_{\rm fb}$) obtained in this work range from $5-9$ Myr (see Section 4), broadly consistent with previous studies (e.g. Kennicutt & Evans 2012; Leroy et al. 2012).

Finally, we calculate a wide variety of derived quantities from the three free parameters, including their PDFs. Among others, these include the total star formation tracer lifetime ($t_{\rm star} \equiv t_{\rm star,ref} + t_{\rm fb}$), the total duration of the evolutionary timeline (τ), the region radii ($r_{\rm H\alpha}$ and $r_{\rm CO}$), the region size-to-separation ratios or filling factors ($\zeta_{\rm H\alpha}$ and $\zeta_{\rm CO}$), the feedback outflow or phase transition front velocity ($v_{\rm fb}$), the global gas depletion time ($t_{\rm depl}$), the integrated star formation efficiency per star formation event ($\epsilon_{\rm sf}$), and the region-scale mass loading factor ($\eta_{\rm fb}$). How these quantities are derived from the three free parameters is detailed in section 3.2.14 of Kruijssen et al. (2018).

In this paper, we apply the HEISENBERG code to a sample of nine galaxies, and derive all of the quantities mentioned above. However, we will mainly focus our discussion on the molecular cloud lifetime (Sections 4 and 5), while future papers will present a detailed investigation of the other derived quantities and their dependence on galactic environment. Before discussing the results of our analysis, we now first describe the input parameters of the HEISENBERG code used in this paper, as well as how we determine a number of observational quantities that are required as input for the measurement of the molecular cloud lifetime.

3.3 Input maps and parameter choices

The requirement that the tracers of the different phases represent causally-related phases along a Lagrangian timeline means that the tracers must be chosen with care. Each independent region needs to be detectable in both tracers at some point in its lifetime, but not necessarily simultaneously. Based on the strong correlation between molecular gas and star formation on galactic scales, we therefore consider the timeline from molecular gas (traced by CO) to young stars (traced by Hα), under the assumption that young stars form from molecular gas.[9] This means that GMCs hosting unembedded massive star formation will be visible in both tracers simultaneously.

For the analysis presented here, we trace the first phase (the 'gas' phase) with the emission of CO(2-1), except for NGC5194, for which we use the high resolution CO(1-0) PAWS map. In the following, we will use the notation $t_{\rm CO}$ to represent the duration of the gas phase (instead of the more general notation $t_{\rm gas}$), which in this context refers to the molecular cloud lifetime. This choice of tracer defines the structures of which the lifetimes are measured: we assume that CO and molecular gas coexist in time and space, so that CO emission can be used to trace molecular gas. As such, the molecular cloud lifetimes presented here represent the 'CO visibility' lifetimes of molecular clouds, i.e. the flux-weighted, population-averaged time for which an individual molecular cloud emits in CO, for the molecular cloud population above our point

---

[7] By using a mass surface density map with a pre-defined stellar age range as the 'reference map' in these calibration experiments, we ensure that the calibration is largely insensitive to the baryonic physics of the simulation. See Haydon et al. (2018) for details.

[8] Binaries are not included in the adopted SPS model, but they may prolong the emission of ionising photons and increase $t_{\rm star,ref}$, because stars in binaries may be tidally stripped, thus exposing their hot interiors (Eldridge et al. 2017; Götberg et al. 2019). However, we do not expect this to substantially change our results, because binaries only increase the ionising flux at times when it has already dropped considerably, i.e. well after the nominal value of $t_{\rm star,ref}$ derived by Haydon et al. (2018), and are unable to boost it to values similar to the ionising flux predicted at $t < t_{\rm star,ref}$ (see fig. 4 of Götberg et al. 2019).

[9] Note that we do not assume the opposite, i.e. not every CO emission peak is assumed to host massive star formation at any point of its life. However, the short cloud lifetimes reported in Section 4 imply that clouds only live for approximately one (cloud-scale or galactic) dynamical time before being associated with Hα emission, which strongly suggests that most CO peaks in our maps do eventually host massive star formation. See the Methods section of Kruijssen et al. (2019) for further discussion.

source sensitivity limit of $\sim 10^5\,M_\odot$. Beyond this definition, an important advantage of the method used here is that the measured time-scales do not explicitly depend on the α_{CO} conversion factor, which is uncertain in extragalactic environments (see e.g. Kennicutt & Evans 2012; Bolatto et al. 2013). Once a molecular gas tracer has been chosen, the assumption of a particular α_{CO} conversion factor or of a ratio CO(2-1)/CO(1-0) has no impact on the derived molecular cloud lifetime, nor on the other primary derived quantities, t_{fb} and λ (see also Section 3.5). This insensitivity to conversion factors arises, because the flux observed near emission peaks is divided by the kpc-scale flux of the same tracer, which means that the conversion factor cancels out on average. However, if there is a considerable α_{CO} spread within the galaxy, the flux-averaging nature of our method implies that the measurements may be biased towards regions of low α_{CO} (high flux). For the shallow metallicity gradients shown in Figure B3, we expect this effect to be minor.

We select Hα as a star formation tracer for the second phase and use it to calibrate the obtained timelines. In the following, we will use the notation $t_{H\alpha}$ to represent the duration of the young stellar phase (instead of the more general notation t_{star}). The duration of the young stellar phase probed by (continuum subtracted) Hα has been calibrated by Haydon et al. (2018) to be $t_{H\alpha,ref} = 4.3$ Myr at solar metallicity, for the calibration setup described in Section 3.2. In Section 3.5, we quantify the slight dependence of this time-scale on metallicity; the reference time-scales listed in Table 3 account for the gas mass-weighted mean metallicity of each galaxy.

It is necessary that the observed tracer maps have a spatial resolution sufficient to resolve the separation length λ between independent regions, and that the inclination of the galactic disc is moderate ($i \lesssim 75°$) to avoid confusion between emission peaks. We also assume that the regions are randomly distributed in each other's vicinity, such that the distribution of neighbouring regions is accurately described in two-dimensions, without dominant one-dimensional structures.[10] These requirements, as well as the other guidelines listed in Kruijssen et al. (2018, section 4.4), have been determined based on experiments on simulated galaxies. We demonstrate in Section 6.1 that our analysis satisfies these guidelines.

The tracer maps of the two consecutive phases are the primary inputs of the HEISENBERG code. Tables 2 and 3 present a selection of flags and input parameters used for our galaxy sample. The other flags and input parameters of the HEISENBERG code not listed here have been set to their default values as listed in tables 1 and 2 of Kruijssen et al. (2018). We note that, while we have optimised the input parameters of the model (such as N_{ap} and $l_{ap,min}$) and of the peak identification ($\Delta \log_{10} \mathcal{F}$ and $\delta \log_{10} \mathcal{F}$) to each of the galaxies in our sample, small variations of these numbers do not strongly affect the constrained quantities, as long as the physically relevant

---

[10] Because the de-correlation between CO and Hα takes place below a size scale $\sim \lambda$ of typically a few hundreds of pc (see Section 4), our methodology is largely insensitive to galactic structure. This means that strong morphological features on the galactic scale do not typically break the assumption of local spatial randomness and two-dimensionality. Even local evolutionary stream lines (e.g. across spiral arms, Meidt et al. 2013; Querejeta et al. 2019; Schinnerer et al. 2017) are accommodated by the method, as long as the increase of the number of neighbouring emission peaks with size scale proceeds roughly as expected for a two-dimensional distribution. We have tested the method on simulated galaxies with a flocculent spiral structure to demonstrate this (Kruijssen et al. 2018).

peaks are identified and the criteria listed in Section 6.1 are satisfied.

3.4 Diffuse emission

The presence of diffuse emission on large scales in the maps of the observed tracers affects the measured cloud lifetime, by adding a reservoir of emission on scales larger than λ that does not belong to the emission peaks identified. This diffuse emission can have different physical origins for different tracers, as described below (e.g. diffuse molecular gas not forming massive stars, ionising photons leaking from HII regions and therefore not spatially associated with a star-forming region), and does not participate in the evolutionary cycle of emission peaks described in Section 3 (Kruijssen et al. 2018; Hygate et al. 2019b). This large-scale emission therefore needs to be filtered out of the observed maps to ensure an unbiased measurement of the different phases of the molecular cloud lifecycle.

In the case of Hα, the leaking of ionising photons outside of the HII regions where they are produced leads to the presence of a diffuse Hα component in the observed maps (e.g. Mathis 1986; Sembach et al. 2000; Wood et al. 2010). Other contributions to this diffuse ionised gas include ionisation by post-asymptotic giant branch stars (e.g. Binette et al. 1994; Sarzi et al. 2010; Flores-Fajardo et al. 2011), dust scattering (Seon & Witt 2012), shocks (Pety & Falgarone 2000; Collins & Rand 2001), and the presence of small, unresolved HII regions (Lee et al. 2016). Different methods can be applied to remove the contribution from the diffuse ionised gas, depending on its assumed origin. The simplest methods consist of subtracting an estimate of the diffuse emission based on a smoothed version of the star-formation tracer (e.g. Hoopes et al. 1996; Greenawalt 1998) or applying a fixed intensity threshold to remove all emission lower than a given value (e.g. Blanc et al. 2009; Kaplan et al. 2016). Including information about the spatial extent of HII regions can also help decomposing the emission into a diffuse background and compact sources (e.g. Thilker et al. 2002; Oey et al. 2007). However, while most of these approaches are physically motivated, they ultimately rely on subjective choices regarding the intensity threshold, the smoothing scale, the size of HII region and/or the scaling factor applied to the smoothed map. We note that if the main source of diffuse Hα emission results from the leaking of ionising photons, this flux should not be omitted from the global SFR when calculating the star formation efficiency (see Section 4.3.4).

In the case of CO, a diffuse component on large scales can be emitted by truly diffuse, unbound molecular gas, or by an ensemble of small mass, unresolved clouds. Our observations have the point source sensitivity to detect cloud masses down to $10^5\,M_\odot$ which for the star formation efficiencies reported in Section 4 corresponds to a few $10^3\,M_\odot$ in stellar mass over the duration of an evolutionary cycle τ. Few massive stars are expected in lower-mass regions (e.g. Weidner & Kroupa 2006; da Silva et al. 2012) and our measurements represent flux-weighted population averages (Kruijssen et al. 2018). Because the cloud mass function follows an exponentially truncated power law with a slope below the truncation mass ($M_{GMC,\star}$) that is shallower than -2 (e.g. Freeman et al. 2017, E. Rosolowsky et al. in prep.), this means that the lifecycles inferred here mostly describe the cloud population near the truncation mass. For the galaxies considered here, this is $M_{GMC,\star} = 10^6 - 10^7\,M_\odot$ (E. Rosolowsky et al. in prep.). We can therefore filter out the lower

mass clouds, which do not strongly contribute to the flux-weighted average evolutionary cycle constrained here.[11]

For both the CO and Hα maps, we filter out diffuse emission from the input images using the method of Hygate et al. (2019b), which uses the mean separation length between independent regions obtained with HEISENBERG (λ) to iteratively filter out emission in Fourier space on scales larger than a fixed multiple of the separation scale. This approach avoids making assumptions about the physical scale of HII regions or a flux threshold to separate HII regions from the diffuse background. Instead, it uses the characteristic separation length between independent regions as a physically-motivated scale for separating the diffuse emission from compact emission. This is achieved by filtering out the emission in Fourier space on spatial scales larger than those of the independent regions undergoing the evolutionary lifecycle of interest, and doing this consistently for the SFR map and the gas map. While this approach does not presume a fixed scale for diffuse emission, it does a posteriori introduce a spatial scale over which diffuse emission is thought to exist. However, given that the separation length is larger than the typical HII region size by definition, this should not introduce a large bias (even though it may not remove all of the diffuse emission). A key advantage of this method is that it also deals well with a diffuse background that varies across the map, as long as the variations manifest themselves over a size scale larger than the region separation length.

The influence of the size and type of filter used are fully described in Hygate et al. (2019b). For our analysis, we use a Gaussian high-pass filter, which is the best compromise between the selectivity of the filter and the undesired appearance of artefacts around compact regions. We then set the characteristic cut-off wavelength of this Gaussian filter to be between $10-12 \times \lambda$ (see Appendix A for details), with λ the characteristic separation length between independent clouds or star-forming regions, as measured with our analysis method (see Sections 3 and 4). The multiples of λ ($n_{\lambda,\mathrm{iter}}$) used are listed in Table 3. This choice of $n_{\lambda,\mathrm{iter}}$ ensures that the large-scale diffuse emission is filtered, while minimising the impact of the filter on the compact regions (Hygate et al. 2019b). After filtering, we again measure λ for the filtered maps and iterate this process until convergence is reached (when λ varies by less than 5 per cent from the previous iteration, for at least four successive iterations). The resulting compact emission fractions ($f_{\mathrm{H\alpha}}$ and f_{CO}; and by complement the diffuse fractions $1 - f_{\mathrm{H\alpha}}$ and $1 - f_{\mathrm{CO}}$) are presented for our nine target galaxies in Appendix A.

3.5 Metallicity and reference time-scale

In this section, we quantify how metallicities of the target galaxies affect the input quantities and derived quantities of our analysis. While our method itself is not directly affected by changes in metallicity, accounting for metallicity variations allows us to calibrate the measured timeline more accurately and to calculate additional derived quantities as described below.

Firstly, the absolute calibration of the reference lifetimes of the young stellar phase (see Section 3.2) depends weakly on the

---

[11] Lower-mass clouds could potentially represent an accretion flow onto more massive clouds and therefore also participate at some level in the high mass formation process. However, these must represent a small gas reservoir, as we only filter out ∼ 15 per cent of the CO emission on average (see Table A1), and therefore do not constitute the main units for massive star formation.

---

metallicity as (Haydon et al. 2018):

$$t_{\mathrm{star,ref}} = (4.32 \pm 0.16\,\mathrm{Myr}) \times \left(\frac{Z}{Z_\odot}\right)^{-0.086 \pm 0.017}, \quad (2)$$

where we define

$$\frac{Z}{Z_\odot} \equiv \frac{(\mathrm{O/H})}{(\mathrm{O/H})_\odot}, \quad (3)$$

with $12 + \log(\mathrm{O/H})_\odot = 8.69$ (Asplund et al. 2009). We therefore scale the reference time-scale for each galaxy by the mean gas mass-weighted metallicity, based on the metallicity gradients measured in Pilyugin et al. (2014). This measurement is available for all galaxies in our sample, except NGC3627. For this galaxy, we therefore use the slope of the metallicity gradient as measured from MUSE observations (see Kreckel et al. 2019, which use the S-calibration method from Pilyugin & Grebel 2016). Because the calibration method is different than the one used in Pilyugin et al. (2014), we compare the average metallicities of the galaxies present in both samples and scale the absolute values in Kreckel et al. (2019) to match the average values in Pilyugin et al. (2014). For the three galaxies in common between the samples, this correction is smaller than 0.1 dex over the radial intervals considered in this work. For each galaxy, the resulting metallicities are shown as a function of galactocentric radius in Figure B3 and the adopted average metallicities are presented in Table 1. The corresponding reference time-scales calculated using equation 2 are listed in Table 3, and shown in Figure B2 as a function of galactocentric radius. Over the entire sample, the average metallicity ranges between $12 + \log(\mathrm{O/H}) = 8.39$ (for NGC5068) and $12 + \log(\mathrm{O/H}) = 8.84$ (for NGC5194), which translates into a narrow range of associated reference time-scales of $t_{\mathrm{star,ref}} = 4.19-4.53$ Myr. Within individual galaxies, the reference time-scale also varies by less than 10 per cent across the range of radii considered.

Secondly, the total molecular gas mass surface density scales directly with the value of the CO-to-H_2 conversion factor, α_{CO}. Therefore, the choice of the conversion factor affects a small subset of the quantities derived through our analysis, such as the molecular gas depletion time, the integrated star formation efficiency per star formation event, and the region-scale mass loading factor (see Kruijssen et al. 2018). For the conversion factor from CO(2-1) to total molecular gas mass, we adopt a fixed ratio CO(2-1)/CO(1-0) = 0.7 (e.g. Gratier et al. 2010; Leroy et al. 2011; T. Saito et al. in prep.) and use the α_{CO} factors provided by Sandstrom et al. (2013) when available (i.e. for NGC628, NGC3351, NGC3627, NGC4254 and NGC4321). For all other galaxies, we simply scale the conversion factor with metallicity as suggested by Bolatto et al. (2013):

$$\alpha_{\mathrm{CO}} = \left[2.9\,\mathrm{M_\odot\,(K\,km\,s^{-1}\,pc^2)^{-1}}\right] \times \exp\left(\frac{0.4Z_\odot}{Z}\right), \quad (4)$$

where α_{CO} is the conversion factor from CO(1-0) flux to total molecular gas mass, including the contribution of heavy elements. The adopted CO-to-H_2 conversion factors are listed in Table 3. When dividing the galaxies into several bins of galactocentric radius (see Section 5), we use the appropriate values of α_{CO} and t_{ref} corresponding to the mean metallicity in each bin (see Figure B2 for the profiles of α_{CO} and $t_{\mathrm{star,ref}}$ as a function of galactocentric radius). We note that these global values may deviate considerably on the scales of individual clouds (e.g. Schruba et al. 2017).

We note again that the absolute metallicity value has no direct influence on the primary parameters of the model (t_{gas}, t_{fb} and λ), which are based on the relative change of the gas-to-SFR flux ratio

compared to the galactic average, and not on the absolute values of the gas mass or SFR. The only way in which it affects the first two of these quantities is through the (slight) metallicity dependence of the reference time-scale in equation (2), which causes the reference time-scale to vary by less than 10 per cent across all galactic environments considered here (see Figure B2).

4 THE MOLECULAR CLOUD LIFECYCLE AVERAGED ACROSS NEARBY GALAXIES

We now apply the methodology described in Section 3 to the data presented in Section 2. We first show that our galaxy sample exhibits a universal de-correlation between molecular gas and star formation on the cloud scale, before translating this de-correlation into the evolutionary timeline of cloud evolution, star formation, and feedback. We conclude the section by giving brief summaries of other inferred quantities, each of which will be the subject of a more detailed analysis in follow-up work.

4.1 A universal de-correlation between gas and star formation on the cloud scale

We apply the analysis described in Sections 3.2 and 3.3, using Hα as a star formation tracer and CO as a gas tracer as discussed in Section 2. For each galaxy, we measure the gas-to-SFR flux ratio compared to the galactic average, focusing on gas peaks and SFR peaks, as a function of varying aperture sizes and then fit these measurements with a model describing how this observable changes as a function of the underlying evolutionary time-scales and region separation length.

Figure 2 shows the measured gas-to-SFR flux ratios as a function of the aperture size for each galaxy, together with the best-fitting model. All galaxies in our sample exhibit a pronounced de-correlation between gas emission and SFR emission, which becomes stronger as the aperture size decreases. This leads to two distinct branches, diverging from the galactic average. The cloud-scale de-correlation between gas and star formation was first observed in M33 by Schruba et al. (2010) and we find that it is a universal feature of the galaxies studied here. As discussed in Kruijssen et al. (2019), this de-correlation implies the rapid evolutionary cycling between molecular gas, star formation, and cloud destruction by stellar feedback. Fujimoto et al. (2019) builds on our empirical results to show that the de-correlation represents a fundamental test of feedback physics in galaxy simulations, as it probes the dispersive effect of stellar feedback on GMCs.

While we find a universal de-correlation between gas and star formation tracers on ~ 100 pc scales, Figure 2 also reveals quantitative variation between galaxies. This variation is caused by differences between the underlying evolutionary timelines. The mathematical expression of the model depends on three independent quantities: t_{CO}, t_{fb} and λ, from which we can also derive secondary quantities as described in Section 3.2. These three quantities are non-degenerate and affect the shape of the model in very different ways. The characteristic scale at which the branches diverge from the galactic average is set by λ. The ratio $t_{CO}/t_{H\alpha}$ governs the asymmetry between the branches, and the ratio t_{fb}/τ, as well as the finite size of the CO and Hα peaks, regulate the flattening of the branches at small aperture sizes (see Kruijssen et al. 2018 for more details). The best-fitting values of the above time-scale ratios are indicated in the bottom-right corner of each panel of Figure 2, with λ marked with an arrow along the x-axis in each panel. The figure

Galaxy	t_{CO} [Myr]	t_{fb} [Myr]	λ [pc]	v_{fb} [km s^{-1}]	ϵ_{sf} [per cent]
NGC0628	$24.0^{+3.6}_{-2.5}$	$3.2^{+0.6}_{-0.4}$	113^{+22}_{-14}	$8.5^{+1.0}_{-1.1}$	$6.1^{+3.7}_{-2.2}$
NGC3351	$20.6^{+3.4}_{-3.0}$	$2.5^{+0.8}_{-0.6}$	166^{+25}_{-16}	$14.8^{+4.3}_{-3.2}$	$5.2^{+5.0}_{-2.6}$
NGC3627	$18.9^{+3.4}_{-3.2}$	$2.8^{+0.8}_{-0.7}$	225^{+55}_{-34}	$20.9^{+5.9}_{-3.8}$	$10.2^{+7.7}_{-4.5}$
NGC4254	$20.9^{+3.9}_{-2.3}$	$4.8^{+1.1}_{-1.0}$	267^{+53}_{-44}	$14.7^{+2.6}_{-2.4}$	$4.2^{+2.2}_{-1.3}$
NGC4303	$16.9^{+4.6}_{-2.2}$	$4.0^{+1.8}_{-1.0}$	250^{+87}_{-44}	$17.4^{+4.0}_{-4.2}$	$4.3^{+3.7}_{-1.7}$
NGC4321	$19.1^{+2.3}_{-2.2}$	$3.3^{+0.7}_{-0.6}$	248^{+33}_{-26}	$19.6^{+3.8}_{-2.9}$	$7.1^{+5.2}_{-4.1}$
NGC4535	$26.4^{+4.7}_{-3.6}$	$3.9^{+1.2}_{-0.9}$	216^{+65}_{-37}	$15.4^{+2.6}_{-2.7}$	$3.8^{+2.9}_{-1.6}$
NGC5068	$9.6^{+2.9}_{-1.8}$	$1.0^{+0.4}_{-0.3}$	107^{+19}_{-11}	$15.6^{+5.8}_{-4.3}$	$4.3^{+3.7}_{-1.8}$
NGC5194	$30.5^{+9.2}_{-4.8}$	$4.8^{+2.1}_{-1.1}$	140^{+25}_{-17}	$7.9^{+1.9}_{-2.2}$	$4.0^{+3.5}_{-1.6}$

Table 4. Physical quantities describing the lifecycle of molecular cloud evolution, star formation, and feedback, obtained with the analysis described in Section 3. Each of these values represents the flux-weighted average for the corresponding galaxy. The uncertainties account for the finite sensitivity and resolution of the maps, as well as for the intrinsic stochasticity of the gas mass and SFR of the different regions.

clearly shows the impact of the above quantities on the shape of the tuning fork diagram describing the de-correlation between gas and star formation. First, galaxies with a small value of λ show a de-correlation at smaller aperture sizes (compare e.g. NGC628 and NGC4321). Secondly, galaxies with a small value of $t_{CO}/t_{H\alpha}$ have tuning fork diagrams with steeper top branches, reflecting a shorter cloud lifetime (compare e.g. NGC628 and NGC5068). Finally, galaxies with a small value of t_{fb}/τ have less flattened branches at small aperture sizes (compare e.g. NGC4254 and NGC5068).

Table 4 summarises the best-fitting values for t_{CO}, t_{fb} and λ, as well as the implied feedback outflow velocity (v_{fb}) and the integrated cloud-scale star formation efficiency (ϵ_{sf}). Together, these describe the molecular cloud lifecycle in the nine star-forming disc galaxies considered here. We now turn to a more detailed discussion of these results.

4.2 Measured molecular cloud lifetime

When applying the model to CO and Hα as tracers of the gas and young stellar phases, respectively, t_{CO} represents the duration of the molecular cloud lifetime during which CO emission is visible as local enhancement. The one-dimensional PDFs of the constrained t_{CO} are presented in Figure 3. The figure shows that t_{CO} is well constrained for all galaxies in our sample, with relative uncertainties ($\sigma_{t_{CO}}/t_{CO}$) in the range of 10–40 per cent.[12] We find that the derived molecular cloud lifetimes are relatively short and vary with

---

[12] We note that the uncertainties on t_{CO} in Figure 3 appear to be asymmetric and tend to increase with increasing t_{CO}. This is caused by two effects. First, the uncertainties are largely log-normal because we fundamentally measure relative time-scales, so that the ratio $\sigma_{t_{CO}}/t_{CO}$ is roughly constant. This manifests itself as an extended positive wing of the PDF when shown in linear space and generally broader PDFs for galaxies with longer GMC lifetimes. Secondly, the results of our analysis are more accurate when the time-scales of both phases (CO and Hα) are similar (Kruijssen et al. 2018). Because $t_{H\alpha}$ is always the shortest, this means that the smallest relative uncertainties are typically found in galaxies with the shortest GMC lifetimes.
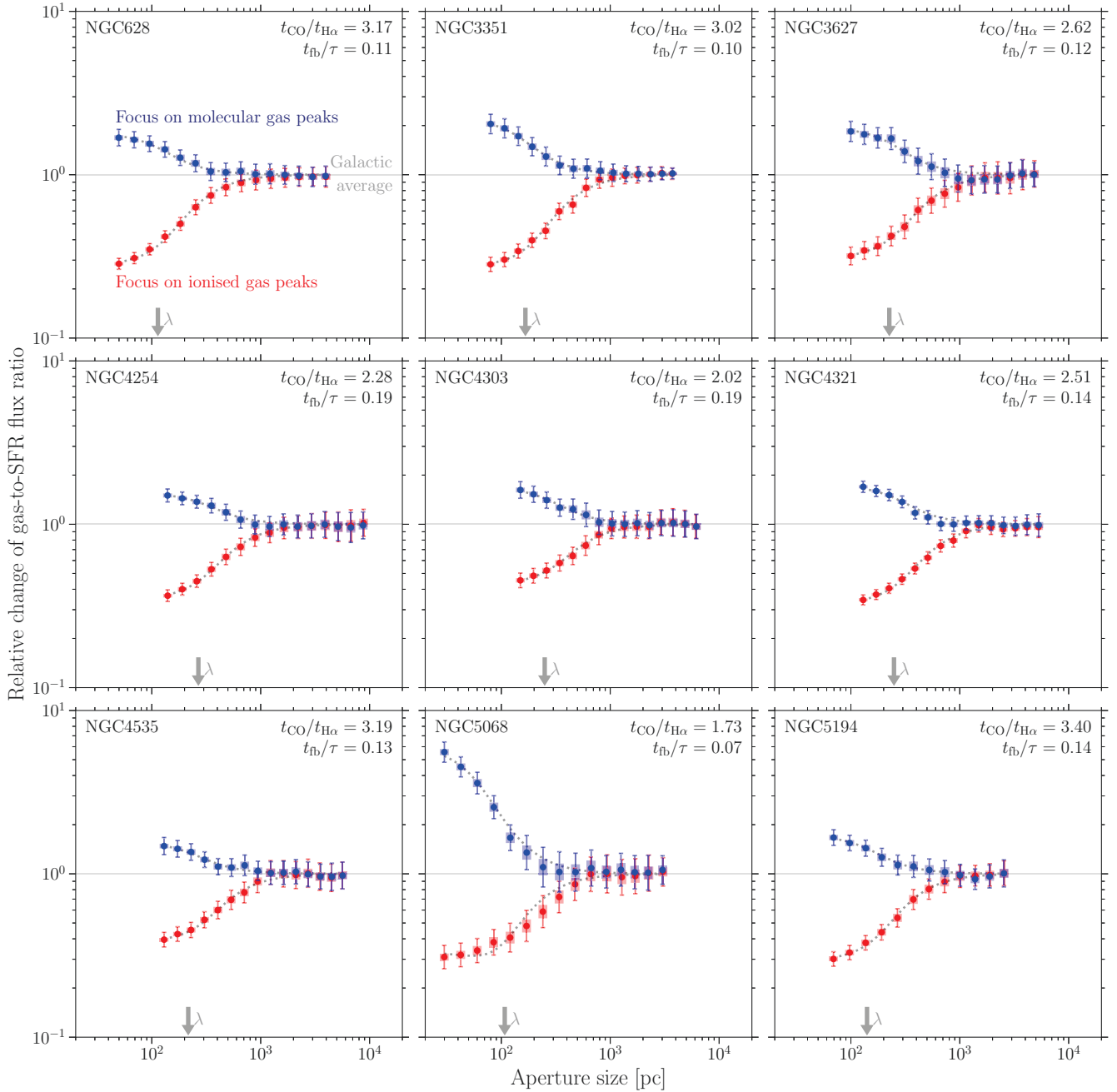
Figure 2. Relative change of the gas-to-SFR (CO-to-Hα) flux ratio compared to the galactic average as a function of aperture size, for apertures placed on CO emission peaks (blue) and Hα emission peaks (red). The error bars indicate the 1σ uncertainty on each individual data point, whereas the shaded areas indicate the effective 1σ uncertainty range that accounts for the covariance between the data points and should be used when visually assessing the quality of the fit. The horizontal solid line indicates the galactic average and the dotted line is the best-fitting model (Kruijssen et al. 2018), which allows us to constrain the GMC lifecycle. The arrows indicate the best-fitting values of the region separation length λ, which is always resolved given the minimum aperture sizes. The ratios $t_{CO}/t_{H\alpha}$ (controlling the asymmetry between the two branches) and t_{fb}/τ (controlling the flattening of the branches) are indicated in the bottom-right corner of each panel.

galactic environment: they range between 10 and 30 Myr across our galaxy sample. This range of values for the molecular cloud lifetime is consistent with those found in previous studies combining region classification with statistical incidence arguments (e.g. Engargiola et al. 2003; Kawamura et al. 2009; Meidt et al. 2015; Corbelli et al. 2017) and those based on the same statistical method

used here (Kruijssen et al. 2019; Hygate et al. 2019a). This is discussed in more detail in Section 6.2.

The above results have two important implications. First, they favour theories suggesting that molecular clouds are short-lived, transient objects that form, evolve, and disperse on a (cloud-scale or galactic) dynamical time (e.g. Elmegreen 2000; Dobbs et al. 2011; Grudić et al. 2018; Jeffreson & Kruijssen 2018; Semenov
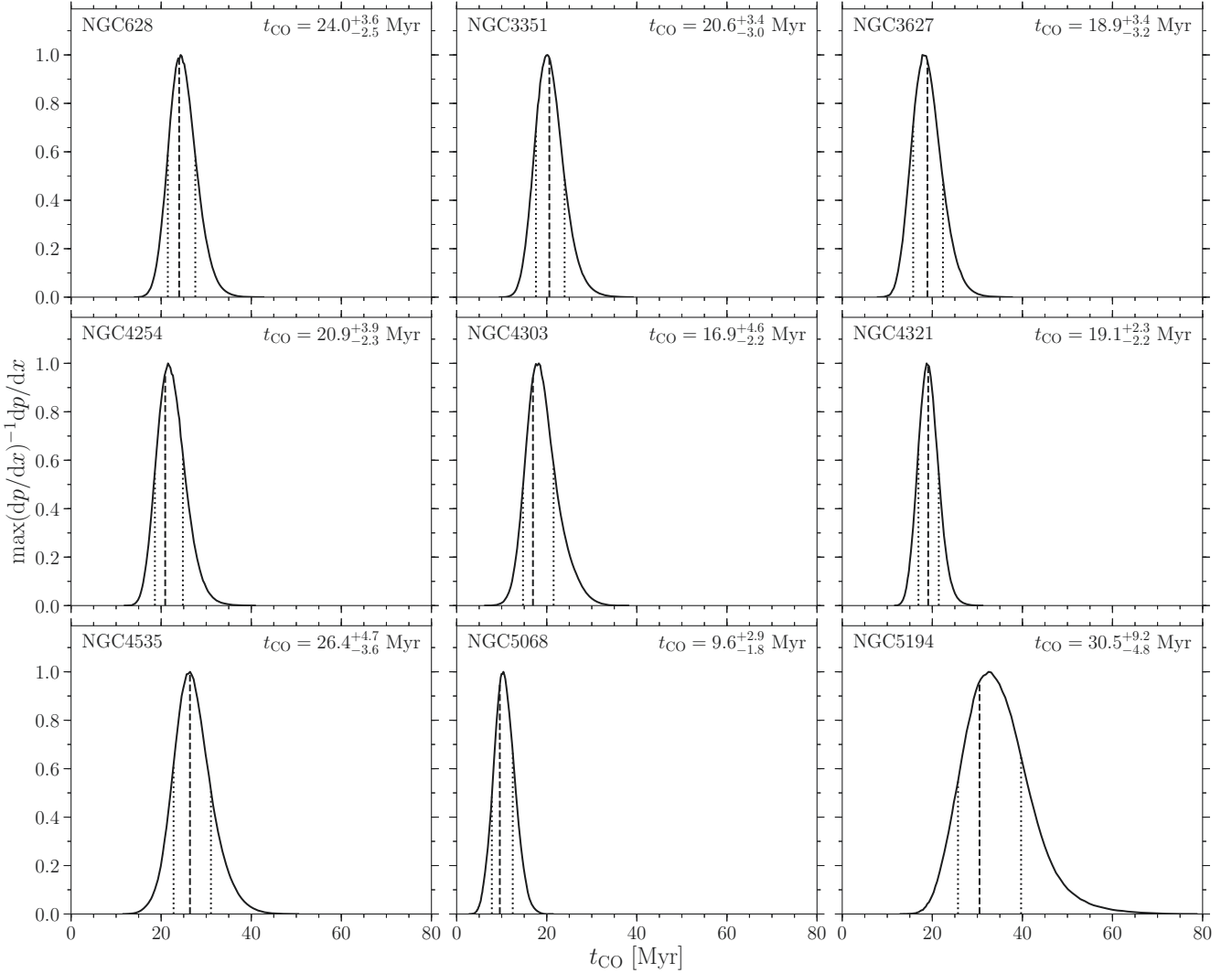
Figure 3. One-dimensional PDFs of t_{CO} for each galaxy. The vertical dashed lines indicate the best-fitting values and the dotted lines indicate the 1σ uncertainties, defined as the 32nd percentile of the part of the PDF below the best-fitting value, and the 68th percentile of the part of the PDF above the fitted value. The uncertainties account for the finite sensitivity and resolution of the maps, as well as for the intrinsic stochasticity of the gas mass and SFR of the different regions. The best-fitting values and their uncertainties are also indicated in the top-right corner of each panel.

et al. 2018). Secondly, the strong variation of the cloud lifetime between different galaxies suggests that cloud formation and collapse does not proceed on a universal time-scale but is plausibly governed by environment, such as galactic dynamics, either by directly setting the time-scale or indirectly, by changing the properties of the clouds (e.g. Leroy et al. 2017b). We will explore this hypothesis in Section 5. For the galaxy-wide quantities discussed in this section, the potential importance of environmental variations implies that the presented numbers are a flux-weighted average representation of the cloud lifecycle across the field of view covering each galaxy.

The full timelines from molecular clouds emitting in CO to young stellar populations emitting in Hα are shown in Figure 4, including the time for which CO and Hα coexist. This 'overlap' time shows when massive stars have started to emerge, but have not completely dispersed the parent molecular cloud yet. As such, it reflects the time over which stellar feedback acts on the cloud. We see that the evolutionary timelines all show evidence for a long 'inert' (or 'isolated' CO-bright) phase, during which the molecu-

lar clouds are brightly emitting in CO, but no signs of massive star formation have appeared yet in Hα. This is consistent with the results obtained using the same method for NGC300 (Kruijssen et al. 2019) and M33 (Hygate et al. 2019a), as well as with the results of GMC–HII region catalogue matching (Kreckel et al. 2018) and pixel statistics (Schinnerer et al. 2019), which all find large numbers of CO-bright clouds or pixels unassociated with Hα emission. While this does not exclude the (potentially prevalent) formation of low-mass stars during this inert phase, it seems inescapable to conclude that unembedded high-mass star formation arrives late during the cloud lifecycle, after 75–90 per cent of the cloud lifetime (corresponding to 9–26 Myr for the lifetimes measured here).[13]

The complete timelines shown in Figure 4 also demonstrate

---

[13] In principle, some clouds may condense and disperse more than once before massive star formation occurs. However, this does not seem very likely, because the measured cloud lifetimes are similar to a (cloud-scale or
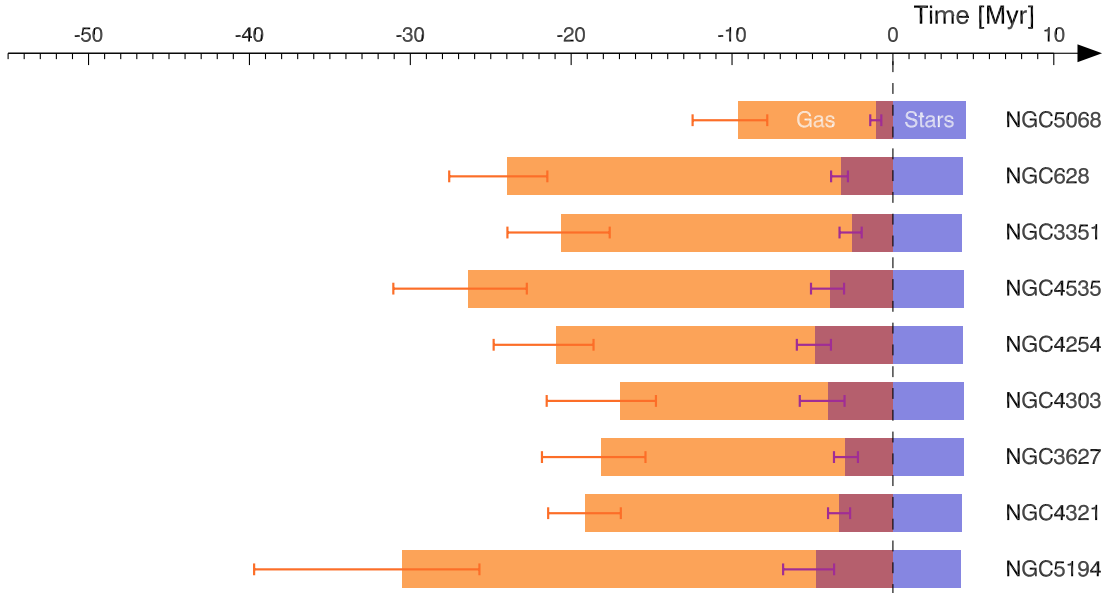
Figure 4. Evolutionary timeline of molecular clouds, star formation, and feedback for each of the nine galaxies. From top to bottom, the galaxies are ordered by increasing galaxy stellar mass. Orange indicates when only CO emission is visible (with duration $t_{\rm CO} - t_{\rm fb}$), purple indicates when only Hα emission is visible (with duration $t_{\rm star,ref} = t_{\rm H\alpha} - t_{\rm fb}$), and maroon indicates the 'overlap' phase, when the region emits both in CO and Hα (with duration $t_{\rm fb}$). The error bars on the left indicate the uncertainty on $t_{\rm CO}$, whereas the error bars in the middle indicate the uncertainty on $t_{\rm fb}$.

that unembedded massive star formation correlates strongly with cloud dispersal, as indicated by the short overlap times in Figure 4 (see Section 4.3.1 below), which constitute 9−18 per cent of the entire timeline (also see Figure 2). In principle, some massive stars may form earlier and remain embedded, so that they are not visible in Hα. We reiterate here that this would not affect our measurements of the cloud lifetimes, but only increase the duration of the overlap phase, because the reference time-scale $t_{\rm star,ref}$ to which our results are calibrated refers to the duration of the unembedded Hα-bright phase, without associated CO emission. We note that this holds under the assumption that new massive stars form as long as the region contains CO-bright molecular gas. In this context, the duration $t_{\rm star,ref}$ is not affected by extinction and the extent to which embedded massive star formation would extend the duration of the overlap phase can be determined by applying the same methodology to galaxies for which high-resolution 24μm maps are available. For NGC300, including embedded star formation would increase the duration of the overlap phase ($t_{\rm fb}/\tau = 0.1$) by only a few per cent (Kruijssen et al. 2019). Because NGC300 is a low-mass, half-solar metallicity galaxy, we might expect a stronger effect in more massive galaxies with higher cloud column densities. In particular, if massive stars are forming in a CO-dark environment, or if star formation stops before the CO gas has been cleared, $t_{\rm star,ref}$ might be affected by extinction. In a future paper, we plan to systematically address the impact of embedded massive star formation on the relative durations of the inert, isolated CO phase and the overlap phase (J. Kim et al. in prep.). Without further evidence, the strong correlation between massive star formation and the end of the CO-bright phase that we find here suggests a causal relation (see Section 4.3.1). This extends the result previously obtained for

galactic) dynamical time, which leaves little time for multiple cycles prior to massive star formation (also see footnote 5).

NGC300, i.e. that stellar feedback is a likely, if not dominant driver of molecular cloud dispersal (Kruijssen et al. 2019), to a wide variety of nearby star-forming galaxies.

4.3 Other derived quantities

In addition to the molecular cloud lifetime, our analysis allows us to constrain a wide variety of other physical quantities. These will be described in more detail in follow-up papers, but here we already summarise some of the key results.

4.3.1 Feedback time-scale

The duration of the feedback phase ($t_{\rm fb}$), during which molecular clouds and HII regions coexist, is relatively short, with $t_{\rm fb} = 1-5$ Myr, and also exhibits environmental variation between galaxies. For four of the galaxies in our sample (NGC628, NGC3351, NGC3627, and NGC5068), this feedback time is significantly shorter than the typical lower limit of 4 Myr at which the first supernovae explode (e.g. Leitherer et al. 2014), whereas for another two (NGC4321 and NGC4535) it is marginally shorter or consistent with 4 Myr. Under the assumption that the embedded phase of massive star formation is short (i.e. $\lesssim 1$ Myr, see the discussion in Sections 2.3 and 4.2, as well as e.g. Prescott et al. 2007; Hollyhead et al. 2015; Kruijssen et al. 2019), this implies that, in these environments, early feedback mechanisms such as winds, photoionisation or radiation pressure must be the dominant processes driving the destruction of molecular clouds.

The short feedback time-scales are not achieved by dynamical cloud dispersal without associated massive star formation. As explained in Section 3, our methodology fundamentally constrains the time spent in a CO-bright phase until associated Hα emission. If clouds would disperse dynamically without massive star forma-

tion, this 'starless' cycle would be added onto a future one during which massive stars do form. The fact that this integrated cloud life-time is found to be similar to a (cloud-scale or galactic) dynamical time-scale (see Section 5) means that there is very little time to go through multiple cycles of dynamical dispersal and (re-)formation. While we cannot formally reject such a scenario, the above time-scale argument makes it unlikely that clouds go through multiple lifecycles prior to experiencing massive star formation. We therefore propose that the close correlation between the appearance of massive stars and rapid cloud dispersal is physical in nature.

In addition, the short feedback time-scales provide evidence against multiple generations of massive star formation within GMCs taking place (and ceasing) prior to the (potentially extended) star formation episode that drives cloud dispersal (see footnote 5). The reason is that the feedback time-scale represents the total time spent by a region in a combined CO-bright and Hα-bright state. Because these overlap time-scales are of a similar duration as the time-scale over wich Hα is emitted by a massive star-forming region, $t_{\rm star,ref} \approx 4.3$ Myr, allowing even a single earlier, unembedded massive star formation episode would leave little or no time for the final massive star formation episode to coexist with a CO-bright cloud. The only alternative is that H II regions born during any earlier episodes of massive star formation would be ejected from the cloud on a short (~ 1 Myr) time-scale. This would require velocities of ~ 30 km s^{-1}, well in excess of the typical cloud-scale velocity dispersion observed in these galaxies (Sun et al. 2018). Therefore, the most plausible interpretation is that massive star formation is temporally clustered towards the end of the cloud lifecycle.

When comparing the measured feedback time-scales to the physical resolutions listed in Table 1, we see a suggestion of a weak trend of increasing $t_{\rm fb}$ towards coarser resolutions (also see the minimum aperture sizes $l_{\rm ap,min}$ in Table 3). We have combined our results with other studies performing the same analysis for NGC300 and M33 (Hygate et al. 2019a; Kruijssen et al. 2019), which all have resolutions of 50 pc or better, to determine whether this constitutes a systematic trend. We find that the feedback time-scale is uncorrelated with resolution for $l_{\rm ap,min} < 120$ pc, but a very weak trend starts to appear for $l_{\rm ap,min} > 120$ pc, in that no feedback time-scales $t_{\rm fb} < 3.3$ Myr are found for galaxies with observations at these resolutions. We therefore advise some caution in the interpretation of the feedback time-scales measured for NGC4254, NGC4303, NGC4321, and NGC4535. It is possible (though not necessarily likely) that these represent upper limits.

Using the same statistical method applied to Hα and CO(1-0) observations, a similarly short feedback time of 1.5 Myr has been measured in NGC300, for which Kruijssen et al. (2019) infer that molecular clouds are predominantly destroyed by photoionisation and stellar winds. Other studies, most of which rely on different methodological approaches, have also found evidence that GMCs are dispersed within a few Myr after the onset of massive star formation (e.g. Kawamura et al. 2009; Whitmore et al. 2014; Hollyhead et al. 2015; Corbelli et al. 2017; Grasha et al. 2019; Hannon et al. 2019; Hygate et al. 2019a). A detailed comparison between the measured feedback time-scales and theoretical expectations for different feedback mechanisms is investigated in more detail in a companion paper (M. Chevance et al. in prep.). The results of that work confirm the importance of 'early', pre-supernova feedback highlighted here.

4.3.2 Region separation length

In addition to the evolutionary timeline discussed so far, we also measure the separation length between independent regions (λ). This length scale is not an area-weighted mean separation length (which would be inflated by large empty space in galaxies, such as inter-arm regions), but instead describes the length scale in the immediate vicinity of a region over which a sufficiently large number of neighbouring regions is found to wash out the decorrelation seen in Figure 2. As such, it reflects the local number density of regions around emission peaks and does so in a way that combines both maps (CO and Hα in this case). Physically, λ defines the separation length between independent building blocks that each undergo the evolutionary lifecycles visualised in Figure 4 and together determine how galaxies form stars.

We find that the region separation length ranges between $\lambda = 100-300$ pc. Similar values have been found in NGC300 ($\lambda = 104^{+22}_{-18}$ pc, Kruijssen et al. 2019) and M33 ($\lambda = 164^{+37}_{-24}$ pc, Hygate et al. 2019a), but our measurements extend this range. Elmegreen et al. (2018) find a separation length of $\lambda_{\rm IR} = 410$ pc for infrared-bright (3.6$-$8 μm) clumps situated along 27 filaments in NGC4321. While this appears to be larger than the separation length measured here for the same galaxy ($\lambda = 248^{+33}_{-26}$ pc), we note that infrared emission tracing embedded stars only spans part of the timelines in Figure 4, such that the resulting separation length is increased by a factor of $\sqrt{\tau/t_{\rm IR}}$, with $t_{\rm IR}$ the visibility lifetime of the infrared emission. Therefore, these two values match each other to within the uncertainties on λ if $t_{\rm IR} = \tau(\lambda/\lambda_{\rm IR})^2$ falls in the range 6.2$-$12.1 Myr. This is not an unreasonable range, because it requires that the IR emission traces the overlap phase, part of the 'isolated young stellar' phase,[14] as well as a short embedded phase of (at most) a few Myr. Finally, we note that the other difference between Elmegreen et al. (2018) and this work is that we consider the entire galaxy, whereas Elmegreen et al. (2018) focus on the separation along dominant filamentary structures. Excluding peaks that do not closely follow these structures likely results in a longer measured separation scale. A similarly larger separation scale between individual CO peaks (~ 400pc) is indeed observed by Henshaw et al. (2019) along the southern spiral arm of NGC4321.

When comparing the measured separation lengths to the physical resolutions listed in Table 1, we typically find larger separation lengths at coarser resolution (also see the discussion in Section 4.3.1). We have combined our results with other studies performing the same analysis for NGC300, M33, and the LMC (Hygate et al. 2019a; Kruijssen et al. 2019; Ward et al. 2019, with the latter measuring the separation length for H I clouds and H II regions), which all have resolutions of 50 pc or better, to determine whether this constitutes a systematic trend. We find that the region separation length mirrors the behaviour of the feedback time-scale. It is uncorrelated with resolution for $l_{\rm ap,min} < 120$ pc, but a trend starts to appear for $l_{\rm ap,min} > 120$ pc. We therefore advise some caution in the interpretation of the separation lengths measured for NGC4254, NGC4303, NGC4321, and NGC4535. It is possible (though not necessarily likely) that these represent upper limits.

It remains to be determined which physical mechanisms set the region separation length across our galaxy sample. For NGC300, Kruijssen et al. (2019) compare the region separation

---

14 Based on observations of NGC300, the Large Magellanic Cloud, and M33, 24 μm emission and Hα emission seem to largely trace the same part of the timeline (J. Kim et al. in prep.), so we expect IR emission to also partly trace the isolated Hα phase.

length to the gas disc scale height and the Toomre (1964) instability length and find that λ matches the gas disc scale height across the full extent of the star-forming disc. A future paper will present this comparison for the nine galaxies considered here, and will investigate whether this correlation applies across the nearby galaxy population (M. Chevance et al. in prep.).

4.3.3   Feedback velocity

Having measured the time-scale over which stellar feedback disperses molecular clouds, combining this with the typical spatial extent of the clouds results in a characteristic velocity scale. This 'feedback outflow velocity' is defined as

$$v_{\mathrm{fb}} = \frac{r_{\mathrm{CO}}}{t_{\mathrm{fb}}}, \qquad (5)$$

where r_{CO} is the mean radius of the CO emission peaks determined with HEISENBERG as the standard deviation of a two-dimensional Gaussian (see eq. 95 in Kruijssen et al. 2018 and the discussion in Appendix A1 of Hygate et al. 2019b; we show $r_{\mathrm{GMC}} = 1.91 r_{\mathrm{CO}}$ in Figure B4).[15] Depending on the nature of molecular cloud dispersal, e.g. whether it is kinetic or takes place by a phase transition, this velocity may represent the speed of the kinetic removal of molecular gas or the speed of the phase transition front. We obtain values in the range $v_{\mathrm{fb}} = 8-21$ km s^{-1}, with a mean of $v_{\mathrm{fb}} \approx 15$ km s^{-1}. These velocities fall within the range of typical expansion velocities found in nearby HII regions in the Milky Way, LMC, NGC300, and M33 (6–30 km s^{-1}, see e.g. Bertoldi & McKee 1990; Murray & Rahman 2010; Hygate et al. 2019a; Kruijssen et al. 2019; McLeod et al. 2019b,a) and in numerical simulations of expanding HII regions (e.g. Dale et al. 2014; Kim et al. 2018). These predictions can be tested independently by measuring the ionised gas kinematics through (integral-field) spectroscopy (for instance with MUSE) for these galaxies.

4.3.4   Star formation efficiency

On galactic scales, the star formation relation between the gas mass (M_{gas}) and the SFR implies a gas depletion time $t_{\mathrm{dep}} \equiv M_{\mathrm{gas}}/\mathrm{SFR}$, which is observed to be $t_{\mathrm{dep}} \approx 2$ Gyr in nearby star-forming galaxies (Bigiel et al. 2008; Bigiel et al. 2011; Leroy et al. 2008, 2013; Blanc et al. 2009; Schruba et al. 2011) and represents the time necessary to convert the entire reservoir of molecular gas into stars at the current SFR. Because the SFR can be expressed as $\mathrm{SFR} = \epsilon_{\mathrm{sf}} M_{\mathrm{gas}}/t_{\mathrm{CO}}$, where t_{CO} is the cloud lifetime and ϵ_{sf} is the mean star formation efficiency per unit cloud lifetime, the gas depletion time is also given by $t_{\mathrm{dep}} = t_{\mathrm{CO}}/\epsilon_{\mathrm{sf}}$. This expression highlights that, at fixed depletion time, there exists a degeneracy between the star formation efficiency and the cloud lifetime. The long depletion time measured on galactic scales (i.e. $t_{\mathrm{dep}} \approx 2$ Gyr being much larger than a dynamical time, see e.g. Zuckerman & Palmer 1974) can either be a result of a small cloud-scale star formation efficiency or of a long cloud lifetime. By directly measuring the characteristic time-scale on which individual clouds within galaxies live and form stars, t_{CO}, we break this degeneracy. As noted

above, our results qualitatively indicate that only a small fraction of the gas mass is converted into stars, with clouds being short-lived and disrupted by stellar feedback before they reach a high star formation efficiency. This is consistent with theoretical and numerical predictions (e.g. Semenov et al. 2017; Grudić et al. 2018; Kim et al. 2018).

Quantitatively, we calculate the integrated star formation efficiency per star formation event as (Kruijssen et al. 2018, eq. 143):

$$\epsilon_{\mathrm{sf}} = \frac{t_{\mathrm{CO}} \Sigma_{\mathrm{SFR}}}{\Sigma_{\mathrm{gas}}}, \qquad (6)$$

where Σ_{SFR} is the SFR surface density and Σ_{gas} the molecular gas surface density across the field of view of each galaxy where we carry out our analysis. We calculate Σ_{SFR} as described in Section 2.4 and we obtain Σ_{gas} from the filtered CO map, using the conversion factor X_{gas} from Table 3. For Σ_{gas}, we thus take only the compact CO emission into account, because this is the emission for which t_{CO} describes the lifetime. This choice assumes that most of the diffuse CO emission[16] originates from truly diffuse molecular gas or from small molecular clouds that do not participate in the formation of massive stars generating Hα emission. With these assumptions in mind, we measure small star formation efficiencies per star formation event, ranging between $\epsilon_{\mathrm{sf}} = 4-10$ per cent. The combination of a short t_{CO} and low ϵ_{sf} indicates that star formation is fast and inefficient, for all galaxies in our sample.

In closing, we note the difference in definition between the integrated star formation efficiency per star formation event from equation (6) to the star formation efficiency per free-fall time, which is given by $\epsilon_{\mathrm{ff}} = t_{\mathrm{ff}} \Sigma_{\mathrm{SFR}}/\Sigma_{\mathrm{gas}}$ (where t_{ff} is the free-fall time). Utomo et al. (2018) measure ϵ_{ff} for all nine galaxies in our sample. Because we find cloud lifetimes of 1–3 free-fall times, $\epsilon_{\mathrm{sf}} \equiv \epsilon_{\mathrm{ff}} t_{\mathrm{CO}}/t_{\mathrm{ff}}$ is higher than ϵ_{ff} by a factor of a few. Another difference is that we measure the star formation efficiency of compact clouds, i.e. after removing diffuse CO emission from the maps, whereas Utomo et al. (2018) measure ϵ_{ff} from the unfiltered CO maps, resulting in a lower efficiency, appropriate for the entire molecular gas reservoir rather than for the clouds considered here. This also contributes to $\epsilon_{\mathrm{sf}} > \epsilon_{\mathrm{ff}}$.

5   VARIATION OF THE MOLECULAR CLOUD LIFETIME AS A FUNCTION OF GALACTIC ENVIRONMENT

We now discuss how the cloud lifetime depends on the galactic environment, by applying our analysis to bins in galactocentric radius. We then compare to analytical models for cloud evolution to determine whether the cloud lifetime is set by internal or external processes. We also discuss the influence of galactic morphological features on the measured cloud lifetimes. In conclusion, we find that both internal and external processes can set the cloud lifetime, and propose a rough separation between both regimes in terms of a critical value of the large-scale gas surface density (i.e. the area-average across radial rings or annuli within the galaxies).

---

[15]   While some of the CO emission peaks may represent unresolved groups of molecular clouds, the measured feedback velocity is quite robust against such blending effects, because the CO peak radius and the feedback time-scale exhibit similar dependences on blending (see fig. 3 of Kruijssen et al. 2019). As a result, the uncertainties increase towards coarser resolution, but the feedback velocity itself remains largely consistent with its true value.

[16]   This is ~ 25 per cent on average, see Table A1 for all measurements of the diffuse CO and Hα emission fractions across our galaxy sample.

5.1 Radial profiles of the molecular cloud lifetime

After having identified a variation of the integrated cloud lifetime between galaxies in Section 4.2, we investigate potential variations of $t_{\rm CO}$ within galaxies to test the hypothesis that the cloud evolution process depends on galactic environment, and determine which mechanisms are playing a role in this process. For each galaxy in our sample, we apply our analysis to successive radial bins around the galactic centre (see Figure B1 for images of the galaxies showing how the radial bins are defined). To do this, we divide each galaxy into non-overlapping radial bins of a minimum width of 1 kpc. This condition is set to satisfy the requirement of having a random two-dimensional distribution on a scale $\sim \lambda$ (typically a few 100 pc, see Table 4) for the application of the method. In addition, we require that each bin contains a minimum of 50 peaks identified in our full-galaxy runs for each tracer, to ensure sufficient statistics to constrain the derived quantities to sufficiently high precision (Kruijssen et al. 2018). If this condition is not satisfied for bins that are 1 kpc in width, we increase their width (and therefore decrease the total number of bins) in order to satisfy this condition.

As the peak identification is normally done by stepping down in flux density relative to the brightest peak in the image (which is different in each radial bin, possibly causing the identified peaks to be different than in the full maps; see Section 3), we supply the peaks identified across the full maps as input for the analysis in each radial bin. As input maps, we use the filtered maps, from which diffuse emission has been removed through the iterative filtering process applied to the full field of view (as described in Section 3.4). This approach is validated a posteriori by the fact that λ (which sets the filtering scale) is approximately constant between each bin for a given galaxy. The resulting $t_{\rm CO}$ profiles as a function of the galactocentric radius for each galaxy are presented in Figure 5 and in Table B1.

We find that, given the uncertainties, the cloud lifetime is often consistent with being constant within galaxies, although some radial variations can be identified. For example, $t_{\rm CO}$ is relatively constant in some galaxies (e.g. NGC628, NGC4303 and NGC4321), but in others it peaks at a certain radius (e.g. NGC3627, NGC4254 and NGC5194), or decreases outwards (e.g. NGC3351, NGC4535 and NGC5068). To understand the origin of these variations, we will now compare the measured cloud lifetimes with analytical predictions for cloud-scale dynamical time-scales and galactic dynamical time-scales.

5.2 Comparison with analytical models

To understand the origin of the environmental variation of $t_{\rm CO}$, we compare our observations with analytical predictions. If molecular clouds are gravitationally bound and globally collapsing, their evolution is governed by the gravitational free-fall time $t_{\rm ff}$. We define the cloud free-fall time as:

$$t_{\rm ff} = \sqrt{\frac{\pi^2 r_{\rm GMC}^3}{10 G M_{\rm GMC}}}, \qquad (7)$$

for spherical clouds of radius $r_{\rm GMC}$ and molecular gas mass $M_{\rm GMC}$, where G is the gravitational constant. The GMC radius and mass are derived using the output from Heisenberg by defining $r_{\rm GMC} \equiv 1.91 r_{\rm CO}$ (Kruijssen et al. 2019) and $M_{\rm GMC} \equiv \mathcal{E}_{\rm gas} \Sigma_{\rm H_2} \pi (\lambda/2)^2$, where $\mathcal{E}_{\rm gas}$ is the surface density contrast on a size scale λ relative to the surface density measured across the field of view, $\Sigma_{\rm H_2}$ (Kruijssen et al. 2018). The choice to take these from the output of Heisenberg is mainly self-consistency – this way,

the masses and radii are obtained for the units that are inferred to undergo the evolutionary lifecycles characterised in this work. By contrast, using a cloud catalogue would rely on subjective classification. It would also be more strongly affected by the finite resolution of the observations. For example, applying the cloud characterisation algorithm CPROPS (Rosolowsky & Leroy 2006) to the CO maps leads in some cases to the identification of GMC complexes of several 100 pc in size (larger than λ), rather than individual GMCs. This is remedied in Heisenberg by using a sub-resolution model to infer GMC sizes from the surface brightness contrast of a subsample of emission peaks against the large-scale background. By definition, these emission peaks are then separated by the separation length of independent regions (see eqs. 94 and 95 of Kruijssen et al. 2018), such that their radii cannot exceed λ. In this context, $r_{\rm GMC}$ and $M_{\rm GMC}$ represent the CO flux-weighted average for each radial bin.

We show the median profile of $t_{\rm ff}$ as a function of the galactocentric radius in Figure 5. For all the galaxies in our sample, $t_{\rm ff}$ is relatively constant within galaxies, exhibiting variations of less than a factor of two. In general, $t_{\rm ff}$ is close to or shorter than the measured molecular cloud lifetime, both for the global measurements and in individual bins, which is expected given that it represents the extreme case of free-fall collapse. Quantitatively, we find that clouds live for $1-3$ free-fall times. However, in some cases $t_{\rm CO}$ appears shorter than $t_{\rm ff}$ by more than the uncertainty. This happens in 6 out of 39 radial bins and could potentially be caused by a biased measurement of $t_{\rm CO}$ due to the effect of galaxy morphology (see the discussion below in Section 5.3), or by the fact that the clouds are not resolved, resulting in an underestimated value of $t_{\rm ff}$ due to beam dilution. However, at least some of these six bins with short-lived clouds should simply result from the uncertainties. We find 12 bins for which $t_{\rm CO} \approx t_{\rm ff}$ to within the uncertainties, implying that for a normal distribution we expect three bins where $t_{\rm CO}$ falls significantly below $t_{\rm ff}$.

We also compare the measured cloud lifetime to the GMC crossing time, which is defined as:

$$t_{\rm cr} = \frac{r_{\rm GMC}}{\sigma_{\rm vel}}, \qquad (8)$$

where $\sigma_{\rm vel}$ is the one-dimensional cloud velocity dispersion. Because Heisenberg does not provide kinematic information, we use the individual cloud velocity dispersions determined by E. Rosolowsky et al. (in prep.) using CPROPS (Rosolowsky & Leroy 2006). Before inserting $r_{\rm GMC}$ and $\sigma_{\rm vel}$ into equation (8), we calculate the CO flux-weighted average for each radial bin. For a large fraction of the galaxies, $t_{\rm cr}$ is similar to the free-fall time and the measured molecular cloud lifetimes, both globally and in individual bins.

Despite the rough similarity between $t_{\rm CO}$ and $t_{\rm ff}$, in many cases (e.g. NGC628, NGC3627, NGC5194) the measured molecular cloud lifetimes cannot be simply explained by the local cloud dynamical time, as visible in Figure 5. We pursue the alternative hypothesis that molecular cloud lifetimes are environmentally dependent and can be affected by galactic dynamics, which has been shown to hold for other cloud properties, such as surface density, velocity dispersion, and boundedness (e.g. Leroy et al. 2017b; Sun et al. 2018; Schruba et al. 2019). We therefore compare our measurements with the predictions of the analytical theory for GMC lifetimes from Jefferson & Kruijssen (2018). Within this theory, the cloud lifetime is set by the large-scale dynamics of the ISM and calculated as the harmonic average of characteristic time-scales associated with the gravitational collapse of the ISM ($\tau_{\rm ff,g}$) counter-
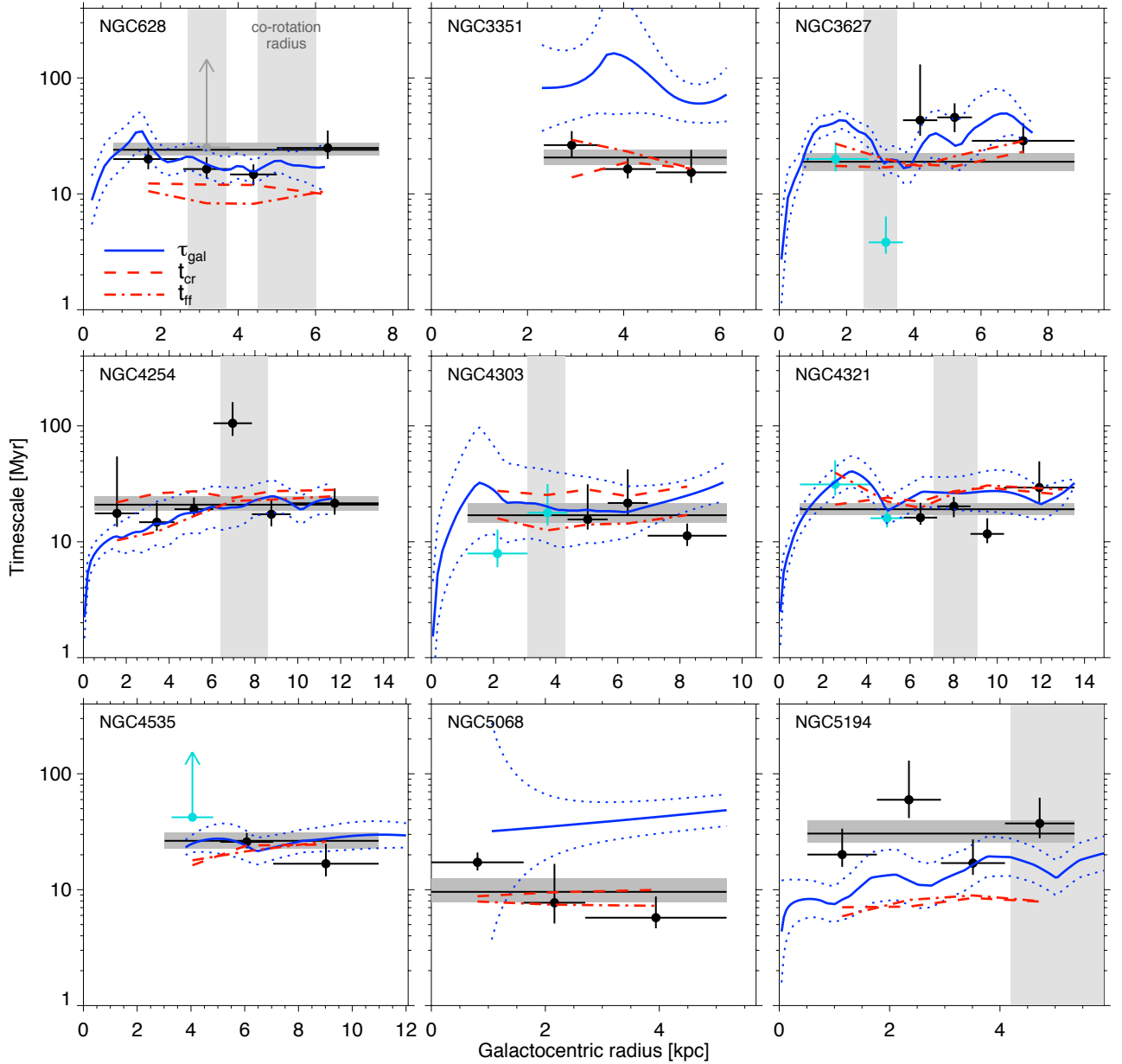
Figure 5. Measured molecular cloud lifetime (t_{CO}) as a function of the galactocentric radius for each galaxy (data points with error bars) and for the full galaxy (horizontal black lines with shaded area representing the 1σ range of uncertainties). For each data point, the horizontal bar spans the range of radii within which t_{CO} is measured and the vertical bar represents the 1σ uncertainties. We note that the uncertainties on t_{CO} for the individual bins are generally larger than the uncertainties for the full galaxies. This results from a larger degree of stochasticity due to a lower number of regions per bin, while the uncertainties on the full galaxies mostly reflect observational uncertainties on the (well-constrained) mean value. The shaded data point in NGC628 represents the value of t_{CO} measured in the second radial bin if the 'headlight' cloud (which vastly dominates the CO emission from the cloud population in that radial bin, see the text and Herrera et al. 2019) is not masked. The light blue data points indicate the bins coinciding with the bar or residing at the tip of the bar for the barred galaxies NGC3627, NGC4303, NGC4321, and NGC4535. The lines indicate the predictions from simple theoretical prescriptions. Red dash-dotted and dashed lines indicate the profiles of the cloud free-fall time and the cloud crossing time, respectively. Blue solid lines represent the cloud lifetime due to various galactic dynamical processes as predicted by the analytical model of Jeffreson & Kruijssen (2018), with dotted lines indicating the 1σ uncertainties on the prediction. The positions of the co-rotation radii (see text and Table 5) are indicated by vertical shaded areas. All measurements of the cloud lifetime shown in this figure are listed in Table B1.

acted by galactic shear (τ_β), cloud-cloud collisions (τ_{cc}), density wave perturbations (τ_{Ω_P}), and epicyclic perturbations (τ_κ). As galactic shear is a dynamically dispersive process, while the other mechanisms are dynamically compressive, it competes with gravitational collapse and the resulting lifetime can be written as

$$\tau_{gal} = |\tau_{ff,g}^{-1} - \tau_\beta^{-1} + \tau_{cc}^{-1} + \tau_{\Omega_P}^{-1} + \tau_\kappa^{-1}|^{-1}. \tag{9}$$

We show the predictions of this model with blue lines in Figure 5, including the uncertainties on the predictions obtained by propagating the uncertainties on the input quantities (see below). We note that in the inner part of NGC3351, the τ_β term becomes as large as all other mechanisms combined, resulting in an extremely large τ_{gal} with a large downward uncertainty. This most likely reflects the morphology of NGC3351, with a strong bar in the center, and a prominent gas ring between $\sim$ 2 and 5 kpc.

All of the time-scales taken into account in τ_{gal} depend on observable parameters. Specifically, these are the angular velocity Ω (all time-scales depend inversely on Ω), the Toomre Q parameter, the surface densities and velocity dispersions of gas (Σ_g and σ_g, respectively) and stars (Σ_s and σ_s, respectively), which are combined into the single quantity $\phi_P = 1 + (\Sigma_s \sigma_g / \Sigma_g \sigma_s)$, the shear $\beta \equiv d \ln \Omega / d \ln R + 1$, the number of spiral arms m and their pattern speed Ω_P. Different (regions of the) galaxies are therefore likely to cover different areas of the ($\beta, Q, \Omega, \phi_P, m, \Omega_P$) parameter space, where cloud evolution is predicted to be governed by different processes, resulting in different values of the cloud lifetime (Jeffreson & Kruijssen 2018). We describe how these quantities are derived in Appendix B. Figure 5 shows that in most galaxies (except for NGC3351 and NGC5068) there exists a broad agreement between the measured molecular cloud lifetimes and the analytical predictions. However, we also note discrepancies in some individual radial bins, which we explore below.

5.3 Influence of galaxy morphology

5.3.1 Co-rotation radius

At the co-rotation radius, the velocity of the material in the disc equals the pattern speed of the spiral structure. Molecular clouds located at the co-rotation radius are therefore likely to permanently reside in a deep potential well provided by the spiral arm, which potentially facilitates sustained gas inflow and extends cloud lifetimes (i.e. the duration of the CO-visible phase). Table 5 summarises the available measurements of co-rotation radii for the galaxies in our sample, and these are indicated as vertical grey-shaded bands in Figure 5. For NGC3351, NGC4535 and NGC5068, either the co-rotation radius falls outside of the range of radii considered here, or no clear pattern speed was available from previous measurements.

Some influence of co-rotation on the molecular cloud lifetime is suggested in several galaxies in Figure 5, with longer cloud lifetimes compared to the galactic average in the bins located at the co-rotation radius. This is most prominent in NGC4254, NGC3627 and NGC628 (lower limit on the cloud lifetime shown by the grey data point), but also somewhat in NGC5194 in the sense that the last bin falls above the median of all bins. One of the most striking examples is found in NGC628, with the presence of a very bright cloud (referred to as the 'headlight' cloud in Herrera et al. 2019), located at the intersection of a spiral arm and the co-rotation radius at 3.2 kpc. We have masked this particular cloud in our analysis in Section 4. The reason is that this cloud is three times brighter in CO(2-1) than any other cloud in the galaxy and it would thus dominate our flux-weighted cloud-lifetime, therefore strongly bias-

Galaxy	R_{CR} [kpc]	Reference
NGC628	2.7−3.7	1
	4.5−6.0	2
NGC3627	2.5−3.5	3
NGC4254	6.4−8.6	4,5,6
NGC4303	3.1−4.3	7
NGC4321	7.1−9.1	8,9
NGC5194	4.2−6.5	8,10,11

Table 5. Position of co-rotation radii for the galaxies of our sample. References: (1) Herrera et al. (2019), (2) Cepa & Beckman (1990), (3) Rand & Wallin (2004), (4) Elmegreen et al. (1992), (5) Gonzalez & Graham (1996), (6) Kranz et al. (2001), (7) Schinnerer et al. (2002), (8) Elmegreen et al. (1989), (9) Garcia-Burillo et al. (1998), (10) Scheepmaker et al. (2009), (11) Querejeta et al. (2016). The range of values given takes into account 15 per cent uncertainties for single references, or the range of values found in the literature when several references exist. Where necessary, we scale R_{CR} to be consistent with the distances tabulated in Table 3.

ing the results towards this particular gas-dominated environment and increasing the apparent cloud lifetime, especially in the second radial bin. If left unmasked, the average cloud lifetime for the full galaxy increases slightly from $t_{CO} = 24.0^{+3.6}_{-2.5}$ Myr to $t_{CO} = 25.1^{+5.0}_{-2.8}$ Myr and becomes unconstrained in the bin including the 'headlight' cloud, with a lower limit of 25.1 Myr (in the top-left panel of Figure 5, compare the grey symbol to the black symbol at the same galactocentric radius). We have verified that other galaxies are not dominated by a single cloud, meaning that the headlight cloud in NGC628 represents an exception due to its extreme mass. In a less extreme way, the low value of t_{CO} measured at the co-rotation radius in NGC4321 likely results from a similar effect, but at a later stage of the star formation cycle. Some of the brightest Hα peaks (including the brightest peak of our map) are located at this co-rotation radius, indicating an accumulation of recent massive star formation events. This violates our requirement of an approximately constant SFR and biases the measured t_{CO} towards a low value.

5.3.2 Influence of the bar

Bars are known to drive large local variations of the molecular gas depletion time due to gas transport and bursty star formation. Specifically, they generate accumulations of material at the bar ends, where massive clouds and bursty star formation are commonly observed (e.g. Beuther et al. 2017), they induce strong radial transport and suppress star formation (e.g. Khoperskov et al. 2018; Sormani & Barnes 2019), and they drive nuclear starbursts (e.g. Peeples & Martini 2006). A small number of bins in Figure 5 exhibit very high or very low values of the molecular cloud lifetime (e.g. the second bin of NGC3627 or the inner bin of NGC4535), which is plausibly caused by the presence of a bar in these galaxies. In Figure 5, we highlight in light blue the data points corresponding to the bins including the bar or the end of the bar for the four barred galaxies in our sample (these are NGC3627, NGC4303, NGC4321, and NGC4535, but excludes NGC3351, for which we do not cover the bar; see also Figure B1). For NGC3627, NGC4303 and NGC4321, the inner bin covers the bar of the galaxy, whereas the second bin covers the tip of the bar. For NGC4321 we note an elevation (by $\sim$ 60 per cent) of the molecular cloud lifetime in the inner bin compared to the galactic average. This is caused by a lack of Hα emission in the bar noted by Schinnerer et al. (2019).

We do not measure a significant elevation of t_{CO} in NGC3627 and NGC4303, where the star formation in the bar is not as strongly suppressed.

For the bins at the end of the bar (i.e. the second bins of NGC3627, NGC4303, and NGC4321, as well as the inner bin of NGC4535), we expect highly bursty and localised star formation. This can lead to strongly enhanced or deficient star formation, depending on the moment of observation, and would violate one of the fundamental assumptions of our methodology, which is that the star formation history over the recent time interval τ must have been relatively constant (Kruijssen et al. 2018). As a consequence, it is not surprising that the data point at the tip of the bar in NGC3627 seems to be an outlier in Figure 5. In NGC3627, Beuther et al. (2017) suggest that the interaction between the end of the bar and the spiral arms might induce strong star formation events. The particularly short cloud lifetime ($t_{CO} = 3.8^{+2.6}_{-0.8}$ Myr) measured in the second bin of NGC3627 (as well as a short $t_{fb} = 0.8^{+0.7}_{-0.4}$ Myr) is due to the fact that two very bright regions both in Hα and in CO dominate this bin. This likely traces a recent burst of star formation and biases the average duration of the different phases towards low values. By contrast, the long t_{CO} (lower limit of 42.1 Myr) measured in the innermost bin of NGC4535, also covering the end of the bar, indicates a low SFR over the recent time interval τ. Interpreted in the context of bursty star formation, this reflects the same physical mechanism as in NGC3627, but observed at a different moment in time. While a starburst has recently taken place at the tip of the bar in NGC3627, gas is currently accumulating at the tip of the bar in NGC4535. Both of these extremes bias the measured cloud lifetimes.

5.4 Galactic dynamics versus internal dynamics

We now investigate the variation of the measured molecular cloud lifetimes in regions that are not affected by galaxy morphology as described in Section 5.3 (i.e. the black data points in Figure 5). Our observations show good agreement with the analytical predictions from Jefferson & Kruijssen (2018) in some of the radial bins, but diverge from these predictions in others, especially in the outskirts of galaxies (e.g. NGC4303 and NGC4535) and in galaxies with low global gas surface densities (e.g. NGC3351 and NGC5068), where t_{CO} is in better agreement with the cloud free-fall time or the cloud crossing time. We have looked for environmental factors that may govern this dichotomy between local or global dynamics correlating with the cloud lifetime, and find that the kpc-scale galactic gas surface density might play a key role. By dividing the sample of measurements between 'low' and 'high' regimes of the area-weighted mean molecular gas surface density in each radial bin (see Figure C1), we find that the transition between cloud lifetimes being governed by galactic dynamics versus cloud lifetimes being set by cloud internal dynamics seems to occur at a molecular gas surface density averaged across the galactocentric radial rings (i.e. measured on $\gtrsim$ kpc scales) of $\Sigma_{H_2,ring} \approx 8\,M_\odot\,pc^{-2}$ (see Appendix C for details), with galactic dynamics dominating at high

surface densities and internal dynamics dominating at low densities.[17]

The different dynamical regimes are illustrated more quantitatively in Figure 6, where we compare t_{CO} with both the analytical prediction based on galactic dynamical processes from Jefferson & Kruijssen (2018) and the internal dynamical time-scales of the clouds, i.e. the cloud free-fall time and the cloud crossing time. In this comparison, we distinguish between the bins where the kpc-scale molecular gas surface density is low ($\Sigma_{H_2,ring} < 8\,M_\odot\,pc^{-2}$, left panel) or high ($\Sigma_{H_2,ring} > 8\,M_\odot\,pc^{-2}$, right panel). At low kpc-scale molecular gas surface densities, there is a better agreement between t_{CO} and the internal dynamical time-scales (t_{cr} and t_{ff}, showing median offsets of 0.09 and 0.06 dex, with standard deviations of 0.25 and 0.20 dex, respectively) than between t_{CO} and τ_{gal} (median offset of 0.28 dex, with a standard deviation of 0.34 dex). Conversely, at high gas surface densities, there is good agreement between t_{CO} and τ_{gal} (median offset of 0.03 dex, with a standard deviation of 0.27 dex), whereas the comparison of t_{CO} and the internal dynamical time-scales shows a systematic offset, albeit with a similar spread (for t_{cr} and t_{ff}, the median offsets are 0.13 and 0.28 dex, with standard deviations of 0.34 and 0.26 dex, respectively). These results do not change significantly for small changes of the critical gas surface density at which the sample is divided into bins of low or high surface density. We test the robustness of these results with respect to the choice of the gas surface density threshold in Figure C1, and confirm that the transition between these two regimes occurs between 7–9 $M_\odot\,pc^{-2}$. In addition, we have verified that the result is robust against the removal of outliers in the data. This is not surprising, given that the central parts of the cumulative distributions are relatively steep.

The existence of two regimes[18] regulating the molecular cloud lifetime at low and high density can be understood by considering the fraction of the gas reservoir probed by CO. We assume that star formation takes place in compact overdensities, which can be more or less uniquely traced by CO in environments of different gas surface density. At high molecular gas surface densities, CO is visible almost everywhere in the galaxy, including the space in between the compact overdensities in which star formation takes place, and may extend beyond the cloud tidal radii. As a result, even after filtering the diffuse emission on large scales, the remaining reservoir of CO-emitting molecular gas is spatially extended and is more likely to be affected by large-scale galactic dynamical processes. At low molecular gas surface densities, CO traces only the densest parts of the clouds, i.e. the overdensities that participate in star formation, and most of the gas reservoir in between is likely to be atomic (e.g. Schruba et al. 2011). The collapse of the

---

[17] One might instead expect a division based on the cloud surface density contrast with respect to the kpc-scale surface density used here, such that galactic dynamics become more important at low density contrasts. This is consistent with our suggestion of a critical large-scale surface density, because the cloud surface density contrast decreases with large-scale gas surface density (see eq. 9 of Kruijssen 2015).

[18] Of course, these two regimes of internal and galactic dynamics may be subdivided further. This likely requires adding physical dependences beyond the correlation with gas surface density highlighted here. For instance, the internal dynamical processes can be separated into the gravitational free-fall or the crossing time, depending on whether or not a cloud is gravitationally bound. Likewise, the galactic dynamical processes can be separated into the several terms of equation (9), with e.g. shear outperforming other processes towards high Toomre Q and shallow rotation curves (Jefferson & Kruijssen 2018).
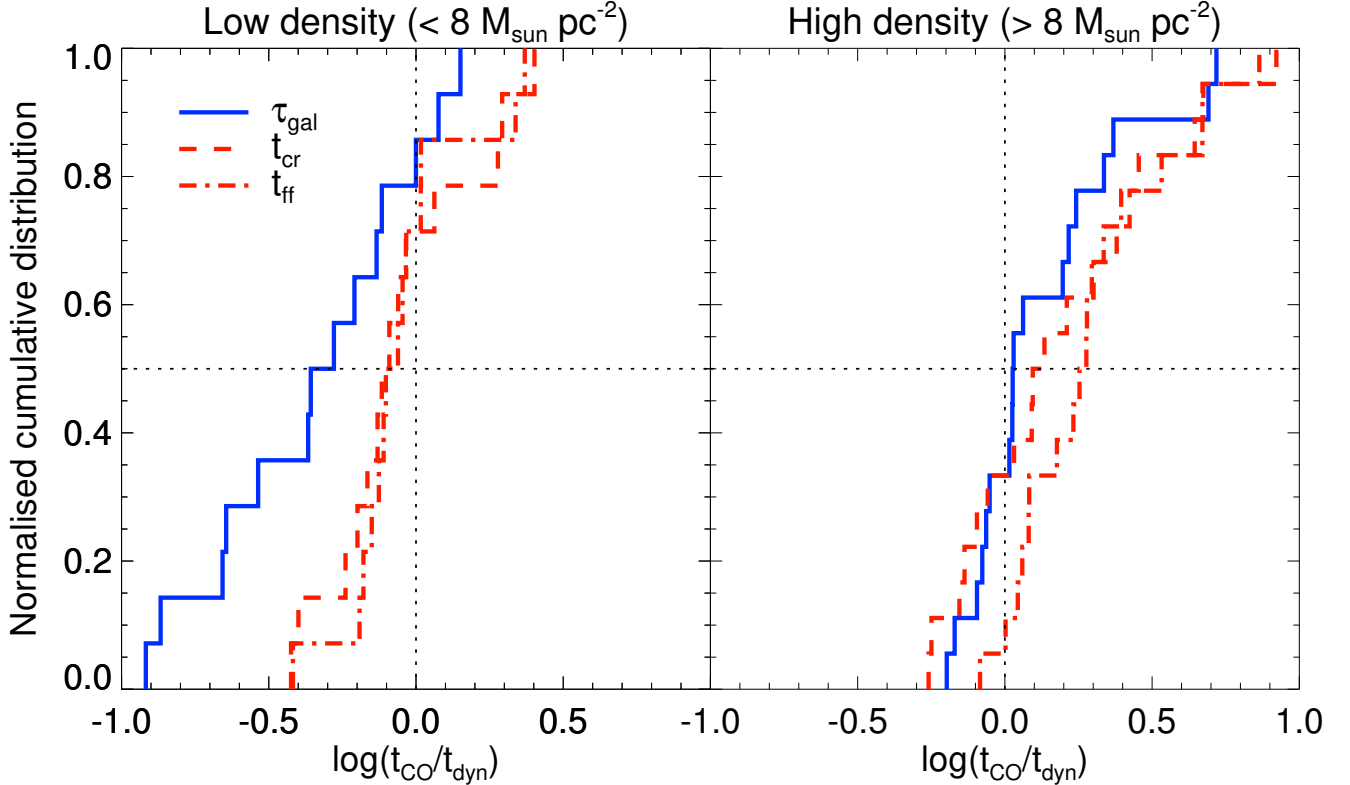
Figure 6. Comparison of the measured molecular cloud lifetimes (t_{CO}) with the predicted cloud lifetimes from galactic dynamics (τ_{gal}, from Jefferson & Kruijssen 2018) and internal dynamics (the cloud crossing time, t_{cr}, and the cloud free-fall time, t_{ff}) for all radial bins with low kpc-scale gas surface densities ($\Sigma_{H_2, ring} < 8\, M_\odot\, pc^{-2}$, left) and those with high kpc-scale gas surface densities ($\Sigma_{H_2, ring} > 8\, M_\odot\, pc^{-2}$, right). Shown are the normalised cumulative distributions of the difference in logarithmic space between t_{CO} and each of the predicted dynamical time-scales (see the legend), defined as $\log(t_{CO}/t_{dyn})$. These distributions do not include the radial bins affected by galactic morphology (light blue data points in Figure 5). In each panel, the horizontal dotted line indicates the median of the distribution and the vertical dotted line indicates perfect agreement between t_{CO} and t_{cloud}. Better agreement between t_{CO} and any of the three time-scales considered here manifests itself as steeper lines crossing more closely to the intersection of both dotted lines. These panels show that cloud lifetimes in regions with low surface densities correlate best with the time-scale for internal dynamical processes (median offset of $0.06-0.09$ dex, as opposed to 0.28 dex for galactic dynamics), whereas those in regions with high surface densities correlate best with the time-scale for galactic dynamical processes (median offset of 0.03 dex, as opposed to $0.13-0.28$ dex for internal dynamics). See the text and Appendix C for details.

CO-emitting part of a cloud is therefore likely decoupled from the galactic dynamics and represents a local process. As a result, the CO-bright cloud lifetimes in low-surface density environments are not expected to be set by the external galactic dynamics, but rather by internal dynamics such as the (CO-)cloud free-fall or crossing time. This regime of 'island GMCs' evolving on an internal dynamical time manifests itself e.g. in the outskirts of NGC4303 and NGC4535, as well as overall in the low molecular gas surface density galaxies NGC3351 and NGC5068, where the measured t_{CO} is consistent with the cloud free-fall time or the cloud crossing time.

We note that the environments with high gas surface densities exhibit a similar spread of $\log(t_{CO}/t_{dyn})$ for galactic dynamics (0.27 dex) and internal dynamics ($0.26-0.34$ dex). However, the medians differ, such that $t_{CO} \approx \tau_{gal} \approx 1.3t_{cr} \approx 1.9t_{ff}$. Therefore, the observed cloud lifetimes are equally well described as matching the galactic dynamical time-scale, as being equal to 1.9 times the internal free-fall time or 1.3 times the cloud crossing time. This is not unexpected, because the GMC internal dynamical time becomes proportional to the galactic dynamical time in the regime where galactic dynamics set the time-scale for cloud evolution (this is referred to as the 'Toomre regime' by Krumholz et al. 2012).

Even though the time-scales are proportional to each other in this regime, the fundamental dependence is on galactic dynamics, to which the internal dynamics of the clouds equilibrate.

The analytical predictions from Jefferson & Kruijssen (2018) are based on a simple analytical model, which limits the direct comparison with our measurement. In particular, the model does not distinguish between the different gas phases, but describes the lifetime of the entire gas concentration, irrespective of its phase. As a result, it is not surprising that the analytical predictions over-estimate the lifetime of the CO clouds in regions of low H_2 density, where a large part of a gas cloud is atomic and not CO-emitting. Several studies have shown that the atomic-to-molecular transition occurs at atomic gas surface densities $\Sigma_{gas} \approx 10\, M_\odot\, pc^{-2}$ at near-solar metallicity (e.g. Wong & Blitz 2002; Leroy et al. 2008; Schruba et al. 2011; Krumholz 2014; Schruba et al. 2018), which is close to the critical molecular gas surface density of $\Sigma_{H_2, ring} = 8\, M_\odot\, pc^{-2}$ below which our cloud lifetimes correlate more strongly with the cloud's internal dynamical time-scales than with the galactic dynamical time-scale from Jefferson & Kruijssen (2018). This also explains why our results show that t_{CO} often decreases (or stays constant) with increasing galactocentric ra-

dius (see Figure 5), whereas the analytically predicted τ_{gal} typically gradually increases towards the outskirts of the galaxies (scaling with Ω^{-1}). In the outskirts of galaxies, the gas reservoir often becomes atomic gas-dominated (e.g. Schruba et al. 2011), causing the CO lifetime measurements to only trace the final phase of cloud collapse. As a result, the analytical theory provides an upper limit to the true cloud lifetimes in this atomic-dominated regime.

In the regions where our measurements are well-reproduced by the analytical theory of Jeffreson & Kruijssen (2018), which happens at small-to-intermediate galactocentric radii for most of the galaxies in our sample (NGC628, NGC3627, NGC4254, NGC4303, NGC4321, NGC4535, and NGC5194), the mid-plane free-fall time $\tau_{\mathrm{ff,g}}$ is generally the shortest of the time-scales included in τ_{gal}. When comparing our measured cloud lifetimes with the other individual characteristic time-scales in equation (9), we can rule out cloud-cloud collisions and spiral arm passages as important mechanisms limiting cloud lifetimes, since they typically act on much longer characteristic time-scales ($\sim 100\,\mathrm{Myr}$; see also Jeffreson & Kruijssen 2018). This suggests that the gravitational collapse of the ISM mainly regulates the cloud lifetime in the molecular-dominated discs of star-forming galaxies, and that clouds are not long-lived: they collapse, form stars, and get disrupted by feedback.

6 DISCUSSION

We now briefly validate our measurements by verifying that all requirements listed in Kruijssen et al. (2018) have been met. In addition, we carry out a comparison to other cloud lifetime measurements from the literature. The section is concluded with a discussion of the physical implications of our results for the GMC lifecycle in galaxies.

6.1 Accuracy of the results

In Sections 4.2 and 4.3, we have presented the results from applying our statistical analysis method (using the HEISENBERG code) to our sample of disc galaxies. To validate the accuracy of these values, we verify here that we fulfill the requirements listed in sect. 4.4 of Kruijssen et al. (2018). The following criteria guarantee that the three derived parameters t_{gas}, t_{fb}, and λ are measured with an accuracy of at least 30 per cent (but often better):

(i) The durations of the gas and young stellar phases differ by less than an order of magnitude, with $|\log_{10}(t_{\mathrm{star}}/t_{\mathrm{gas}})| \leqslant 0.53$ for all galaxies (Tables 3 and 4).

(ii) In all cases, we verify that $\lambda \geqslant l_{\mathrm{ap,min}}$, which implies that the region separation length is sufficiently resolved by our observations to obtain a reliable measurement of t_{fb}. Quantitatively, we have $\lambda \geqslant 1.7 l_{\mathrm{ap,min}}$ for all galaxies (Tables 3 and 4)

(iii) We choose the galactocentric bins to have a minimum of 50 identified emission peaks of each type in each bin and a minimum width of 1 kpc (which is needed to fulfill the assumption of randomly distributed regions on a scale of a few times λ). A fortiori, we respect the condition $N_{\mathrm{min}} \equiv \min(N_{\mathrm{peak,star}}, N_{\mathrm{peak,gas}}) \geqslant 35$ for each galactocentric bin (and each galaxy) necessary to ensure relative uncertainties of less than 50 per cent on the derived quantities. For $\geqslant 50$ peaks per tracer, we obtain relative uncertainties of $\leqslant 30$ per cent (see fig. 25 of Kruijssen et al. 2018).

(iv) Focusing on an SFR or a gas peak should never lead to a deficit of this tracer relative to a galactic average. This condition is not fulfilled before we filter out diffuse emission. This applies in particular when focusing on Hα peaks for most galaxies, because the Hα maps have larger diffuse emission reservoirs than the CO maps, which is also visible directly in Figure 1. After the filtering of the diffuse emission (Section 3.4), this criterion is satisfied.

(v) The global star formation histories (SFHs) of the galaxies should be relatively constant over a time interval τ (i.e. $15-35\,\mathrm{Myr}$ for our measurements), so that the evolutionary timelines (including the CO-bright phase) are homogeneously sampled. Unfortunately, the spatially-resolved SFHs of the galaxies in our sample are not known. NGC3627 is interacting with the neighbouring galaxy NGC3628 (e.g. Rots 1978; Haynes et al. 1979), but all other galaxies in our sample are not expected to have significant variations of their SFR in the disc during the last $\sim 50\,\mathrm{Myr}$. We note in particular that this is the case for NGC5194 (Eufrasio et al. 2017; Tress et al. 2019), despite its relatively recent interaction with NGC5195, ~ 350-$500\,\mathrm{Myr}$ ago (Salo & Laurikainen 2000; Mentuch Cooper et al. 2012; Eufrasio et al. 2017). The condition that the SFR averaged over age intervals with a width of t_{star} or t_{gas} should not vary by more than 0.2 dex as function of age for $t \leqslant \tau$ is therefore highly likely to be satisfied on galactic scales. This ensures that any bias of the measured t_{gas} due to possible SFR variations is less than 50 per cent. Note that this condition is likely not fulfilled for at least some of the bins covering bars or the tips of bars. The stochasticity and synchronised, bursty nature of the star formation events in these regions therefore leads to large uncertainties or biases on the cloud lifetime. In these regions, the measured t_{gas} becomes dependent on the precise moment of observation (see Section 5.3).

The fulfillment of the above criteria guarantees the accuracy of the constraints obtained for t_{gas} and λ. Additional requirements apply to ensure the accuracy of t_{fb}. While we have verified that these are satisfied, we defer a detailed discussion to the companion paper focusing on the feedback time-scale (M. Chevance et al. in prep.).

6.2 Comparison with previous work

Previous studies of individual galaxies have led to a variety of measured molecular cloud lifetimes, using different techniques to infer these. Cloud lifetimes with similarly short values as in the present study ($10-30\,\mathrm{Myr}$) have been measured by counting clouds or classifying clouds based on their stellar content (e.g. Elmegreen 2000; Hartmann et al. 2001; Engargiola et al. 2003; Kawamura et al. 2009; Meidt et al. 2015; Corbelli et al. 2017). Similar values have been obtained by using the spiral arm pattern speed and local circular velocity to convert the offsets between H II regions and molecular clouds into evolutionary time-scales (Egusa et al. 2009). By contrast, much longer values of over 100 Myr have been suggested by the presence of molecular clouds in the inter-arm regions of nearby spiral galaxies (Scoville & Hersh 1979; Scoville & Wilson 2004; Koda et al. 2009), while a much shorter value of $\sim 1\,\mathrm{Myr}$ has been measured in the Central Molecular Zone (i.e. the central $\sim 500\,\mathrm{pc}$ of the Milky Way), by following clouds along a known gas orbit (Kruijssen et al. 2015; Henshaw et al. 2016; Barnes et al. 2017; Jeffreson et al. 2018).

These previous studies have made major progress in tackling the fundamental problem of measuring the evolutionary timeline of cloud-scale star formation and feedback. At the same time, they have faced several immediate challenges. First, by their pioneering nature, they targeted single galaxies. Taken together, these studies therefore lack the homogeneity of definitions needed to make

direct comparisons between galaxies and determine whether the differences between galaxies are physical in nature or result from differences in experiment design. Related to this, previous works used different weighing schemes for quantifying the average cloud lifecycle, e.g. using a number-weighted average or a flux-weighted average (as is done in this paper). Secondly, several of these studies rely on defining and classifying GMCs and H II regions, which is necessarily subjective. Reliable GMC classifications have often required resolving individual clouds or star-forming regions (of a few tens of parsec), which has so far obstructed systematic measurements of the molecular cloud lifetime outside of the Local Group. While the methodology used in this paper does not differ fundamentally in terms of its broader philosophy, a key change is that it has tried to eliminate the subjectivity of GMC classification and therefore does not require to resolve individual regions, increasing its reproducibility and applicability. Finally, some of these studies primarily investigated the effects of a single dynamical mechanism (e.g. spiral arm perturbations) without considering the variety of possible processes affecting clouds.

By using the unified framework provided by Kruijssen et al. (2018), it is now possible to build on the broad foundation laid by previous studies and probe the variation of the molecular cloud lifetime as a function of environment, both between and within galaxies. In this paper, we present homogeneous measurements of the molecular cloud lifetime for nine different galaxies, finding that they are short, with values between $10-30$ Myr for galaxy-averaged cloud lifetimes and typically a factor of $\gtrsim 2$ variation within galaxies (as presented in Figure 5). This is consistent with the lifetimes of molecular clouds measured in NGC300 ($10.8^{+2.1}_{-1.7}$ Myr, Kruijssen et al. 2019) and M33 (16.7 ± 2.1 Myr, Hygate et al. 2019a) using the same statistical formalism. We do not find any dependence of the measured evolutionary timelines on the strength or the number of spiral arms in the galaxies of our sample. This suggests that, while spiral arms may instigate molecular cloud formation, the subsequent evolution of the clouds is likely governed by the processes identified in this work (i.e. dynamics and stellar feedback) irrespectively of the presence of spiral arms. As a result, we suggest that the offsets between molecular clouds and H II regions perpendicular to spiral arms that have been used to infer evolutionary time-scales (e.g. Egusa et al. 2009; Meidt et al. 2015) are driven primarily by cloud evolution and feedback rather than by dynamical drift alone.

In Figure 7, we compare the GMC lifetimes measured in this study with the cloud lifetimes inferred by Meidt et al. (2015) in NGC5194 (M51). Meidt et al. (2015) use the variation of the GMC number density as a function of the azimuthal coordinates to estimate the cloud lifetimes as a fraction of the inter-arm travel time. We observe a broad agreement between the range of lifetimes obtained by both methods, although the exact values differ from bin to bin. The discrepancy is the largest in the second radial bin ($1.8-2.9$ kpc) and may exist for two different reasons. First, the galactocentric bins considered by Meidt et al. (2015) are relatively small (width of 0.3 kpc) and therefore include a small number of clouds (between 4 and 23). This affects how well the different phases of the evolutionary cycle from clouds to young stellar regions are sampled in a given bin, making the results sensitive to stochasticity. Secondly, related to the previous point, the method assumes a constant rate of change in the cloud population with time for each individual bin. While this type of statistical equilibrium may apply across the full cloud population, it is less likely to apply to smaller sub-populations, either due to stochasticity as in the previous point, or due to systematic changes in the local conditions. When using statistical inference to measure the cloud life-
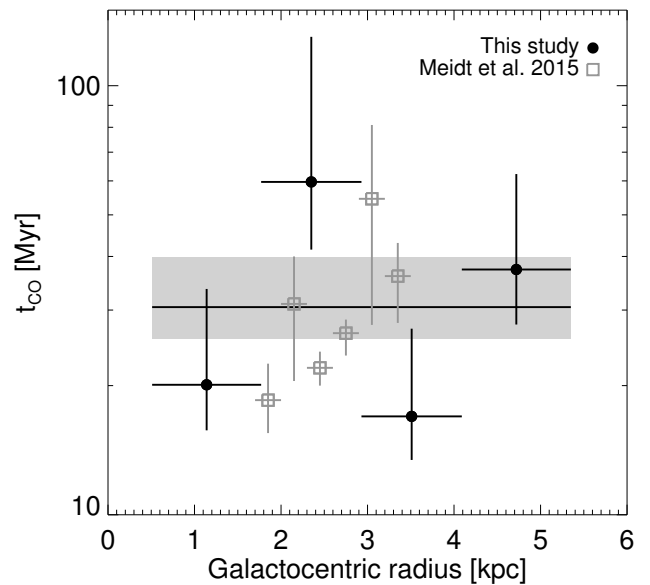

Figure 7. Comparison of our GMC lifetime measurements in NGC5194 (black) to those from Meidt et al. (2015) (grey) as a function of galactocentric radius. The horizontal black line represents the average GMC lifetime across the entire galaxy, with the uncertainties indicated by the grey-shaded area.

time, these two reasons imply that the dispersion within a bin (and therefore the uncertainties on the measurement) scale directly with the size of the (sub-)population under consideration. This plausibly explains why the cloud lifetimes and their uncertainties differ between both methods.

Finally, Schinnerer et al. (2019) present estimates for the duration of the CO-bright phase for eight of the galaxies considered here (all except NGC4303) using pixel statistics. Specifically, that work presents the ratio between the number of CO-bright pixels and the number of Hα-bright pixels (above a chosen flux density threshold) and discusses how this could be interpreted as the ratio between the visibility time-scales of both tracers. The relative simplicity of pixel statistics has the great advantage that it is highly reproducible, but it also means that it may not be straightforward to translate them directly into time-scales. For this reason, Schinnerer et al. (2019) highlight several of the caveats associated with this temporal interpretation. Figure 8 quantitatively tests this hypothesis by comparing their measurements to the time-scale ratios measured here. The figure shows that the pixel-based approach is in order-of-magnitude agreement with our measurements, but systematically underestimates the GMC lifetime by a factor of ~ 2 on average. The order-of-magnitude agreement is encouraging, even if the systematic bias and the presence of two strong outliers (NGC3351 and NGC5068) at the bottom of the diagram caution against using pixel statistics as a quantitative tracer of the cloud lifetime.

The difference between our GMC lifetimes and the fractions of CO-bright pixels can be understood as the result of differences in methodology. First, there is a difference in how either approach deals with blending between regions. The analysis of this paper self-consistently accounts for blending effects towards coarser resolutions, and uses these effects to measure the separation scales of the units undergoing evolutionary cycling. Conversely, the number ratio between CO-bright and Hα-bright pixels by definition approaches unity towards coarser resolutions, implying $t_{CO}/t_{H\alpha} \sim 1$
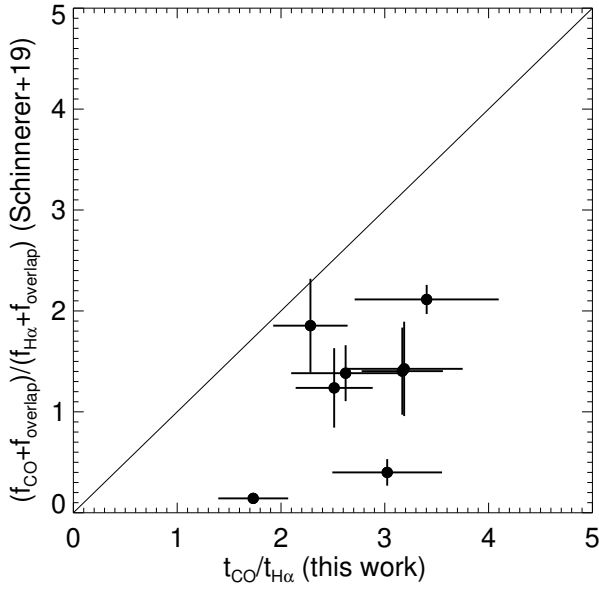
Figure 8. Comparison of our measured GMC lifetimes in units of the Hα emission time-scale (*x*-axis) to the estimates based on pixel statistics from table 5 of Schinnerer et al. (2019) (*y*-axis) for the eight full galaxies in common between both studies. The diagonal line shows the 1:1 relation.

without a physical similarity between the underlying time-scales. Because $t_{\mathrm{H}\alpha} < t_{\mathrm{CO}}$ for all galaxies, this leads to a systematic bias. Secondly, using the number of pixels bright in either tracer as a proxy for the lifetimes of regions assumes that all regions have the same size (or area). This particularly affects NGC3351 and NGC5068, where the visible extent of the CO clouds is typically smaller than that of the HII regions. This leads to an underestimation of the time-scales inferred from pixel statistics. The analysis presented here avoids this by accounting for differences in region size between both tracer maps (see Section 3 and Kruijssen et al. 2018). In summary, the quantitative differences between the results of both approaches are a natural result of differences in methodology. This comparison demonstrates that pixel statistics are a good qualitative probe of the GMC lifecycle, but do not perform as well when used as a quantitative metric of the GMC lifetime. Together, the pixel statistics presented in Schinnerer et al. (2019) and the results presented here constitute critical and complementary empirical observables that simulations of galactic-scale star formation will need to reproduce (see e.g. Fujimoto et al. 2019).

6.3 Implications for the GMC lifecycle in galaxies

The results presented in Section 4 reveal that the de-correlation between molecular gas and young stellar regions at $\sim 100\,\mathrm{pc}$ scales is ubiquitous across our galaxy sample. The fact that GMCs and HII regions rarely coexist on these small scales indicates the rapid evolutionary cycling between GMCs, star formation and feedback. This has previously been shown in two very nearby ($D < 2\,\mathrm{Mpc}$) galaxies using the same method (e.g. NGC300, Kruijssen et al. 2019; M33, Hygate et al. 2019a) and we can now generalise this result to a much larger sample of galaxies.

The significant variation of the molecular cloud lifetime measured homogeneously across a sample of nine galaxies demonstrates that the cycling between gas and stars is not quantitatively

universal, but exhibits a clear environmental dependence. In environments with high kpc-scale molecular gas surface densities ($\Sigma_{\mathrm{H}_2,\mathrm{ring}} > 8\,\mathrm{M}_\odot\,\mathrm{pc}^{-2}$), our measurements correlate most strongly with the predicted time-scales based on galactic dynamical processes from Jeffreson & Kruijssen (2018). This shows the importance of galactic dynamics in setting the cloud lifetime, and hence its role in regulating the star formation process. In most cases, this predicted dynamical timescale τ_{gal} is dominated by the time-scale for the gravitational free-fall of the mid-plane ISM ($t_{\mathrm{ff,g}}$) and for dispersal by shear (t_β). In environments with low kpc-scale molecular gas surface densities ($\Sigma_{\mathrm{H}_2,\mathrm{ring}} < 8\,\mathrm{M}_\odot\,\mathrm{pc}^{-2}$), GMCs become decoupled from the large-scale galactic dynamics and the molecular cloud lifetime is consistent with being set by the cloud's internal dynamical time (t_{ff} or t_{cr}).

The short duration of the feedback phase measured in Section 4.3 ($t_{\mathrm{fb}} = 1\text{−}5\,\mathrm{Myr}$) lends further support to a highly dynamic view of the ISM. For several galaxies, the feedback time-scale is shorter than the typical minimum time of 4 Myr for supernovae to explode (e.g. Leitherer et al. 2014), indicating that early (stellar) feedback mechanisms are responsible for dispersing the parent molecular cloud within a short time-scale. This means that photoionisation and stellar winds are likely to play an essential role in the rapid destruction of the molecular cloud after the onset of massive star formation. Without a quantitative comparison to theoretical predictions, it is not possible determine whether the parent GMC is destroyed by a phase transition or by kinetic dispersal, i.e. whether the remaining molecular gas is photodissociated or merely separated from the young stellar population, potentially broken up in several smaller diffuse clouds. We are currently undertaking such an analysis for the galaxy sample presented here (M. Chevance et al. in prep.), where this question will be addressed in more detail.

7 CONCLUSION

We present a systematic measurement of the characteristic time-scales describing the lifecycle of molecular clouds, star formation, and feedback, for a sample of nine nearby star-forming disc galaxies, using cloud-scale ($\sim 100\,\mathrm{pc}$) resolution imaging of CO and Hα, obtained as part of the PHANGS collaboration. We employ the multi-scale, multi-wavelength statistical method presented in Kruijssen & Longmore (2014) and Kruijssen et al. (2018) to measure the molecular cloud lifetime and the feedback time-scale, which are critical for constraining the physical processes regulating star formation at the cloud scale. These quantities could previously be obtained only for a handful of single galaxies, mostly restricted to the Local Group, and the heterogeneity of methods used did not enable direct comparisons between different studies. As a result, it was unclear if the variety of cloud lifetimes in the literature (ranging between 1 Myr and > 100 Myr) is caused by differences in experiment design or reflects a variety of physical conditions and processes. By applying a rigorous, statistical analysis method homogeneously to a sample of nine galaxies, we are now able to determine the quantities describing the cloud lifecycle systematically across a wide range of galactic environments.

Across our sample of nine star-forming disc galaxies, our analysis method reveals a universal de-correlation of CO and Hα emission on the cloud scale ($\sim 100\,\mathrm{pc}$), indicating a rapid evolutionary lifecycle in which star formation is fast and inefficient: molecular clouds live for a (cloud-scale or galactic, see below) dynamical time, form stars, and get disrupted by feedback. Our results show that star-forming disc galaxies can be described as ensembles of in-

dependent building blocks, separated by $\lambda = 100-300$ pc, undergoing a rapid evolutionary cycle from molecular clouds to young stellar regions. We measure relatively short molecular cloud lifetimes of $t_{CO} = 10-30$ Myr, with statistically significant variations, both between and within galaxies. The fact that these cloud lifetimes are much shorter than the molecular gas depletion time (~ 2 Gyr) implies that the integrated star formation efficiency per star formation event is low; we obtain values in the range of $\epsilon_{sf} = 4-10$ per cent.

Molecular clouds experience a long 'inert' or 'isolated' phase, taking $75-90$ per cent of their total lifetime, during which they show no signs of massive star formation. When massive stars do emerge, towards the end of the cloud lifecycle, the parent cloud is dispersed within $t_{fb} = 1-5$ Myr, strongly suggesting that cloud dispersal is driven by stellar feedback. The short duration of this 'feedback time-scale', which represents the time between the emergence of the first ionising photons due to massive star formation and the eventual destruction or dispersal of the parent molecular cloud, indicates that early (stellar) feedback such as photoionisation or stellar winds plays a major role in this process, acting before the first supernovae explode. We will present a detailed investigation of the relative importance of different feedback mechanisms (supernovae, photoionisation, stellar winds, and radiation pressure) in GMC dispersal in a companion paper, by comparing the feedback time-scales measured here to theoretical predictions (M. Chevance et al. in prep.).

The above quantities are consistent with the results obtained by applying this method to NGC300 (Kruijssen et al. 2019) and M33 (Hygate et al. 2019a), but we extend these to a more representative sample of star-forming main sequence galaxies. In addition, by using a single analysis method to measure the molecular cloud lifetime across a sample of galaxies, we are now able to demonstrate how it varies with the galactic environment, both between galaxies and within them. We distinguish two regimes, in which the GMC lifetime is set by different physical mechanisms. In environments with high kpc-scale molecular gas surface densities ($\Sigma_{H_2,ring} \geqslant 8\,M_\odot pc^{-2}$), the cloud lifetime is regulated by galactic dynamics, mostly by a combination of the gravitational free-fall of the mid-plane ISM and shear. Spiral arm crossings and cloud-cloud collisions take place on considerably longer (~ 100 Myr) time-scales and are too rare to systematically drive cloud evolution across the cloud population. In environments with low kpc-scale molecular gas surface densities ($\Sigma_{H_2,ring} \leqslant 8\,M_\odot pc^{-2}$), GMCs decouple from the dynamics of the host galaxy, with CO-devoid regions separating them from other GMCs, and the cloud lifetime correlates with the cloud crossing and free-fall times, showing that cloud evolution is regulated by internal dynamics. The division between these two regimes in galactic molecular gas surface density coincides with the atomic-to-molecular gas transition occurring near the above density limit (Wong & Blitz 2002; Leroy et al. 2008; Krumholz 2014; Schruba et al. 2018). In addition to these general trends, we find that GMC lifetimes can be elevated near the co-rotation radius.

The quantitative variation of the evolutionary timeline describing the cloud lifecycle reveals that the processes that regulate cloud-scale star formation and feedback in galaxies are environmentally dependent. Therefore, to determine the relevant environmental quantities (e.g. galactic dynamics, disc structure, ISM pressure) affecting the cycle of cloud evolution, star formation, and feedback, it is necessary to extend the analysis performed in this work to a larger number of galaxies, covering a broad range of environments and morphology. The systematic application of this method to a large fraction of all massive star-forming disc galaxies

within 17 Mpc will soon be possible with the on-going PHANGS-ALMA Large Programme and will be presented in J. Kim et al. (in prep.). This will allow us to quantitatively assess how the efficiency and lifecycle of star-formation and feedback depends on the galactic environment. We expect that this work will contribute to characterising the multi-scale physics driving these lifecycles and move away from a quasi-static picture of star formation in galaxies, instead describing it in terms of the mass flows generated by cloud-scale accretion and stellar feedback. This will represent key empirical input for a predictive theory of how galaxies grow and form stars, as well as for sub-grid models for star formation and feedback in galaxy simulations.

data: ADS/JAO.ALMA #2012.1.00650.S, ADS/JAO.ALMA #2015.1.00925.S, ADS/JAO.ALMA #2015.1.00956.S. ALMA is a partnership of ESO (representing its member states), NSF (USA) and NINS (Japan), together with NRC (Canada), NSC and ASIAA (Taiwan), and KASI (Republic of Korea), in cooperation with the Republic of Chile. The Joint ALMA Observatory is operated by ESO, AUI/NRAO and NAOJ. The National Radio Astronomy Observatory is a facility of the National Science Foundation operated under cooperative agreement by Associated Universities, Inc. This paper makes use of the PdBI Arcsecond Whirlpool Survey (Schinnerer et al. 2013; Pety et al. 2013). The IRAM 30-m telescope and PdBI are run by IRAM, which is supported by INSU/CNRS (France), MPG (Germany) and IGN (Spain). The results presented in this paper made use of THINGS, 'The HI Nearby Galaxy Survey' (Walter et al. 2008). This work has made use of data from the European Space Agency (ESA) mission *Gaia* (https://www.cosmos.esa.int/gaia), processed by the *Gaia* Data Processing and Analysis Consortium (DPAC, https://www.cosmos.esa.int/web/gaia/dpac/consortium). Funding for the DPAC has been provided by national institutions, in particular the institutions participating in the *Gaia* Multilateral Agreement.

REFERENCES

Asplund M., Grevesse N., Sauval a. J., Scott P., 2009, ARA&A, 47, 481
Bally J., 2016, ARA&A, 54, 491
Barnes A. T., Longmore S. N., Battersby C., Bally J., Kruijssen J. M. D., Henshaw J. D., Walker D. L., 2017, MNRAS, 469, 2263
Bertoldi F., McKee C. F., 1990, ApJ, 354, 529
Beuther H., Meidt S., Schinnerer E., Paladino R., Leroy A., 2017, A&A, 597, A85
Bigiel F., Leroy A., Walter F., Brinks E., de Blok W. J. G., Madore B., Thornley M. D., 2008, AJ, 136, 2846
Bigiel F., Walter F., Blitz L., Brinks E., de Blok W. J. G., Madore B., 2010, AJ, 140, 1194
Bigiel F., et al., 2011, ApJ, 730, L13
Binette L., Magris C. G., Stasińska G., Bruzual A. G., 1994, A&A, 292, 13
Blanc G. A., Heiderman A., Gebhardt K., Evans Neal J. I., Adams J., 2009, ApJ, 704, 842
Blitz L., Fukui Y., Kawamura A., Leroy A., Mizuno N., Rosolowsky E., 2007, in Reipurth B., Jewitt D., Keil K., eds, , Protostars and Planets V. University of Arizona Press, Tucson, p. 81
Boissier S., Prantzos N., Boselli A., Gavazzi G., 2003, MNRAS, 346, 1215
Bolatto A. D., Leroy A. K., Rosolowsky E., Walter F., Blitz L., 2008, ApJ, 686, 948
Bolatto A. D., Wolfire M., Leroy A. K., 2013, ARA&A, 51, 207
Brinchmann J., Charlot S., White S. D. M., Tremonti C., Kauffmann G., Heckman T., Brinkmann J., 2004, MNRAS, 351, 1151
Caldú-Primo A., Schruba A., Walter F., Leroy A., Bolatto A. D., Vogel S., 2015, AJ, 149, 76
Cepa J., Beckman J. E., 1990, ApJ, 349, 497
Chabrier G., 2005, in Corbelli E., Palla F., Zinnecker H., eds, Astrophysics and Space Science Library Vol. 327, The Initial Mass Function 50 Years Later. p. 41 (arXiv:astro-ph/0409465), doi:10.1007/978-1-4020-3407-7_5
Collins J. A., Rand R. J., 2001, ApJ, 551, 57
Corbelli E., et al., 2017, A&A, 601, A146
Daddi E., et al., 2010, ApJ, 714, L118
Dale J. E., 2015, New Astronomy Reviews, 68, 1
Dale J. E., Ngoumou J., Ercolano B., Bonnell I. A., 2014, MNRAS, 442, 694
Dettmar R. J., 1990, A&A, 232, L15
Dobbs C. L., Pringle J. E., 2013, MNRAS, 432, 653
Dobbs C. L., Burkert A., Pringle J. E., 2011, MNRAS, 413, 2935

Dobbs C. L., et al., 2014, Protostars and Planets VI, 3, 25
Dobbs C. L., Pringle J. E., Duarte-Cabral A., 2015, MNRAS, 446, 3608
Egusa F., Kohno K., Sofue Y., Nakanishi H., Komugi S., 2009, ApJ, 697, 1870
Eldridge J. J., Stanway E. R., Xiao L., McClelland L. A. S., Taylor G., Ng M., Greis S. M. L., Bray J. C., 2017, Publ. Astron. Soc. Australia, 34, e058
Elmegreen B. G., 2000, ApJ, 530, 277
Elmegreen B. G., Elmegreen D. M., Seiden P. E., 1989, ApJ, 343, 602
Elmegreen B. G., Elmegreen D. M., Montenegro L., 1992, ApJS, 79, 37
Elmegreen B. G., Elmegreen D. M., Efremov Y. N., 2018, ApJ, 863, 59
Engargiola G., Plambeck R., Rosolowsky E., Blitz L., 2003, ApJS, 149, 343
Eufrasio R. T., et al., 2017, ApJ, 851, 10
Faesi C. M., Lada C. J., Forbrich J., 2018, ApJ, 857, 19
Feldmann R., Gnedin N. Y., Kravtsov A. V., 2011, ApJ, 732, 115
Fitzpatrick E. L., 1999, PASP, 111, 63
Flores-Fajardo N., Morisset C., Stasińska G., Binette L., 2011, MNRAS, 415, 2182
Freeman P., Rosolowsky E., Kruijssen J. M. D., Bastian N., Adamo A., 2017, MNRAS, 468, 1769
Fujimoto Y., Tasker E. J., Wakayama M., Habe A., 2014, MNRAS, 439, 936
Fujimoto Y., Chevance M., Haydon D. T., Krumholz M. R., Kruijssen J. M. D., 2019, MNRAS, 487, 1717
Gaia Collaboration et al., 2016, A&A, 595, A1
Gaia Collaboration et al., 2018, A&A, 616, A1
Garcia-Burillo S., Sempere M. J., Combes F., Neri R., 1998, A&A, 333, 864
Genzel R., et al., 2010, MNRAS, 407, 2091
Genzel R., et al., 2011, ApJ, 733, 101
Goddard Q. E., Kennicutt R. C., Ryan-Weber E. V., 2010, MNRAS, 405, 2791
Gonzalez R. A., Graham J. R., 1996, ApJ, 460, 651
Götberg Y., de Mink S. E., Groh J. H., Leitherer C., Norman C., 2019, A&A, 629, A134
Grand R. J. J., et al., 2017, MNRAS, 467, 179
Grasha K., et al., 2019, MNRAS, 483, 4707
Gratier P., et al., 2010, A&A, 522, A3
Greenawalt B. E., 1998, PhD thesis, New Mexico State University
Grudić M. Y., Hopkins P. F., Faucher-Giguère C.-A., Quataert E., Murray N., Kereš D., 2018, MNRAS, 475, 3511
Hannon S., et al., 2019, MNRAS, p. 2450
Hao C.-N., Kennicutt R. C., Johnson B. D., Calzetti D., Dale D. A., Moustakas J., 2011, ApJ, 741, 124
Hartmann L., Ballesteros-Paredes J., Bergin E. A., 2001, ApJ, 562, 852
Haydon D. T., Kruijssen J. M. D., Hygate A. P. S., Schruba A., Krumholz M. R., Chevance M., Longmore S. N., 2018, MNRAS submitted, p. arXiv:1810.10897
Haydon D. T., Fujimoto Y., Chevance M., Kruijssen J. M. D., Krumholz M. R., Longmore S. N., 2019, MNRAS submitted
Haynes M. P., Giovanelli R., Roberts M. S., 1979, ApJ, 229, 83
Hayward C. C., Hopkins P. F., 2017, MNRAS, 465, 1682
Henshaw J. D., et al., 2016, MNRAS, 457, 2675
Henshaw J. D., et al., 2019, submitted
Herrera C. N., et al., 2019, A&A in press, p. arXiv:1910.14311
Heyer M., Krawczyk C., Duval J., Jackson J. M., 2009, ApJ, 699, 1092
Hollyhead K., Bastian N., Adamo A., Silva-Villa E., Dale J., Ryon J. E., Gazak Z., 2015, MNRAS, 449, 1106
Hoopes C. G., Walterbos R. A. M., Greenwalt B. E., 1996, AJ, 112, 1429
Hopkins P. F., Narayanan D., Murray N., 2013, MNRAS, 432, 2647
Hopkins P. F., et al., 2018, MNRAS, 480, 800
Hughes A., et al., 2013, ApJ, 779, 46
Hygate A. P. S., Kruijssen J. M. D., Chevance M., Walter F., Schruba A., Kim J. J., Haydon D. T., Longmore S. N., 2019a, MNRAS submitted,
Hygate A. P. S., Kruijssen J. M. D., Chevance M., Schruba A., Haydon D. T., Longmore S. N., 2019b, MNRAS, 488, 2800
Jarrett T. H., et al., 2013, AJ, 145, 6
Jefferson S. M. R., Kruijssen J. M. D., 2018, MNRAS, 476, 3688

Jeffreson S. M. R., Kruijssen J. M. D., Krumholz M. R., Longmore S. N., 2018, MNRAS, 478, 3380
Kaplan K. F., et al., 2016, MNRAS, 462, 1642
Kawamura A., et al., 2009, ApJS, 184, 1
Kennicutt R. C. J., 1989, ApJ, 344, 685
Kennicutt R. C. J., 1998, ApJ, 498, 541
Kennicutt R. C., Evans N. J., 2012, ARA&A, 50, 531
Kennicutt R. C. J., et al., 2003, PASP, 115, 928
Kennicutt Jr. R. C., et al., 2009, ApJ, 703, 1672
Khoperskov S., Haywood M., Di Matteo P., Lehnert M. D., Combes F., 2018, A&A, 609, A60
Kim J.-G., Kim W.-T., Ostriker E. C., 2018, ApJ, 859, 68
Koda J., et al., 2009, ApJ, 700, L132
Kranz T., Slyz A., Rix H.-W., 2001, ApJ, 562, 164
Kreckel K., Blanc G. A., Schinnerer E., Groves B., Adamo A., Hughes A., Meidt S., 2016, ApJ, 827, 103
Kreckel K., et al., 2018, ApJ, 863, L21
Kreckel K., et al., 2019, ApJ in press, p. arXiv:1910.07190
Kruijssen J. M. D., 2015, MNRAS, 454, 1658
Kruijssen J. M. D., Longmore S. N., 2014, MNRAS, 439, 3239
Kruijssen J. M. D., Dale J. E., Longmore S. N., 2015, MNRAS, 447, 1059
Kruijssen J. M. D., Schruba A., Hygate A. P. S., Hu C.-Y., Haydon D. T., Longmore S. N., 2018, MNRAS, 479, 1866
Kruijssen J. M. D., et al., 2019, Nature, 569, 519
Krumholz M. R., 2014, Phys. Rep., 539, 49
Krumholz M. R., Dekel A., McKee C. F., 2012, ApJ, 745, 69
Krumholz M. R., Fumagalli M., da Silva R. L., Rendahl T., Parra J., 2015, MNRAS, 452, 1447
Krumholz M. R., Burkhart B., Forbes J. C., Crocker R. M., 2018, MNRAS, 477, 2716
Krumholz M. R., McKee C. F., Bland -Hawthorn J., 2019, ARA&A, 57, 227
Lacerda E. A. D., et al., 2018, MNRAS, 474, 3727
Lada C. J., Lombardi M., Alves J. F., 2010, ApJ, 724, 687
Lang P., et al., 2019, ApJ submitted
Lee J. C., Veilleux S., McDonald M., Hilbert B., 2016, ApJ, 817, 177
Leitherer C., Ekström S., Meynet G., Schaerer D., Agienko K. B., Levesque E. M., 2014, ApJS, 212, 14
Leroy A. K., Walter F., Brinks E., Bigiel F., de Blok W. J. G., Madore B., Thornley M. D., 2008, Astron. J., 136, 2782
Leroy A. K., et al., 2009, AJ, 137, 4670
Leroy A. K., et al., 2011, ApJ, 737, 12
Leroy A. K., et al., 2012, AJ, 144, 3
Leroy A. K., et al., 2013, AJ, 146, 19
Leroy A. K., et al., 2017a, Astrophys. J., 835, 1
Leroy A. K., et al., 2017b, ApJ, 846, 71
Leroy A. K., et al., 2019, ApJS, 244, 24
Madau P., Dickinson M., 2014, ARA&A, 52, 415
Martin C. L., Kennicutt Jr. R. C., 2001, ApJ, 555, 301
Mathis J. S., 1986, ApJ, 301, 423
McKee C. F., 1989, ApJ, 345, 782
McLeod A. F., et al., 2019a, ApJ submitted, p. arXiv:1910.11270
McLeod A. F., Dale J. E., Evans C. J., Ginsburg A., Kruijssen J. M. D., Pellegrini E. W., Ramsay S. K., Testi L., 2019b, MNRAS, 486, 5263
McMullin J. P., Waters B., Schiebel D., Young W., Golap K., 2007, in Shaw R. A., Hill F., Bell D. J., eds, Astronomical Society of the Pacific Conference Series Vol. 376, Astronomical Data Analysis Software and Systems XVI. p. 127
Meidt S. E., et al., 2012, ApJ, 744, 17
Meidt S. E., et al., 2013, ApJ, 779, 45
Meidt S. E., et al., 2014, ApJ, 788, 144
Meidt S. E., et al., 2015, ApJ, 806, 72
Meidt S. E., et al., 2018, ApJ, 854, 100
Meidt S. E., et al., 2019, ApJ submitted
Mentuch Cooper E., et al., 2012, ApJ, 755, 165
Miura R. E., et al., 2012, ApJ, 761, 37
Miville-Deschênes M.-A., Murray N., Lee E. J., 2017, ApJ, 834, 57
Monnet G., 1971, A&A, 12, 379

Murray N., 2011, ApJ, 729, 133
Murray N., Rahman M., 2010, ApJ, 709, 424
Oey M. S., et al., 2007, ApJ, 661, 801
Onodera S., et al., 2010, ApJ, 722, L127
Ostriker E. C., Shetty R., 2011, ApJ, 731, 41
Peeples M. S., Martini P., 2006, ApJ, 652, 1097
Pérez-González P. G., et al., 2006, ApJ, 648, 987
Peters T., et al., 2017, MNRAS, 466, 3293
Pety J., Falgarone É., 2000, A&A, 356, 279
Pety J., et al., 2013, ApJ, 779, 43
Pilyugin L. S., Grebel E. K., 2016, MNRAS, 457, 3678
Pilyugin L. S., Grebel E. K., Kniazev A. Y., 2014, AJ, 147, 131
Prescott M. K. M., et al., 2007, ApJ, 668, 182
Querejeta M., Meidt S. E., Schinnerer E., S^{4}G Collaboration 2014, in Iodice E., Corsini E. M., eds, Astronomical Society of the Pacific Conference Series Vol. 486, Multi-Spin Galaxies. p. 143
Querejeta M., et al., 2016, A&A, 588, A33
Querejeta M., et al., 2019, A&A, 625, A19
Rand R. J., Wallin J. F., 2004, ApJ, 614, 142
Rosolowsky E., Leroy A., 2006, PASP, 118, 590
Rots A. H., 1978, AJ, 83, 219
Salo H., Laurikainen E., 2000, MNRAS, 319, 377
Sandstrom K. M., et al., 2013, ApJ, 777, 5
Sarzi M., et al., 2010, MNRAS, 402, 2187
Scannapieco C., et al., 2012, MNRAS, 423, 1726
Schaller G., Schaerer D., Meynet G., Maeder A., 1992, A&AS, 96, 269
Scheepmaker R. A., Lamers H. J. G. L. M., Anders P., Larsen S. S., 2009, A&A, 494, 81
Schinnerer E., Maciejewski W., Scoville N., Moustakas L. A., 2002, ApJ, 575, 826
Schinnerer E., et al., 2013, ApJ, 779, 42
Schinnerer E., et al., 2017, ApJ, 836, 62
Schinnerer E., et al., 2019, ApJ in press, p. arXiv:1910.10520
Schlafly E. F., Finkbeiner D. P., 2011, ApJ, 737, 103
Schruba A., Leroy A. K., Walter F., Sandstrom K., Rosolowsky E., 2010, ApJ, 722, 1699
Schruba A., et al., 2011, AJ, 142, 37
Schruba A., et al., 2017, ApJ, 835, 278
Schruba A., Bialy S., Sternberg A., 2018, ApJ, 862, 110
Schruba A., Kruijssen J. M. D., Leroy A. K., 2019, ApJ, 883, 2
Schuster K. F., Kramer C., Hitschfeld M., Garcia-Burillo S., Mookerjea B., 2007, A&A, 461, 143
Scoville N. Z., Hersh K., 1979, ApJ, 229, 578
Scoville N. Z., Wilson C. D., 2004, in Lamers H. J. G. L. M., Smith L. J., Nota A., eds, Astronomical Society of the Pacific Conference Series Vol. 322, The Formation and Evolution of Massive Young Star Clusters. p. 245
Sembach K. R., Howk J. C., Ryans R. S. I., Keenan F. P., 2000, ApJ, 528, 310
Semenov V. A., Kravtsov A. V., Gnedin N. Y., 2017, ApJ, 845, 133
Semenov V. A., Kravtsov A. V., Gnedin N. Y., 2018, ApJ, 861, 4
Seon K.-I., Witt A. N., 2012, ApJ, 758, 109
Silk J., 1997, ApJ, 481, 703
Solomon P. M., Rivolo a. R., Barrett J., Yahil a., 1987, ApJ, 319, 730
Sormani M. C., Barnes A. T., 2019, MNRAS, 484, 1213
Sun J., et al., 2018, Astrophys. J., 860, 172
Swinbank A. M., et al., 2011, ApJ, 742, 11
Swinbank A. M., Smail I., Sobral D., Theuns T., Best P. N., Geach J. E., 2012, ApJ, 760, 130
Tacconi L. J., et al., 2013, ApJ, 768, 74
Tacconi L. J., et al., 2018, ApJ, 853, 179
Thilker D. A., Walterbos R. A. M., Braun R., Hoopes C. G., 2002, AJ, 124, 3118
Toomre A., 1964, ApJ, 139, 1217
Tress R. G., Smith R. J., Sormani M. C., Glover S. C. O., Klessen R. S., Mac Low M.-M., Clark P. C., 2019, MNRAS submitted, p. arXiv:1909.10520
Utomo D., et al., 2018, ApJ, 861, L18

Vázquez-Semadeni E., Banerjee R., Gómez G. C., Hennebelle P., Duffin D., Klessen R. S., 2011, MNRAS, 414, 2511

Walter F., Brinks E., de Blok W. J. G., Bigiel F., Kennicutt Jr. R. C., Thornley M. D., Leroy A., 2008, AJ, 136, 2563

Ward J. L., Chevance M., Kruijssen J. M. D., Hygate A. P. S., Schruba A., Longmore S. N., 2019, MNRAS to be submitted

Weidner C., Kroupa P., 2006, MNRAS, 365, 1333

Whitmore B. C., et al., 2014, ApJ, 795, 156

Williams J. P., de Geus E. J., Blitz L., 1994, ApJ, 428, 693

Wong T., Blitz L., 2002, Astrophys. J., 569, 157

Wood K., Hill A. S., Joung M. R., Mac Low M.-M., Benjamin R. A., Haffner L. M., Reynolds R. J., Madsen G. J., 2010, ApJ, 721, 1397

Zanella A., et al., 2019, MNRAS, 489, 2792

Zuckerman B., Palmer P., 1974, ARA&A, 12, 279

da Silva R. L., Fumagalli M., Krumholz M., 2012, ApJ, 745, 145

da Silva R. L., Fumagalli M., Krumholz M. R., 2014, MNRAS, 444, 3275

APPENDIX A: FRACTIONS OF COMPACT AND DIFFUSE EMISSION

In order to obtain robust results from our statistical analysis with the HEISENBERG code, we need to remove the biasing impact of diffuse emission. We do this by separating the compact HII regions and GMCs from the large-scale diffuse emission in both tracers. The method for doing this has been presented, tested, and validated by Hygate et al. (2019b) and a filtering procedure based on filtering in Fourier space has been implemented in HEISENBERG. As recommended in Hygate et al. (2019b), we use a Gaussian filter of FWHM $\sim 10 \times \lambda$ to mask the low spatial frequencies in Fourier space (i.e. large-scale emission) and filter out the diffuse emission from the compact regions of interest. The Gaussian shape of the filter used limits artefacts compared to a more selective step function. However, contrary to a step function, a Gaussian function extends to infinitely high spatial frequencies, implying that some compact emission is spuriously filtered out. To compensate for this effect, we apply two correction factors defined by Hygate et al. (2019b) to the measured fraction of compact emission. The first correction factor, q_{con}, compensates for flux loss from the individual compact regions. The second correction factor, q_{overlap}, compensates for the flux loss due to overlap between regions. Prescriptions for q_{con} and q_{overlap} are calibrated in Hygate et al. (2019b) and Hygate et al. (2019a), respectively. We then determine the fraction of emission that belongs to compact structures in the Hα map ($f_{\mathrm{H}\alpha}$) and the CO map (f_{CO}) as:

$$f_{\mathrm{H}\alpha} = \frac{1}{q_{\mathrm{con,H}\alpha} q_{\mathrm{overlap,H}\alpha}} \frac{F'_{\mathrm{H}\alpha}}{F_{\mathrm{H}\alpha}} \qquad (A1)$$

and

$$f_{\mathrm{CO}} = \frac{1}{q_{\mathrm{con,CO}} q_{\mathrm{overlap,CO}}} \frac{F'_{\mathrm{CO}}}{F_{\mathrm{CO}}}, \qquad (A2)$$

where $F_{\mathrm{H}\alpha}$ (respectively F_{CO}) is the total flux in the original Hα (respectively CO) map and $F'_{\mathrm{H}\alpha}$ (respectively F'_{CO}) is the total flux in the filtered Hα (respectively CO) map. After applying these corrections, we obtain the fractions of compact flux as listed in Table A1. The diffuse emission fractions follow as the complement of the compact emission fractions, i.e. as $1 - f_{\mathrm{H}\alpha}$ and $1 - f_{\mathrm{CO}}$.

As recommended by Hygate et al. (2019b), we ensure that $q_{\mathrm{con}} \geqslant 0.9$, so that the correction to be applied to the compact fraction is relatively small. For each galaxy, this is done by setting the FWHM of the Gaussian filter to the smallest multiple of λ at which this condition is satisfied. This results in cut-off wavelengths

for the Gaussian filters in the range $10-12 \times \lambda$, as listed in Table 3. These values ensure an optimum between maximising the filtering of the diffuse emission, and minimising the spurious filtering of the compact structures.

For comparison, we note that Pety et al. (2013) find that 50 ± 10 per cent of the CO(1-0) emission in NGC5194 is distributed on scales larger than 1.3 kpc, which is close to the size of the Gaussian filter used in our analysis for this galaxy (~ 1.7 kpc). This estimate is obtained by comparing the amount of flux recovered by the Plateau de Bure interferometer to the total flux measured by the IRAM-30 m single-dish telescope. This is roughly equivalent to filtering the emission on large scales in Fourier space, without applying the correction factors mentioned above. Before taking into account the correction factors $q_{\mathrm{con}} = 0.90^{+0.01}_{-0.01}$ and $q_{\mathrm{overlap}} = 0.45^{+0.06}_{-0.04}$, we measure a fraction of diffuse emission of 56 ± 2 per cent in NGC5194, in agreement with the above estimate by Pety et al. (2013). Caldú-Primo et al. (2015) found (lower) diffuse fractions in the range $8-48$ per cent for two other galaxies, which is consistent with our results listed in Table A1. After including the correction factors, we obtain a true diffuse fraction for NGC5194 in a range (representing the 1σ uncertainty interval) of $0-9$ per cent.

APPENDIX B: RADIAL PROFILES

Here we present the (galactocentric) radial profiles of all quantities necessary to reproduce our analysis of the data and the comparison with analytical models in Figure 5. The position and width of the radial bins as defined in Section 5.1 are outlined in Figure B1, also highlighting the regions affected by bars (light blue) and the masked central and outer regions (grey). For each of these bins, the reference timescale (t_{ref}), the SFR, and the gas conversion factor (α_{CO}) used as input in the HEISENBERG code are presented in Figure B2, in addition to the values used when analysing each galaxy in its entirety. For each bin, t_{ref} and α_{CO} are calculated using the metallicity dependence from Haydon et al. (2018) and Bolatto et al. (2013), respectively. The galaxy-scale values are based on the CO flux-weighted average metallicity. Note that the galaxy-wide SFR by definition corresponds to the sum of the individual bins. Table B1 summarises the measured cloud lifetimes (t_{CO}), for each galaxy and each individual radial bin.

Figure B3 shows the radial profiles of properties describing the galaxies, i.e. the molecular gas surface density $\Sigma_{\mathrm{H_2}}$, the stellar surface density Σ_{stars}, the SFR surface density Σ_{SFR}, the circular velocity, the Toomre Q stability parameter, and the gas phase metallicity [expressed as $12 + \log(\mathrm{O/H})$]. We calculate $\Sigma_{\mathrm{H_2}}$ using the CO flux-weighted average α_{CO} from Figure B2. The stellar mass surface density profiles are derived from S4G/3.6 μm imaging (M. Querejeta et al. in prep.), in a similar way as presented in Meidt et al. (2012, 2014); Querejeta et al. (2014). The SFR surface density profiles are obtained as described in Section 2.4. The rotation curves are derived by fitting a model of projected circulation motion to the observed CO velocity fields, as described in detail by Lang et al. (2019). Where the data quality is not good enough to perform this measurement (due to noise or missing data, which applies to the outskirts of NGC3351, NGC4303, NGC4321, and NGC4535, as well as for NGC5068), we used the fitted rotation curve as a function of the galactocentric radius R, in the form $V_{\mathrm{rot}} = V_0 (2/\pi) \arctan(R/r_{\mathrm{t}})$, where V_0 and r_{t} have been fitted by Lang et al. (2019). Toomre Q follows from the above input variables in combination with the second moment of the CO

Galaxy	$f_{\mathrm{H}\alpha}$	f_{CO}	$q_{\mathrm{con,H\alpha}}$	$q_{\mathrm{con,CO}}$	$q_{\mathrm{overlap,H\alpha}}$	$q_{\mathrm{overlap,CO}}$
NGC0628	$0.69^{+0.01}_{-0.01}$	$0.82^{+0.06}_{-0.06}$	$0.89^{+0.02}_{-0.01}$	$0.89^{+0.02}_{-0.01}$	$0.74^{+0.02}_{-0.01}$	$0.52^{+0.06}_{-0.05}$
NGC3351	$0.31^{+0.01}_{-0.01}$	$0.83^{+0.06}_{-0.06}$	$0.89^{+0.01}_{-0.01}$	$0.90^{+0.01}_{-0.01}$	$0.73^{+0.02}_{-0.02}$	$0.56^{+0.05}_{-0.04}$
NGC3627	$0.42^{+0.01}_{-0.01}$	$0.81^{+0.04}_{-0.06}$	$0.91^{+0.02}_{-0.01}$	$0.91^{+0.01}_{-0.01}$	$0.70^{+0.03}_{-0.02}$	$0.49^{+0.06}_{-0.04}$
NGC4254	$0.69^{+0.01}_{-0.02}$	$0.74^{+0.06}_{-0.06}$	$0.91^{+0.01}_{-0.01}$	$0.91^{+0.02}_{-0.01}$	$0.67^{+0.03}_{-0.02}$	$0.48^{+0.06}_{-0.05}$
NGC4303	$0.68^{+0.01}_{-0.03}$	$0.82^{+0.08}_{-0.10}$	$0.89^{+0.02}_{-0.01}$	$0.90^{+0.02}_{-0.02}$	$0.62^{+0.05}_{-0.02}$	$0.46^{+0.09}_{-0.06}$
NGC4321	$0.44^{+0.01}_{-0.01}$	$0.79^{+0.05}_{-0.05}$	$0.91^{+0.01}_{-0.01}$	$0.91^{+0.01}_{-0.01}$	$0.69^{+0.02}_{-0.02}$	$0.49^{+0.04}_{-0.04}$
NGC4535	$0.93^{+0.02}_{-0.03}$	$0.98^{+0.09}_{-0.11}$	$0.89^{+0.02}_{-0.01}$	$0.90^{+0.02}_{-0.02}$	$0.68^{+0.04}_{-0.02}$	$0.44^{+0.08}_{-0.06}$
NGC5068	$0.64^{+0.01}_{-0.01}$	$1.35^{+0.04}_{-0.04}$	$0.92^{+0.01}_{-0.01}$	$0.95^{+0.01}_{-0.01}$	$0.74^{+0.04}_{-0.03}$	$0.76^{+0.03}_{-0.02}$
NGC5194	$0.37^{+0.01}_{-0.01}$	$1.05^{+0.06}_{-0.09}$	$0.90^{+0.01}_{-0.01}$	$0.91^{+0.01}_{-0.01}$	$0.71^{+0.02}_{-0.01}$	$0.45^{+0.06}_{-0.04}$

Table A1. Fractions of emission in the Hα and the CO maps that belong to compact structures ($f_{\mathrm{H}\alpha}$ and f_{CO}, respectively) for each of the nine galaxies in our sample. The diffuse emission fractions follow as $1 - f_{\mathrm{H}\alpha}$ and $1 - f_{\mathrm{CO}}$. We also list the associated correction factors. These are $q_{\mathrm{con,H\alpha}}$ and $q_{\mathrm{con,CO}}$, applied to correct for any over-subtraction of diffuse emission caused by using a Gaussian filter in Fourier space, and $q_{\mathrm{overlap,H\alpha}}$ and $q_{\mathrm{overlap,CO}}$, applied to correct for any over-subtraction of diffuse emission caused by overlap between regions. See Section 3.4 and Hygate et al. (2019a,b) for more details.

maps (A. K. Leroy et al. in prep.) to describe the gas velocity dispersion. We note that, strictly speaking, the second moment is an overestimate of σ_{gas} due to the fact that beam smearing may blend lines of sight with different first moments (i.e. absolute velocities). However, as we are mostly focusing on the flat part of the galaxy rotation curves (Figure B3), the potential effects of beam smearing are limited. Finally, the metallicities are obtained as discussed in Section 3.5. Beyond the quantities shown here, the comparison to theoretical models in Section 5.2 uses the stellar velocity dispersion, which is determined according to eq. 22 in the Methods section of Kruijssen et al. (2019), and the spiral arm pattern speeds from the references listed in Table 5.

Figure B4 shows the radial profiles of the CO flux-weighted average properties of the cloud population, i.e. the radius, velocity dispersion σ_{GMC}, mass, surface density Σ_{GMC}, volume density $\rho_{\mathrm{H_2}}$, and virial parameter α_{vir}. The GMC radii and masses are derived using the output from HEISENBERG as described and motivated in Section 5.2. The GMC velocity dispersions are taken from the CPROPS GMC catalogues of these galaxies. More details about the application of CPROPS and the properties of the cloud population in this sample of galaxies can be found in E. Rosolowsky et al. (in prep.). The surface densities, volume densities, and virial parameters are derived from the first three quantities.

APPENDIX C: GAS SURFACE DENSITY THRESHOLD SEPARATING GALACTIC AND CLOUD-SCALE DYNAMICS

In Section 5.4, we investigate whether cloud lifetimes are set by internal dynamics (i.e. the cloud crossing time or free-fall time) or galactic dynamics (i.e. the combination of mechanisms considered by Jeffreson & Kruijssen 2018, see Section 5.2). By characterising the properties of the radial bins in Figure 5 where the measured cloud lifetimes better agree with the red (internal) and blue (galactic) lines, we find that both situations can occur and seem to occupy different ranges of the large-scale molecular gas surface density (i.e. averaged on kpc scales, across the entire radial bin).

At low surface densities, cloud lifetimes follow the cloud crossing time or free-fall time, whereas at high surface densities, they match the galactic dynamical time-scale. Figure 6 quantifies this statement by dividing the sample of radial bins in which the cloud lifetime is measured at a surface density of $\Sigma_{\mathrm{H_2,ring}} = 8\,M_\odot\,\mathrm{pc}^{-2}$ and considering the difference between the measured cloud lifetime and the galactic and internal dynamical time-scales. To arrive at this critical surface density threshold separating both regimes, we have systematically varied the density threshold at which the sample of radial bins is divided into low and high densities.

Figure C1 shows how the choice of the surface density threshold affects the median absolute logarithmic offset between the measured cloud lifetime (t_{CO}) and the predicted internal (t_{cr} and t_{ff}) and galactic (τ_{gal}) dynamical times, as well as the standard deviation of this offset. While the cloud lifetimes in low-density regions are relatively insensitive to the choice of threshold and generally correlate well with t_{cr} and t_{ff} (left-hand panels), the high-density regions only correlate well with the galactic dynamical time-scale if a sufficiently high threshold density is used to define 'high density' environments (i.e. $\Sigma_{\mathrm{H_2}} > 8\,M_\odot\,\mathrm{pc}^{-2}$). The corresponding scatter exhibits a steep decrease for $\Sigma_{\mathrm{H_2}} \geqslant 7\,M_\odot\,\mathrm{pc}^{-2}$ (bottom-right panel), which is also where the median offset between t_{CO} and t_{ff} starts to drop (top-left panel). For threshold values higher than $9\,M_\odot\,\mathrm{pc}^{-2}$, the prediction due to galactic dynamics develops an offset from the observed cloud lifetimes (top-right panel). Finally, the cloud lifetimes in low-density environments start matching the prediction for galactic dynamics to within 0.2 dex when adopting threshold densities of $\Sigma_{\mathrm{H_2}} > 12\,M_\odot\,\mathrm{pc}^{-2}$ (top-left panel). In the light of these observations, we adopt a threshold value of $\Sigma_{\mathrm{H_2}} = 8\,M_\odot\,\mathrm{pc}^{-2}$.

An alternative to Figure 6 for visualising the two regimes is shown in Figure C2, where we demonstrate how the ratios $t_{\mathrm{CO}}/\tau_{\mathrm{gal}}$ $t_{\mathrm{CO}}/t_{\mathrm{cr}}$ and $t_{\mathrm{CO}}/t_{\mathrm{ff}}$ depend on the kpc-scale gas surface density for all of our measurements. At surface densities $\Sigma_{\mathrm{H_2,ring}} < 8\,M_\odot\,\mathrm{pc}^{-2}$, the figure shows that t_{CO} is systematically offset from τ_{gal} by a factor of 0.5, and that the ratio between the two quantities shows considerable scatter. By contrast, the median $t_{\mathrm{CO}}/t_{\mathrm{cr}}$ and $t_{\mathrm{CO}}/t_{\mathrm{ff}}$ are close to unity in this regime, with modest scatter. This implies that internal dynamics set the GMC lifetime at low gas surface densi-
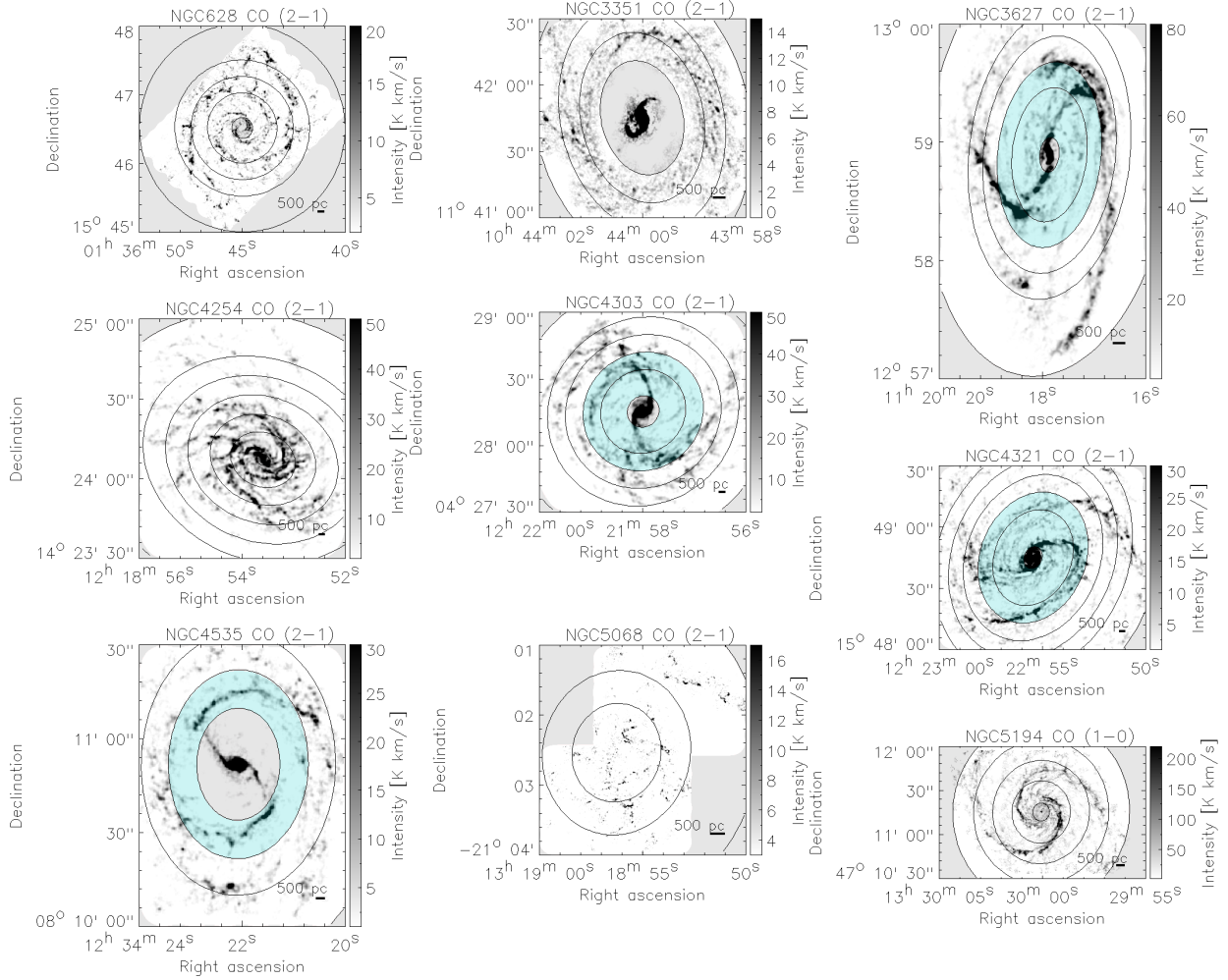
Figure B1. Definition of the bins in galactocentric radius for each galaxy, outlined by black ellipses. The grey-shaded centres were identified by eye and have been excluded from the analysis. The same applies to the regions outside the outer ellipse, defined as the outer radius at which an emission peak is identified in either of the two maps. The bins containing a bar or the end of a bar are coloured in light blue. The background images show the CO(2-1) intensity maps [CO(1-0) for NGC5194].

ties. At surface densities $\Sigma_{H_2,ring} > 8\,M_\odot pc^{-2}$, the ratio t_{CO}/τ_{gal} is unity, whereas t_{CO}/t_{cr} and t_{CO}/t_{ff} are now systematically offset from unity, by a factor of 1.3 and 1.9, respectively. The similar scatter of all ratios at high kpc-scale gas surface densities means that the cloud lifetime matches the time-scale for galactic dynamics, as well as a fixed multiple of (1.3−1.9 times) the internal dynamical time-scale. As discussed in Section 5.4, this close agreement with both time-scales is expected when galactic dynamics set the time-scale for cloud evolution (this is referred to as the 'Toomre regime' by Krumholz et al. 2012), because the cloud dynamics adjust to the galactic dynamics in this regime. In summary, Figure C1 and C2 substantiate the rough division made of our sample into two regimes of kpc-scale molecular gas surface density. Future work with a larger sample of galaxies will need to refine this division.

[1]*Astronomisches Rechen-Institut, Zentrum für Astronomie der Universität Heidelberg, Mönchhofstraße 12-14, 69120 Heidelberg, Germany*
[2]*Max-Planck Institut für Astronomie, Königstuhl 17, 69117 Heidelberg, Germany*
[3]*Max-Planck Institut für Extraterrestrische Physik, Giessenbach-straße 1, 85748 Garching, Germany*
[4]*Astrophysics Research Institute, Liverpool John Moores University, IC2, Liverpool Science Park, 146 Brownlow Hill, Liverpool L3 5RF, UK*
[5]*Research School of Astronomy and Astrophysics, Australian National University, Canberra, ACT 2611, Australia*
[6]*IRAM, 300 rue de la Piscine, 38406 Saint Martin d'Hères, France*
[7]*CNRS, IRAP, 9 Av. du Colonel Roche, BP 44346, F-31028 Toulouse cedex 4, France*
[8]*Université de Toulouse, UPS-OMP, IRAP, F-31028 Toulouse cedex 4, France*
[9]*Department of Astronomy, The Ohio State University, 140 West 18th Ave, Columbus, OH 43210, USA*
[10]*Sterrenkundig Observatorium, Universiteit Gent, Krijgslaan 281 S9, B-9000 Gent, Belgium*
[11]*Sorbonne Université, Observatoire de Paris, Université PSL, CNRS, LERMA, F-75005, Paris, France*
[12]*Departamento de Astronomía, Universidad de Chile, Casilla 36-D, Santiago, Chile*
[13]*4-183 CCIS, University of Alberta, Edmonton, Alberta, Canada*
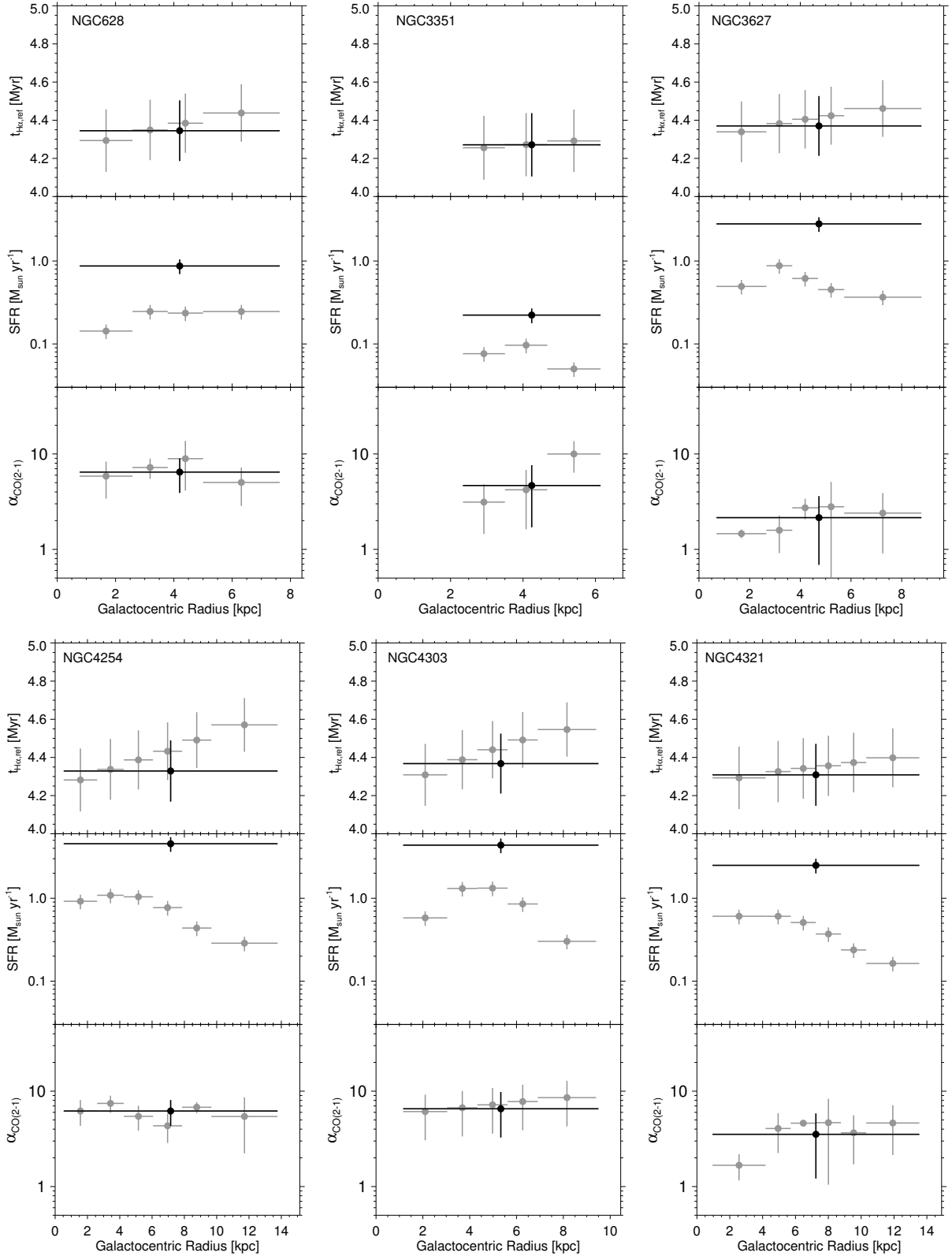[14]*Argelander-Institut für Astronomie, Universität Bonn, Auf dem*

Figure B2. Radial profiles of the input quantities of our analysis, i.e. $t_{\mathrm{H}\alpha,\mathrm{ref}}$, absolute SFR and α_{CO}. The black data points show the values for the entire galaxy (which are averages for $t_{\mathrm{H}\alpha,\mathrm{ref}}$ and α_{CO}, and the total for the SFR), whereas the grey data points show the same for each individual bin of galactocentric radius. For each data point, the horizontal bar represents the range of radii within which these quantities are measured and the vertical bar represents the 1σ uncertainties.
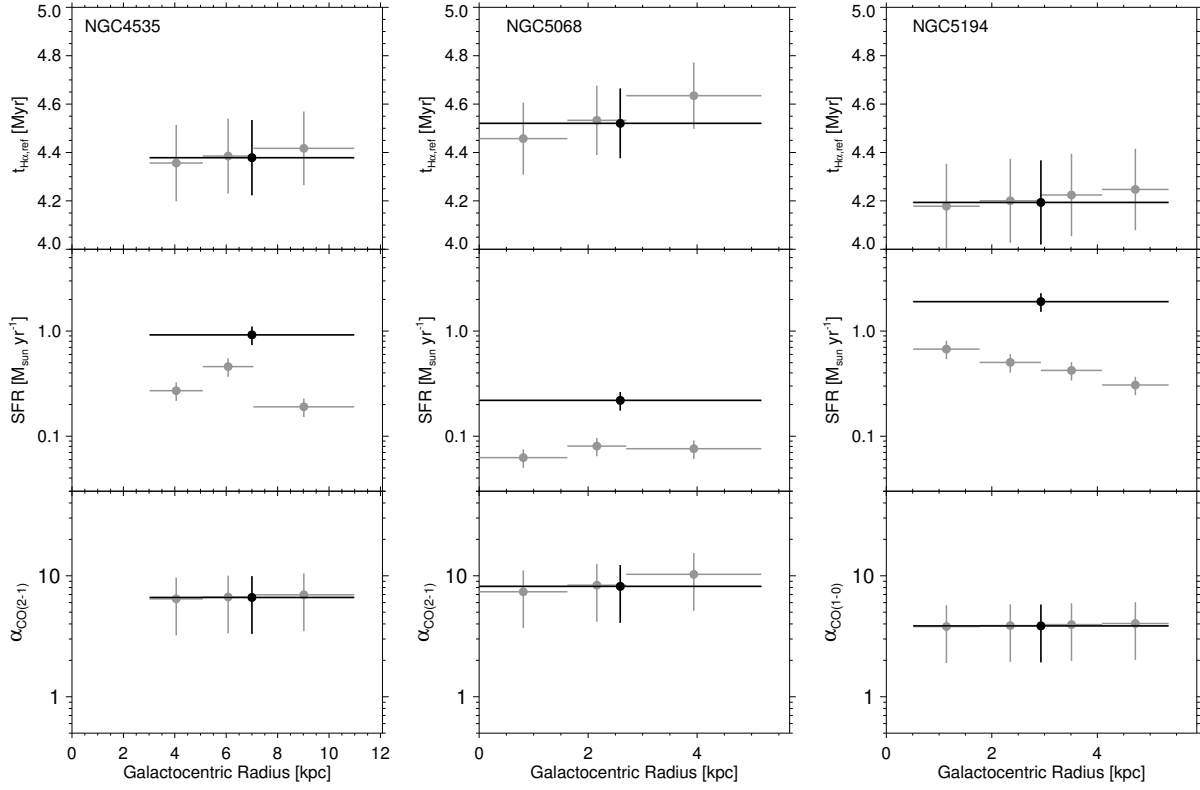
Figure B2 – *continued*

NGC0628	Radial interval [kpc]	entire	0.77-2.58	2.58-3.79	3.79-5.00	5.00-7.63		
	t_{GMC} [Myr]	$24.0^{+3.6}_{-2.5}$	$20.0^{+5.1}_{-3.6}$	$16.4^{+4.3}_{-2.8}$	$14.7^{+3.3}_{-2.9}$	$24.9^{+10.3}_{-4.9}$		
NGC3351	Radial interval [kpc]	entire	2.34-3.50	3.50-4.67	4.67-6.14			
	t_{GMC} [Myr]	$20.6^{+3.4}_{-3.0}$	$26.3^{+8.5}_{-5.7}$	$16.4^{+3.9}_{-2.8}$	$15.3^{+8.7}_{-2.9}$			
NGC3627	Radial interval [kpc]	entire	0.69-2.66	2.66-3.68	3.68-4.70	4.70-5.73	5.73-8.78	
	t_{GMC} [Myr]	$18.9^{+3.4}_{-3.2}$	$20.0^{+7.9}_{-4.3}$	$3.8^{+2.6}_{-0.8}$	$43.2^{+87.7}_{-11.5}$	$45.7^{+14.8}_{-11.6}$	$28.7^{+12.0}_{-6.3}$	
NGC4254	Radial interval [kpc]	entire	0.53-2.60	2.60-4.25	4.25-6.06	6.06-7.86	7.86-9.67	9.67-13.77
	t_{GMC} [Myr]	$20.9^{+3.9}_{-2.3}$	$17.6^{+36.9}_{-4.1}$	$14.8^{+6.9}_{-2.3}$	$19.1^{+5.0}_{-2.7}$	$105.4^{+55.1}_{-23.4}$	$17.3^{+5.5}_{-3.7}$	$21.5^{+7.4}_{-4.3}$
NGC4303	Radial interval [kpc]	entire	1.16-3.10	3.10-4.39	4.39-5.68	5.68-6.97	6.97-9.50	
	t_{GMC} [Myr]	$16.9^{+4.6}_{-2.2}$	$7.9^{+4.8}_{-1.9}$	$17.8^{+13.7}_{-4.0}$	$15.6^{+15.8}_{-2.8}$	$21.6^{+20.5}_{-4.7}$	$11.3^{+3.1}_{-2.1}$	
NGC4321	Radial interval [kpc]	entire	0.95-4.18	4.18-5.71	5.71-7.24	7.24-8.77	8.77-10.31	10.31-13.54
	t_{GMC} [Myr]	$19.1^{+2.3}_{-2.2}$	$31.2^{+19.3}_{-6.1}$	$16.0^{+3.6}_{-2.7}$	$16.2^{+5.5}_{-2.2}$	$20.2^{+4.2}_{-3.9}$	$11.7^{+4.2}_{-2.0}$	$29.3^{+20.1}_{-7.3}$
NGC4535	Radial interval [kpc]	entire	3.02-5.09	5.09-7.06	7.06-10.98			
	t_{GMC} [Myr]	$26.4^{+4.7}_{-3.6}$	$61.3^{+92.4}_{-19.2}$	$25.9^{+5.0}_{-3.2}$	$16.7^{+8.1}_{-3.7}$			
NGC5068	Radial interval [kpc]	entire	0.00-1.62	1.62-2.70	2.70-5.18			
	t_{GMC} [Myr]	$9.6^{+2.9}_{-1.8}$	$17.2^{+3.7}_{-2.6}$	$7.7^{+9.0}_{-2.6}$	$5.7^{+3.0}_{-1.1}$			
NGC5194	Radial interval [kpc]	entire	0.51-1.77	1.77-2.93	2.93-4.09	4.09-5.35		
	t_{GMC} [Myr]	$30.5^{+9.2}_{-4.8}$	$20.1^{+13.5}_{-4.4}$	$59.7^{+70.3}_{-18.2}$	$17.0^{+10.2}_{-3.5}$	$37.3^{+24.9}_{-9.5}$		

Table B1. Measured molecular cloud lifetimes for each galaxy in its entirety, as well as in each individual radial bin.
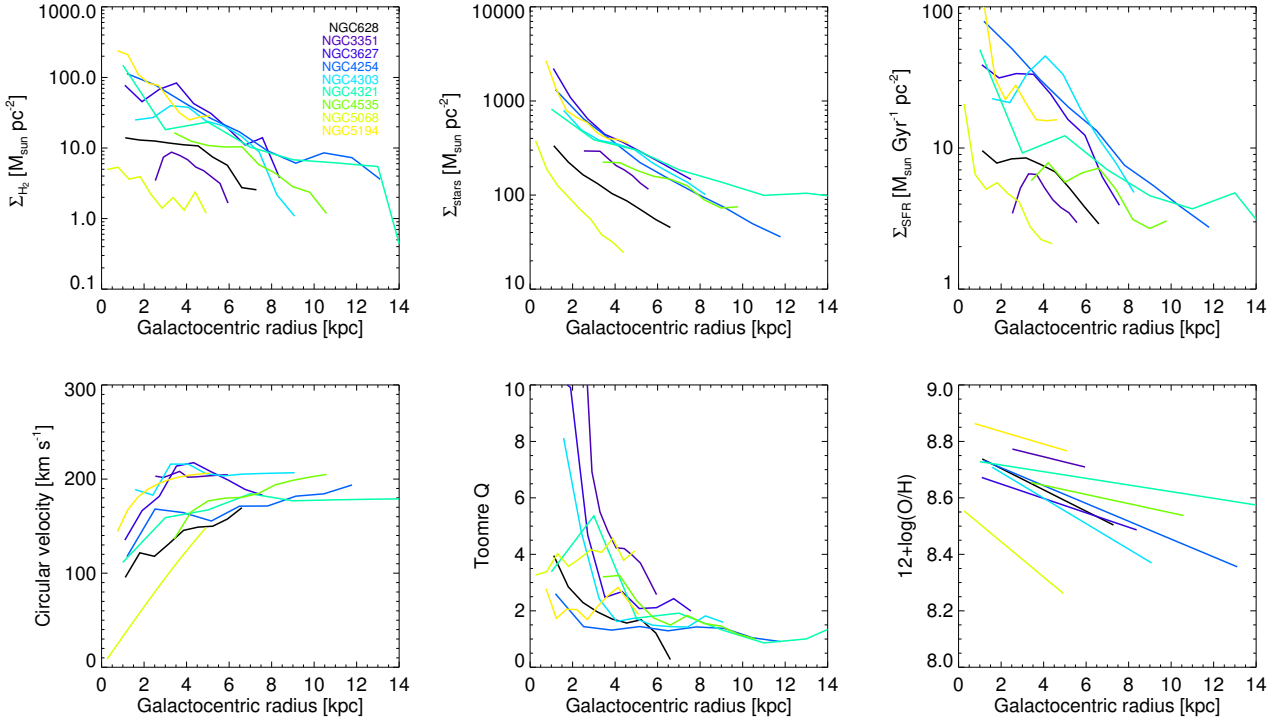
Figure B3. Radial profiles of properties describing the galaxies in our sample. From left to right, the top row shows the molecular gas surface density (using the conversion factor from Table 3), the stellar mass surface density and the SFR surface density (calculated as described in Section 2.4). The bottom row shows the rotation curve (Lang et al. 2019), the Toomre Q parameter and the gas-phase metallicity gradient (Pilyugin et al. 2014, see Section 3.5).

Hügel 71, 53121 Bonn, Germany

[15]*The Observatories of the Carnegie Institution for Science, 813 Santa Barbara Street, Pasadena, CA 91101, USA*

[16]*European Southern Observatory, Karl-Schwarzschild-Straße 2, D-85748 Garching bei München, Germany*

[17]*Univ. Lyon, Univ. Lyon1, ENS de Lyon, CNRS, Centre de Recherche Astrophysique de Lyon UMR5574, F-69230 Saint-Genis-Laval France*

[18]*Institüt für Theoretische Astrophysik, Zentrum für Astronomie der Universität Heidelberg, Albert-Ueberle-Strasse 2, 69120 Heidelberg, Germany*

[19]*Caltech/IPAC, California Institute of Technology, Pasadena, CA, USA*

[20]*Observatorio Astronómico Nacional (IGN), C/Alfonso XII 3, Madrid E-28014, Spain*

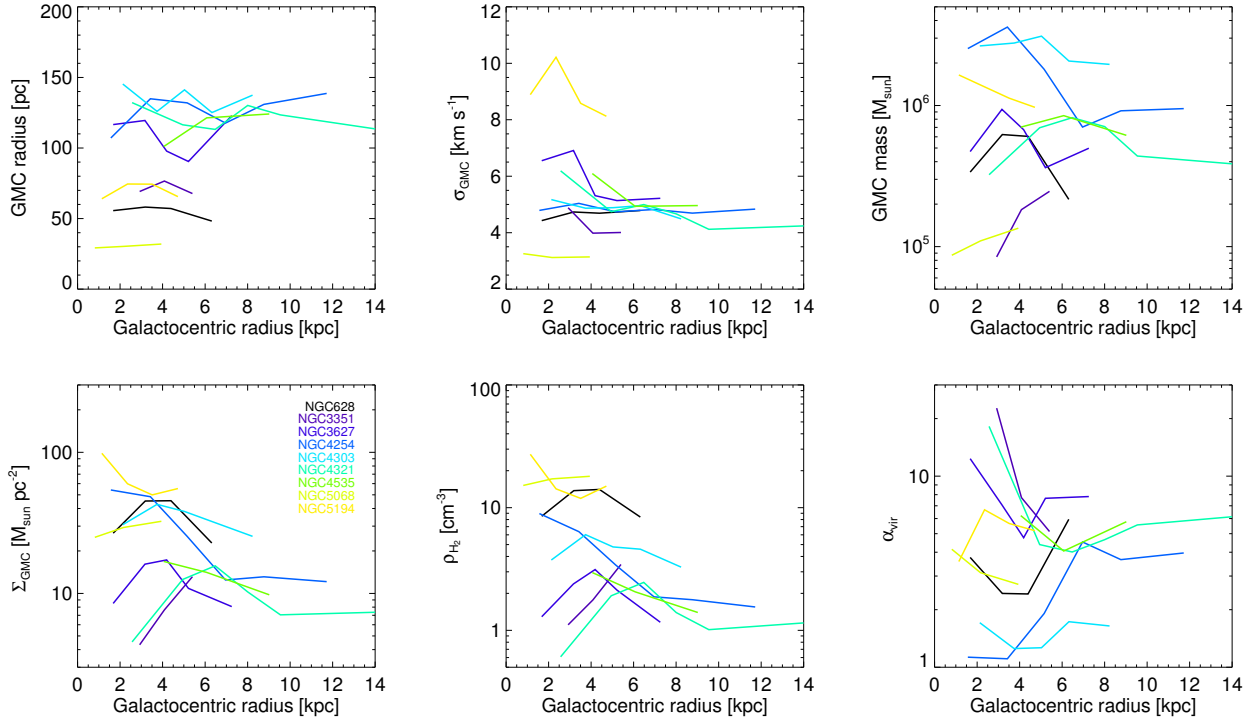This paper has been typeset from a TEX/LATEX file prepared by the author.

Figure B4. Radial profiles of the CO flux-weighted average properties of the molecular cloud population of each galaxy. From left to right, the top row shows the CO flux-weighted average cloud radius, velocity dispersion, and luminous mass as a function of galactocentric radius. The bottom row shows the CO flux-weighted average molecular gas surface density of clouds, the H_2 number density and the virial parameter. The quantities in the top row are derived from the output of HEISENBERG (for the GMC radius and mass) and the CPROPS GMC catalogue (E. Rosolowsky et al. in prep.; for the velocity dispersion). The quantities in the bottom row are derived from those in the top row.
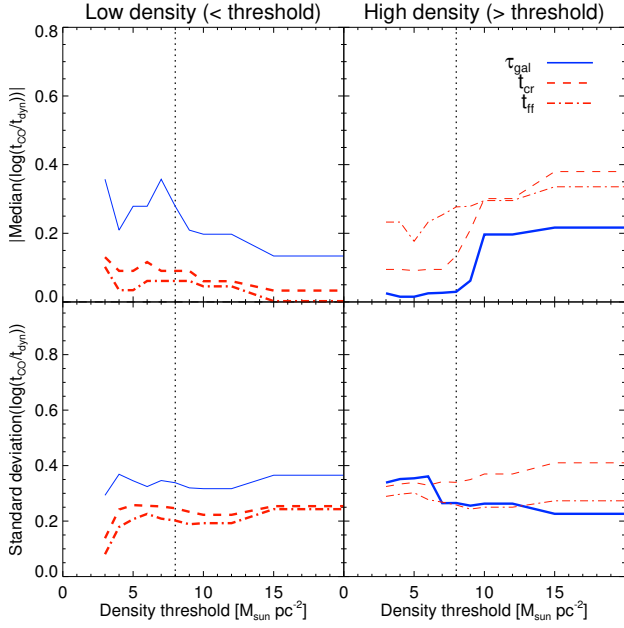
Figure C1. Median absolute logarithmic offset between the measured cloud lifetime (t_{CO}) and the predicted internal (t_{cr} and t_{ff}) and galactic (τ_{gal}) dynamical times (top panels), as well as the standard deviation of this offset (bottom panels), for clouds in environments of low (left-hand panels) and high (right-hand panels) kpc-scale molecular gas surface densities, as a function of the density threshold used to divide the sample into 'low' and 'high' gas surface densities. See Figure 6 for reference. A perfect correlation corresponds to a median and scatter of zero. We find that the cloud lifetime in high density regions (respectively low density regions) correlates best with τ_{gal} (respectively t_{cr} and t_{ff}) when dividing the regions at a density threshold of $\Sigma_{H_2,ring} = 8\,M_\odot\,pc^{-2}$, indicated by the vertical dotted line. Figure 6 compares t_{CO}, τ_{gal}, t_{cr}, and t_{ff} for the two 'low' and 'high' gas surface density regimes separated by this density threshold.
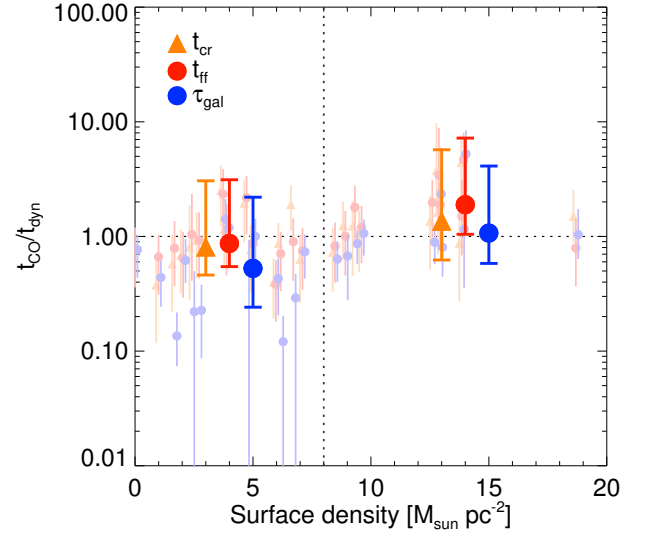
Figure C2. Ratio of the measured cloud lifetime t_{CO} over the dynamical time (τ_{gal} in pale blue dots, t_{cr} in pale orange triangles, t_{ff} in pale red dots) as a function of the galactic gas surface density $\Sigma_{H_2,ring}$. On either side of $\Sigma_{H_2,ring} = 8\,M_\odot\,pc^{-2}$ (vertical dotted line), the median and standard deviation of the ratios are indicated by the large, bright symbols, respectively. At surface densities lower than this surface density threshold, we note a larger dispersion of t_{CO}/τ_{gal} compared to t_{CO}/t_{cloud}, as well as a median of $t_{CO}/\tau_{gal} \approx 0.5$, whereas $t_{CO}/t_{cr} \approx t_{CO}/t_{ff} \approx 1$. By contrast, at surface densities higher than this threshold, the dispersions of the ratios are all similar, with absolute values of $t_{CO}/\tau_{gal} \approx 1$, $t_{CO}/t_{cr} \approx 1.9$ and $t_{CO}/t_{cr} \approx 1.3$. See Section 5.4 for a detailed discussion and physical interpretation of these results.